Exploring excitons in van der Waals heterostructures and their potential for lasing

Lin, Qiaoling

Publication date:
2023

Document Version
Publisher's PDF, also known as Version of record

Doctor of Philosophy
Doctoral thesis in Photonics Engineering

DTU Electro
Department of Electrical and Photonics Engineering

Exploring excitons in van der Waals heterostructures and their potential for lasing

Author: Qiaoling Lin

DTU

Supervisor: Assoc. Prof. Sanshui Xiao
Co-supervisors: Assoc. Prof. Martijn Wubs & Assoc. Prof. Nicolas Stenger

DTU Electro
Department of Electrical and Photonics Engineering
Technical University of Denmark
Ørsteds Plads
Building 343
2800 Kongens Lyngby, Denmark

Preface

This thesis is submitted in fulfilment of the requirements for the degree of Doctor of Philosophy at the Technical University of Denmark (DTU). The project has been carried out in the Quantum Photonics of Low-Dimensional Systems group at DTU Fotonik from March 2020 to June 2023 under the supervision of Assoc. Prof. Sanshui Xiao, Assoc. Prof. Nicolas Stenger and Assoc. Prof. Martijn Wubs.

The research has been financed by the Independent Research Fund Denmark (project no. 9041-00333B and project no.2032-00351B), and by the Center for Nanostructured Graphene supported by the Danish National Research Foundation (project no. DNRF103).

In this PhD project, we study excitons in heterobilayers and light-matter interaction in combination with silicon photonic cavities. This PhD project has been carried out in close collaboration with several international groups, in particular with Prof. Zhipei Sun at Aalto University and with Dr. Hanlin Fang at Chalmers University of Technology.

Kongens Lyngby, 6th July 2023

Qiaoling Lin

Abstract

Two-dimensional (2D) semiconducting transition metal dichalcogenides (TMDs) have gained intense attention in the field of optoelectronics and nanophotonics due to their unique excitonic properties. TMDs can act as efficient gain materials for lasing in combination with photonic cavities. Nanolasers based on TMDs have been extensively studied and offer promising prospects for energy-efficient lasers. Interlayer excitons (IXs) in type-II van der Waals heterostructures hold promise for energy-efficient, silicon-integrated, tunable, and electrically pumped lasers. The moiré potentials formed in heterostructures create additional in-plane confinement on IXs, thus potentially providing large optical gain at low pumping levels. However, there is still a lack of research regarding the moiré exciton at room temperature, and the influence of moiré superlattices on laser performance remains unexplored.

In this PhD project, we build a deterministic assembly system for transferring 2D materials. Starting with debugging an old spectrometer, we construct a multifunctional optical measurement setup working from the visible to the near-infrared (NIR) spectrum with high sensitivity. The success in platform construction serves as the cornerstone for our upcoming experiments.

We fabricate high-quality MoS_2/WSe_2 heterobilayers and study the optical properties of excitons and their dependence on twist angles and pump power. We observe a significant energy shift (> 200 meV) of the IXs by varying twist angles. When the twist angle is close to zero, the IX resonance shows a notable blue-shift as we increase the pump power and the absorption peak of WSe_2 A exciton splits. These observations indicate the existence of moiré excitons at room temperature.

In addition, we study the impact of the moiré potential on the excitons by analyzing the time-resolved PL dynamics. We find that heterobilayers with strong interlayer coupling exhibit a lower IX energy and a longer IX lifetime than that with weak coupling. Our observation reveals that moiré excitons could be an efficient gain medium for energy-efficient and high-performance nanolasers.

Furthermore, we couple moiré IXs to silicon topological cavities and study their light-matter interaction. We fabricate silicon high-Q cavities at DTU Nanolab and the hBN-encapsulated MoS_2/WSe_2 heterostructures are then transferred onto the photonic cavities by using our home-built transfer setup. By conducting power-dependent PL measurements, we observe low-threshold lasing-like emission in the optical fiber communication O-band (1260-1360 nm). Our device shows the highest spectral coherence ($\sim$0.1 nm) compared to all 2D material laser systems and an im-

pressive spontaneous-emission suppression ratio (SESR) of ∼10 dB, similar to the value achieved by the TMD-based vertical-cavity surface-emitting laser (VCSEL).

Our works encourage studying novel exciton physics in moiré superlattices at room temperature and open new avenues for using these artificial quantum materials in high-performance device applications.

Resumé

Todimensionelle (2D) halvledende overgangsmetal-dichalcogener (TMD'er) har fået stigende interesse indenfor områder som optoelektronik og nanofotonik grundet deres særprægede excitoniske egenskaber. I kombination med fotoniske kaviteter kan TMD'er spille rollen som et effektivt forstærkningsmedie og udmunde i lasing. TMD-baserede nanolasere er et forskningsområde med meget opmærksomhed, og kan muligvis byde på energieffektive nanolasere. To-lags-delte excitoner (IX) i type-2 van der Waals heterostrukturer har lovende udsigter til sillicium-integrerede modificerbare energieffektive elektrisk-pumpede lasere. Moirépotentialet skabt af heterostrukturen skaber yderligere indskrænkning af IX'erne i samme plan, potentielt resulterende i en kraftigere optisk forstærkning ved svag pumpning. Der er til gengæld manglende forskning indenfor moiré excitoner ved stuetemperatur. Derudover er indflydelsen af moiré supergitteret på laserkarakteristika uudforsket territorie.

I dette ph.d. projekt bygges der et deterministisk samlingssystem til overførsel af 2D materialer. Ved modificering af et gammelt spektrometer bygges der et multifunktionelt optisk setup til højt sensitive måleserier fra den synlige til den nær-infrarøde ende af spektret. Denne platform er en hjørnesten for kommende eksperimenter.

Vi fabrikerer MoS2/WSe2 hetero-dobbeltlag af høj kvalitet, og undersøger excitonernes optiske egenskaber samt vridningsvinklens og pumpe-effektens indflydelse på det førnævnte. Ved at ændre vridningsvinklen findes et signifikant energiskift ($>$ 200 meV) for IX'erne. Med en næsten afrettet vridningsvinkel viser IX'ernes resonans et betydeligt blåskift når pumpens effekt øges, og absorptionslinjen for A-excitonen i WSe2 splitter sig i to. Sådanne observationer indikerer Moiréexcitoner ved stuetemperatur. Ydermere undersøger vi moirépotentialets indflydelse på excitonerne ved at analysere tidsopløst fotoluminescens dynamik. Hetero-dobbeltlag med stærk kobling mellem lagene udviser en lavere IX energi og en længere henfaldstid, sammenlignet med svag koblingsregimet. Denne observation peger på at moiréexcitoner kan blive et effektivt forstærkningsmedium til energieffektive højt-ydende nanolasere.

Til sidst kobler vi moiré IX'erne til silicium-baserede topologiske kaviteter og undersøger lys-stof vekselvirkningen. Vi fabrikerer siliciumkaviteter i DTU Nanolab med høje kvalitetsfaktorer, og ved brug af det udviklede deterministiske samlingssystem, bliver hBN-indkapslede MoS2/WSe2 heterostrukturer overført til den fotoniske kavitet. Ved at udføre fotoluminescens målinger observeres en laser-lignende karakteristik med lav lasertærskel i O-båndet (1260-1360 nm). Dette apparat har den højeste spektrale kohærens ($\sim$0.1 nm) sammenlignet med alle lasersystemer baseret

på 2D materialer, samt et imponerende spontan emissions undertrykkelses forhold (SESR) på omkring ∼10 dB, sammenligneligt med værdier fundet i vertikal-kavitets overflade-emitterende lasere (VCSELs).

Vores arbejde fremmer forskningen af ny exciton fysik i moiré supergitre ved stuetemperatur og paver nye veje for brugen af kunstige kvantematerialer i højtydende apparater.

Acknowledgements

First and foremost, I would like to thank my supervisors, Sanshui Xiao, Nicolas Stenger, and Martijn Wubs, for giving me the opportunity to pursue my PhD at DTU and thank for their time, valuable support, and insightful feedback throughout my studies. In particular, Sanshui, my principal supervisor, cared about my well-being. Most of my early experiments were frustrating. He told me to take a rest whenever I felt overwhelmed.

I would like to thank Hanlin Fang, our collaborator from Chalmers University of Technology, for the academic discussion and his invaluable contributions in sharing his extensive knowledge and experience for my PhD project. I want to thank Professor Zhipei Sun, our collaborator from Aalto University, for his patience in reviewing our manuscript and for constructive discussion.

I would like to thank all the staff at Nanolab for giving me valuable training on various types of equipment. I would like to thank Professor Juntao Li, my master's supervisor, for providing me with SOI substrates. A big thanks goes to Xiaowei Guan who generously shared his dry etching recipe and valuable experience. I also thank Bingdong Chang, Meng Xiong, Huaqing Qiu, Yaoqin Lu for generously providing their kind assistance.

I would like to thank Kresten Yvind for sharing the spectrometer and the optical table, which are essential for my PhD project. I thank Radu Malureanu, Osamu Takayama and Binbin Zhou for lending me countless optical components. Many thanks to Moritz Fischer for his endless help with debugging the spectrometer and the lifetime setup, as well as MATLAB codes. I thank Yanjing Zhao, a colleague who conducted optical experiments in the same room, for her companionship and encouragement in the dark laboratory.

Furthermore, I thank the wonderful group members, Fengwen, Mads, Mortiz, Laura, Rui, Pooja, Xingyu, Frederik, Devashish, Leonid, Benjamin, Amedeo for their friendliness and support throughout this journey. Big thanks to Laura for her incredible kindness and support. She always patiently explained and translated for me when I looked confused about what others were saying. Thanks to Xingyu for organizing various enjoyable activities. I would like to thank all my friends who have shared countless moments of laughter and joy with me, making my life truly delightful. From playing sports, going on trips, to enjoying meals together, our bond has made my life truly special.

Last but not least, I would like to thank my family for their support. A special

thanks goes to my loving husband Hanlin, who always gives me love, patience, and embrace. It is through his presence that I have come to perceive the essence of love, and thus embark on a journey of self-discovery.

List of publications

Journal pubilcations

Included in this thesis

- **A Room-Temperature Moiré Interlayer Exciton Laser**

  Qiaoling Lin, Hanlin Fang, Yuanda Liu, Yi Zhang, Moritz Fischer, Juntao Li, Joakim Hagel, Samuel Brem, Ermin Malic, Nicolas Stenger, Zhipei Sun, Martijn Wubs, Sanshui Xiao

  arXiv preprint arXiv:2302.01266 (2023)

Additional work

- **Localization and Interaction of Interlayer excitons in $MoSe_2/WSe_2$ Heterobilayers**

  Hanlin Fang, Qiaoling Lin, Yi Zhang, Joshua Thompson, Sanshui Xiao, Zhipei Sun, Ermin Malic, Saroj P. Dash, and Witlef Wieczorek

  In preparation

- **Optically Active Telecom Defects in $MoTe_2$ Fewlayers at Room Temperature**

  Yuxin Lei, Qiaoling Lin, Sanshui Xiao, Juntao Li and Hanlin Fang

  Nanomaterials **13**(9), 1501 (2023)

- **Observation of Multiple Bulk Bound States in the Continuum Modes in a Photonic Crystal Cavity**

  Rui Chen, Yi Zheng, Xingyu Huang, Qiaoling Lin, Chaochao Ye, Meng Xiong, Martijn Wubs, Yungui Ma, Minhao Pu and Sanshui Xiao

  Beilstein J. Nanotechnol. **14**, 544–551 (2023)

Conference contributions

- **Light Emission of Excitons in 2D Layered Materials Integrated with Photonic Microcavities**

  Qiaoling Lin, Nicolas Stenger, Martijn Wubs, Sanshui Xiao

  NanoPhoton **2022** (Poster)

- **Two Dimensional Material Based Nanolasers**

  Qiaoling Lin, Nicolas Stenger, Martijn Wubs, Sanshui Xiao

  International Postgraduate Photonics Forum (IPPF) **2022** (Presentation)

- **Room-temperature Moiré Excitons in van der Waals Heterostructures towards Lasing**

  Qiaoling Lin, Hanlin Fang, Yuanda Liu, Yi Zhang, Moritz Fischer, Juntao Li, Nicolas Stenger, Zhipei Sun, Martijn Wubs, Sanshui Xiao

  Nanophotonics of 2D Materials (N2D) **2023** (Poster)

Abbreviations

2D	Two-dimensional
ADP	$NH_4H_2PO_4$
AFM	Atomic Force Microscope
ARPES	Angle-resolved Photoemission Spectroscopy
ASE	Amplified Spontaneous Emission
BS	Beam Splitter
CBM	Conduction Band Minimum
CCD	Charge-coupled Device
CMOS	Complementary Metal-Oxide-Semiconductor
CVT	Chemical Vapor Transport
CW	Continuous Wave
DBR	Distributed Bragg Reflector
DRS	Differential Reflectance Spectroscopy
EBL	Electron Beam Lithography
EELS	Electron Energy-loss Spectroscopy
FDTD	Finite-difference Time-domain
FM	Flip Mirror
FWHM	Full Width at Half Maximum
GaAs	Gallium Arsenide
HB	Heterobilayer
hBN	hexagonal Boron Nitride

HWP	Half-wave Plate
InAs	Indium Arsenide
InP	Indium Phosphide
IPA	Isopropyl Alcohol
IRF	Instrument Response Function
IX	Interlayer exciton
KDP	KH_2PO_4
LED	Light-emitting Device
L-L curve	Light-in and light-out curve
LPF	Long-pass Filter
mBZ	moire Brillouin Zone
MoS_2	Molybdenum Disulfide
$MoSe_2$	Molybdenum Diselenide
$MoTe_2$	Molybdenum Ditelluride
NA	Numerical Aperture
NIR	Near Infrared
Obj.	Objective
OFC	Optical Fiber Communication
PC	Polycarbonate
PDMS	Polydimethylsiloxane
PL	Photoluminescence
PMT	Photomultiplier Tube
QD	Quantum Dot
QW	Quantum Well
SE	Spontaneous Emission
SEM	Scanning Electron Microscopy
SESR	Spontaneous-emission Suppression Ratio

SHG Second Harmonic Generation

Si_3N_4 Silicon Nitride

SiO_2 Silicon Dioxide

SMSR Single-mode Suppression Ratio

SOC Spin-orbit Coupling

SOI Silicon on Insulator

SPD Single Photon Detector

SPF Short-pass Filter

STEM Scanning Transmission Electron Microscopy

STM Scanning Tunnelling Microscopy

STS Scanning Tunnelling Spectroscopy

TCSPC Time-correlated Single Photon Counting

TEPL Tip-enhanced Photoluminescence

TFET Tunnelling Field-effect Transistor

TiO_2 Titanium Dioxide

TMD Transition Metal Dichalcogenide

UV Ultraviolet

VBM Valence Band Maximum

VCSEL Vertical-cavity Surface-emitting Laser

WS_2 Tungsten Disulfide

WSe_2 Tungsten Diselenide

Contents

Introduction

In today's fast-paced digital world, the need for faster and more efficient data processing is becoming increasingly crucial. Traditional electronic chips face limitations when it comes to speed, power consumption, and bandwidth capacity. Compared to electrons, photons travel at the speed of light without suffering heat loss. And photons possess a broad spectrum that allows for the transmission of multiple signals simultaneously. These have led to a growing interest in the development of all-optical chips, which hold great promise for revolutionizing industries. Silicon has long been the foundation of the electronics industry. Building upon the well-established technology of silicon-based integrated circuits, a silicon photonic integrated circuit holds immense application value [1].

A laser, as a source of coherent light, is a crucial component in enabling the development and advancement of all-optical chips. However, the inherent indirect bandgap of silicon make it an unsuitable material for efficient radiative recombination, thus hindering the laser application. To address this issue, various solutions have been proposed and explored [2]. One approach focuses on enhancing the light-emitting efficiency of silicon, such as utilizing porous Si [3] or Si nanocrystals [4]. However, these attempts have yet to resolve the problem of low emission efficiency in silicon. Another mainstream approach involves integrating direct bandgap III-V materials (e.g., GaAs, InP) onto silicon to achieve high-performance hybrid silicon lasers [5, 6]. Nevertheless, this method involves complex fabrication processes, because the significant lattice mismatch and thermal expansion coefficient mismatches between III-V materials and silicon make direct epitaxial growth challenging.

The emergence of two-dimensional (2D) materials brings great prospects in the fields of optoelectronic devices and nanophotonics [7]. It is considered one of the most promising candidates to extend Moore's Law [8]. Transition metal dichalcogenides (TMDs) are semiconductors in the family of 2D materials. Monolayer TMDs have a direct bandgap, making them suitable gain media without considering lattice matching with various materials including silicon. Thanks to its 2D nature, excitons are strongly confined in atomically thin layers with large exciton binding energy (hundreds of meV) and stable at room temperature. With their unique characteristics, TMDs are promising for the development of energy-efficient hybrid optoelectronic devices.

Currently, TMD-based lasers have been achieved through numerous theoretical studies and experimental demonstrations [9]. Apart from monolayer $MoTe_2$, the

majority of monolayer TMDs exhibits an intrinsic bandgap of 1.5-2 eV [10], which restricts their lasing wavelength below 900 nm. This limitation hinders their integration with silicon. Silicon-based integrated TMD lasers have been reported by utilizing $MoTe_2$ whose emission energy (1.1 eV) is a bit below the silicon bandgap (1.15 eV) [11–13]. Nevertheless, monolayer $MoTe_2$ is susceptible to oxidation in ambient air and faces challenges in extending its emission wavelength to communication wavelengths (e.g., 1310 and 1550 nm).

The interlayer excitons (IXs) in type-II van der Waals heterostructures as an efficient gain medium have been demonstrated for lasing application with integration with silicon [14] and silicon nitride [15] cavities. It features flexible band structure engineering, a significant shift between the photoluminescence (PL) and absorbance peaks, electrical tunability and electrical injection. Thus, it shows great potential for compact, energy-efficient, silicon-integrated, tunable and electrically pumped lasers [15].

The superposition of atomic lattices in heterostructures can create moiré pattern. The additional in-plane quantum confinement in moiré superlattices could potentially enhance the quantum yield of light emission and lead to a large optical gain at low pumping levels, akin to quantum dots which showed lower lasing thresholds than quantum wells and bulk materials [16]. However, the study of the moiré excitons on laser performance has remained unexplored.

Outline of this thesis

In this thesis, we study the presence of moiré excitons at room temperature and explore their combination with high-Q silicon photonic crystal cavities for pushing the working wavelength to the O-band of optical fiber communication (1260-136 nm).

This thesis is structured in the following manner.

In Chapter 1, we provide an overview of excitons in TMDs, which dominate the optical properties of atomically thin TMD layers. Their unique 2D structure contributes to the special electrical and optical characteristics. Next, we introduce the formation and properties of interlayer excitons (IXs) in heterobilayers (HBs) formed by stacking different monolayers. Then we give an overview of the moiré pattern formed in heterobilayers and the experimental observation of moiré excitons trapped in moiré potentials. Finally, we provide an overview of the current state of TMD-based lasers.

In Chapter 2, we focus on the preparation techniques of the samples. Firstly, we discuss the fabrication of MoS_2/WSe_2 heterobilayers, which involves the exfoliation and characterization of high-quality monolayer TMDs, as well as the deterministic transfer technique for monolayer MoS_2 and WSe_2 stacking. Additionally, we describe the nanofabrication process for silicon high-Q cavities and the method employed to transfer the heterostructures onto the photonic cavities.

In Chapter 3, we focus on optical characterization. We discuss the problems we encountered with the old spectrometer and build a multi-functional optical setup from scratch. Using this home-built system, we carry out four different optical measurement techniques, allowing us to comprehensively characterize and investigate our samples.

In Chapter 4, we present the experimental result of MoS_2/WSe_2 heterobilayers on PDMS as revealed through twist angle-dependent PL measurements, power-

dependent PL measurements, and twist angle-dependent differential reflectance spectroscopy. Our findings demonstrate the presence of moiré excitons at room temperature in MoS2/WSe2 HB. Additionally, we study the impact of the moiré potential on the excitons by analyzing the time-resolved PL dynamics.

In Chapter 5, we couple moiré IXs to silicon topological cavities and study the light-matter interaction in a weak-coupling regime. We give a overview of the energy level structure of moiré IX states and the topological nanobeam cavity. By conducting power-dependent PL measurements, we observe low-threshold lasing-like emission in the O-band (1260-1360 nm) of optical fiber communication (OFC). Our device shows the highest spectral coherence compared to all 2D material laser systems to date.

CHAPTER 1

Excitons in transition metal dichalcogenides (TMDs)

This chapter provides a comprehensive overview of excitons in TMDs, ranging from fundamental properties of intralayer excitons in monolayers to interlayer excitons (IXs) in stacked heterobilayers, and their behaviour with the presence of moiré patterns in closely aligned heterobilayers. This chapter also gives an overview of the journey of advancements made in utilizing TMDs as active materials for lasing.

1.1 Two-dimensional transition metal dichalcogenides

Crystal structure of TMDs

Transition metal dichalcogenides (TMD) are layered materials belonging to the two-dimensional material family. They have the chemical formula MX_2, where M is a transition metal atom from group IV (e.g., Ti, Zr, Hf), group V (e.g., V, Nb or Ta) or group VI (e.g., Mo, W), and X is a chalcogen atom (S, Se or Te). As shown in Fig. 1.1(a), a monolayer TMD consists of a transition metal atom layer sandwiched between two chalcogenide atom layers, resulting in a layer thickness of 0.65 nm. In the layer plane, The M atom and X atom are strongly connected by covalent bonds. In bulk crystals, the adjacent layers are held together by the van der Waals forces, which makes it feasible to fabricate monolayer TMDs and combine them with diverse materials. Additionally, TMDs have several phases, so-defined 2H,

3R, and 1T phases [1], as shown in Fig. 1.1(b).

The 1T phase TMD is metallic with octahedral metal coordination. The single layers of the 2H and 3R phases have the same trigonal prismatic coordination but are stacked in two different ways giving hexagonal symmetry (2H) or rhombohedral symmetry (3R). Regarding TMD bilayers, their corresponding stacking orders are called H-stack and R-stack, respectively.

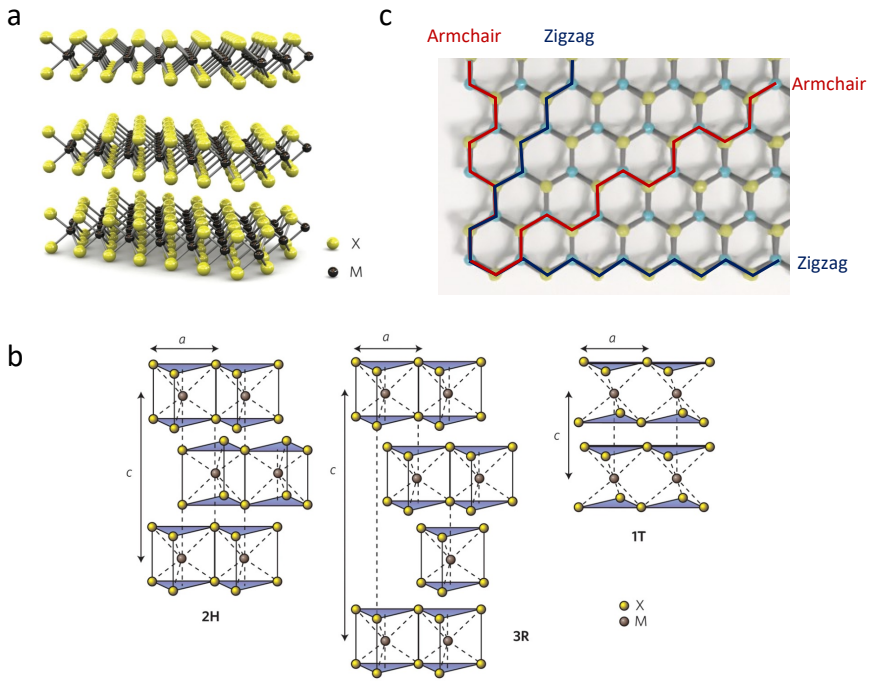

Figure 1.1. Crystal structures of TMDs. (a) Three-dimensional schematic representation of a typical MX_2 structure, with the chalcogen atoms (X) in yellow and the metal atoms (M) in grey, taken from Ref. [18]. (b) Schematics of the structural polytypes: 2H, 3R and 1T, taken from Ref. [18]. (c) The top view of the 2H phase, showing the hexagonal honeycomb lattice. The red and blue curves highlight the crystal axes of the armchair and zigzag, respectively.

The top view of the trigonal prismatic phase is illustrated in Fig. 1.1(c), showing a hexagonal honeycomb lattice. The red and blue curves represent the orientation of the crystal axes, i.e., armchair and zigzag. The armchair axes have broken symmetry inversion, resulting in strong second harmonic generation. This second-order nonlinear generation will be further discussed in Section 3.2.3.

[1]The digit indicates the number of layers in the crystallographic unit cell, and the letter indicates the type of symmetry with T standing for tetragonal (D_{3d} group), H for hexagonal (D_{3h} group), and R for rhombohedral (C^5_{3v} group) [17]

In this dissertation, we focus on the most widely studied compounds of group VI semiconducting TMDs (MoS_2, $MoSe_2$, MoTe2, WS_2, WSe_2). And the monolayers we study are isolated from semiconducting 2H phase bulk crystals.

Bandstructure of TMDs

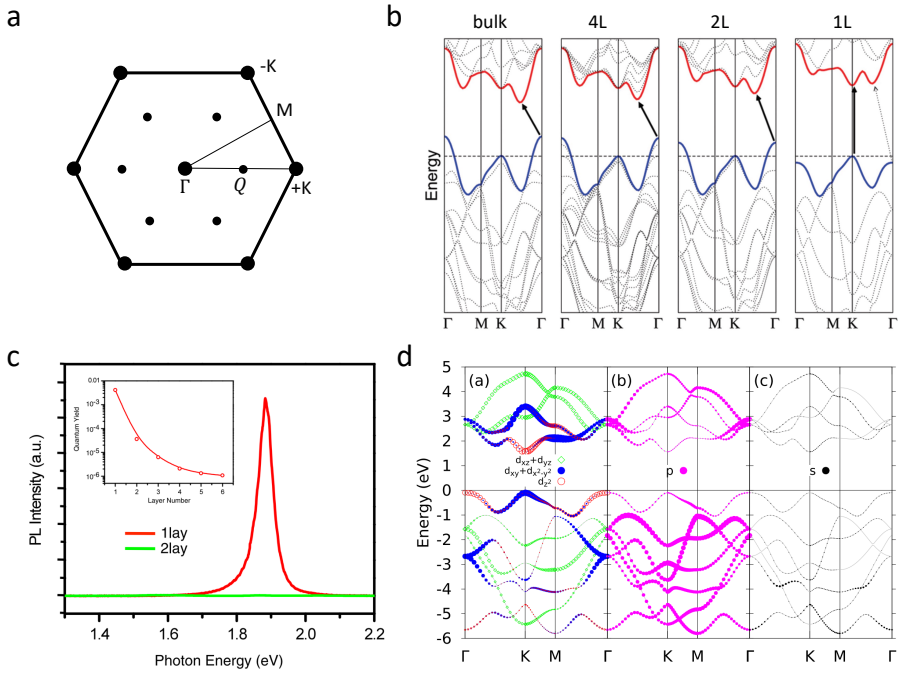

Figure 1.2. Band structures of TMDs. (a) A schematic of the hexagonal 1st Brillouin Zone of the 2H phase TMD. (b) The evolution of the layer-dependent electronic band structure of MoS_2, taken from Ref. [19]. The solid arrows indicate the lowest energy transitions. (c) Layer-dependent PL spectra of MoS_2, taken from Ref. [20]. (d) Orbital projected band structures, taken from Ref. [21]. The *d* orbitals are dominated by M atoms. The *p* orbitals are dominated by X atoms.

Fig. 1.2(a) shows the hexagonal Brillouin Zone of the 2H phase TMD. When TMD bulk material is thinned down to a monolayer, the electronic band structure undergoes a transition from an indirect to a direct bandgap. The evolution of the electronic band structure with layer number is calculated by density functional theory [19], as shown in Fig. 1.2(b). For the monolayer, both the conduction band minimum (CBM) and the valence band maximum (VBM) are located at the K point, resulting in a K-K direct transition. As the layer number increases, the band edges at the

K point remain almost unchanged, while the conduction band edge at the Q point and the valence band edge at the Γ point move closer, leading to a Γ-Q indirect transition. This indirect-to-direct bandgap transition is experimentally confirmed by angle-resolved photoemission spectroscopy [22, 23] and the significant enhancement of photoluminescence in monolayer TMD [20] (see Fig. 1.2(c)).

The reason for distinct layer-dependent responses at K, Γ and Q points come from the different orbital compositions of electronic states [21, 24]. The orbital projected band structures from the first principle calculations are shown in Fig. 1.2(d). The electronic states at the K point are predominantly composed of the *d* orbitals of the M atom. In other words, they are strongly localized in the middle transition metal atom, which is less affected by the adjacent layers. In contrast, the CB states at the Γ point and the VB states at the Q point are linear combinations of M atom *d* orbitals and X atom *p* orbitals, leading to a strong dependence on the interlayer coupling.

In TMD, the M atoms with a heavy mass yield to a strong spin-orbit coupling, resulting in the energy splitting at ±K valleys [2] [25], as shown in Fig. 1.3. The energy splitting in the valence band is around 200 meV for Mo-based TMDs and 400 meV for the W-based, while the splitting in the conduction band is one or two orders smaller than in the valence band (e.g., 3 meV for MoS_2, -37 meV for WSe_2). The resulting spin splitting of the bands gives rise to the so-called spin-valley locking effect, triggering extensive studies on valleytronics [26].

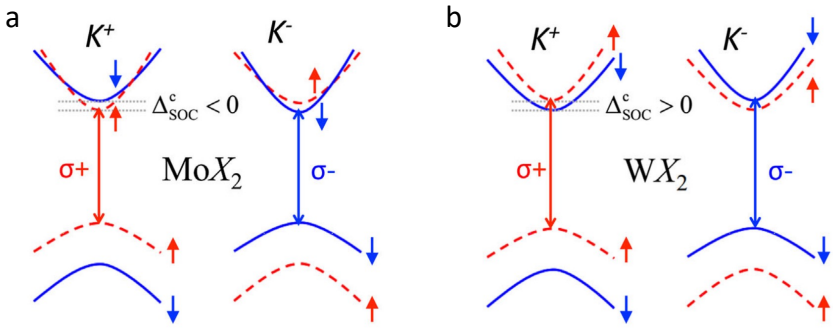

Figure 1.3. Schematic of electron band structures at ±K valleys for Mo- and W based TMD, taken from Ref. [27].

1.2 Excitons in monolayer TMDs

An exciton is a quasi-particle that consists of an electron-hole pair bound by their attractive Coulomb interaction. There are three typical types of excitons [28]: Frenkel

[2]The location of local minimum (maximum) in the conduction (valence) band is regarded as a valley.

excitons, charge transfer excitons and Wannier-Mott excitons. As illustrated in Fig. 1.4(a), Frenkel excitons and charge transfer excitons are localized at an atom and the nearest neighbour molecules, and occur mainly in molecular crystals and ionic crystals, respectively. Wannier-Mott excitons with electrons and holes separated by several lattice constants mainly occur in semiconductors, such as TMD materials and traditional III-V materials. This type of exciton is also called free exciton, as it is free to move inside the crystal. If not specifically stated, the excitons mentioned below mean the Wannier-Mott excitons.

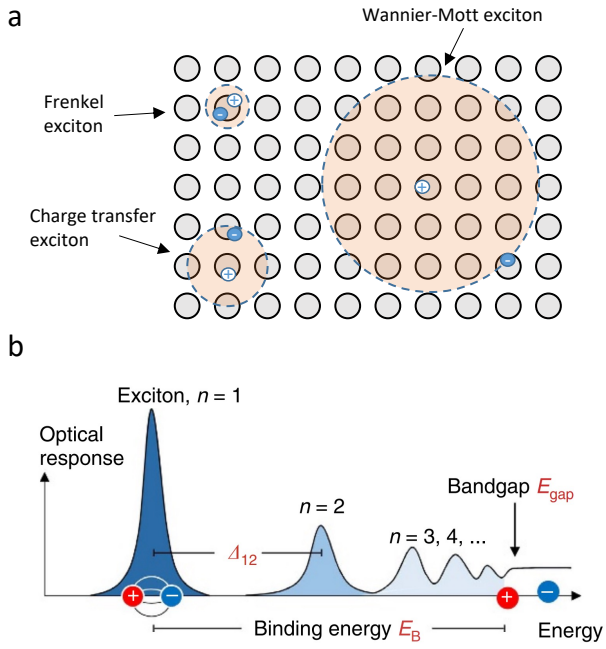

Figure 1.4. Excitons. (a) Schematic illustration of Frenkel excitons, charge transfer excitons and Wannier-Mott excitons in a crystal. (b) Schematic illustration of the optical response of excitons in an ideal 2D semiconductor, including exciton ground (n=1) and excited (n>1) state resonances and the onset of the (quasiparticle) bandgap, taken from Ref. [29].

Analogous to the hydrogen atom, a series of exciton Rydberg states emerges below the free quasi-particle bandgap, which is labelled by their principal quantum number n (n=1,2,3,...), as shown in Fig. 1.4(b). The energy difference between the bandgap and the exciton resonance defines the exciton binding energies E_B, which is the energy required to ionize the bound exciton into a free hole and electron. The binding energy of exciton states depends on the principal quantum number. For the exciton ground

state (n=1), E_B is defined as [28]

$$E_B = \frac{(m_r/m_0)}{\varepsilon^2} Ry(H) \tag{1.1}$$

where $m_r = m_e m_h/(m_e + m_h)$ is the reduced mass of exciton, m_0 stands for the free exciton mass and ε is the dielectric permittivity, and $Ry(H)$ =13.6 eV is the Rydberg constant. For traditional bulk GaAs (InP) semiconductors, the exciton binding energy is ∼4.2 meV (∼5.1 meV). The binding energy will increase to ∼9 meV for the quasi-2D exciton in a GaAs quantum well of a width less than 10 nm [30]. These excitons can only exist at low temperatures, as the thermal energy at room temperature is about 25 meV. Remarkably, the binding energy of monolayer TMD is on the order of 500 meV, making it stable even at room temperature. Fig. 1.5(a) shows the impact of the dimensionality on the electronic and excitonic properties. In the 2D limit, the electrons and holes are strongly confined in an atomically thin layer, and a large proportion of the electric field is outside the crystal. The variation of the dielectric environment of monolayer TMD changes the exciton binding energy by several hundred meV [29], see in Fig. 1.5(b). In addition, the reduced masses of excitons in monolayer TMD are on the order of $0.25m_0$, which are larger than that of GaAs ($0.06m_0$) [24]. The dimensionality, reduced dielectric screening, and large reduced masses contribute to enhanced exciton binding energy. The large exciton binding energy yields strong excitonic effects that dominate the optical properties of monolayer TMD.

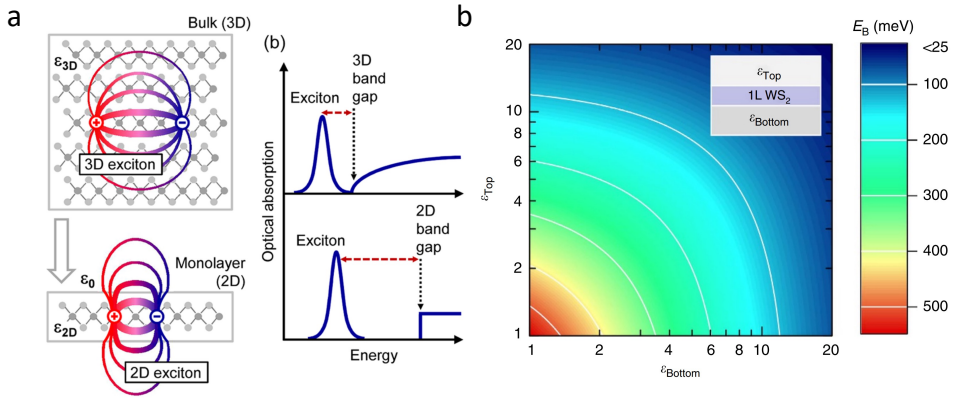

Figure 1.5. Binding energy of atomically thin TMD layer. (a) Impact of the dimensionality on the electronic and excitonic properties. Left panel: electric-field distribution of excitons in real space for 3D bulk and 2D monolayer; Right panel: optical absorption indicates reduced dimensionality increases both band gap and exciton binding energy; taken from Ref. [31]. (b) Impact of the dielectric environment on exciton binding energy in monolayer TMD, taken from Ref. [29].

Excitons in monolayer TMD can be either optical bright or dark depending on whether they satisfy the optical selection rule, which requires energy, spin, and momentum conservation. Due to the strong SOC, the spin splitting in ±K valleys gives rise to the formation of two bright excitonic states, A and B excitons, corresponding to the lower and higher energy exciton, respectively. These excitons have been widely observed in optical absorption spectra [32, 33].

Additionally, TMD monolayers exhibit unique valley-dependent optical selection rules, as shown in Fig. 1.6(a). The +K and -K valleys are degenerate in energy, but their sign in spin splitting is opposite due to the broken time-reversal symmetry (Fig. **??**). Therefore, the transition in the +K (-K) valley only couples to right-handed $\sigma+$ (left-handed $\sigma-$) circularly polarized light. The spin-valley locking effect has been observed in experiments [33,34] through the utilization of incident circularly polarized light with analysis performed on the polarization of exciton emission. The circular polarization degree [3] of monolayer MoS_2 is reported to achieve unity at 14 K, which persists over 1 ns [33]. However, the valley polarization decreases with the temperature increase (see Fig. 1.6(b)), due to the increased inter-valley scattering at high temperatures. When warmed up to room temperature, the valley polarization of monolayer MoS_2 totally vanishes [33, 34].

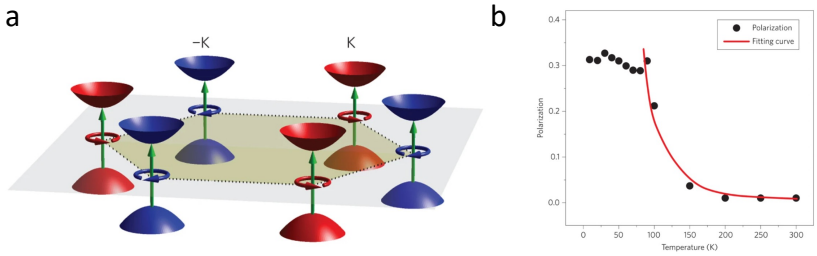

Figure 1.6. Spin-valley locking effect. (a) Schematic of valley-dependent optical selection rules, showing that the transition in the +K (-K) valley only couples to right-handed $\sigma+$ (left-handed $\sigma-$) circularly polarized light, taken from Ref. [25]. (b) Degree of circular polarization as a function of temperature, taken from Ref. [34].

1.3 Interlayer excitons in heterobilayers

The van der Waals structure of TMD crystal enables one to tailor material properties by simply stacking two different monolayers without the need for lattice matching. The various TMD monolayers have different bandgaps and band offsets, as shown in

[3] The circular polarization degree is defined as $p = \frac{I(\sigma+)-I(\sigma-)}{I(\sigma+)+I(\sigma-)}$, where $I(\sigma+)$ and $I(\sigma-)$ are the PL intensities of $\sigma+$ and $\sigma-$, respectively.

Fig 1.7(a). Their multiple combinations enrich the exciton physics in TMD heterobilayaer systems. Depending on the band alignment of the constituting monolayers, the heterobilayer can be classified into three categories: straddling gap (type-I), staggered gap (type-II), and broken gap (type-III), as illustrated in Fig. 1.7(b). In this dissertation, we focus on the TMD heterobilayer with type-II band alignment, in which the CBM and VBM locate at different layers, leading to the emergence of interlayer excitons (IXs).

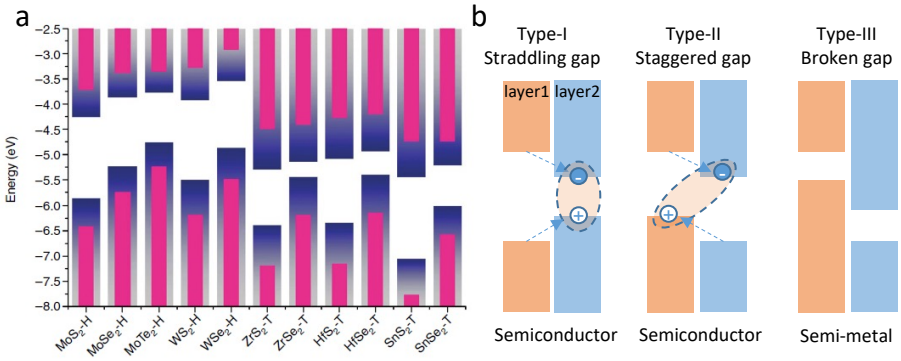

Figure 1.7. Band alignment of heterobilayers. (a) Band offset for various material combinations, taken from Ref. [25]. (b) Three types of band alignment. Type-I: The carriers can only transfer from one layer with the larger bandgap to another layer with the smaller bandgap, but not vice versa [35, 36]. Type-II: the CBM and VBM are situated in different layers, resulting in a reduced band gap. Type-III: the CBM and VBM locate at different layers, with the VBM energy higher than the CBM. As a result, the band gap does not exist, making it a semi-metal material.

A distinctive characteristic of IXs is the emergence of a new peak at low energy in the PL spectrum, as shown in Fig. 1.8(a). The formation process of IXs is depicted in Fig. 1.8(b). It involves three steps:

1. Under optical excitation, the interband optical absorption leads to the generation of intralayer excitons in monolayers.
2. Due to the band offsets, the excited intralayer excitons in monolayers separate into electrons in one layer and holes in the other via an ultrafast charge transfer process (<50 fs) [37]. This process is mediated by the strongly layer-hybridized Q(Γ) valley for the electron (hole) transfer [38].
3. These electrons and holes are bonded together through attractive Coulomb interaction, yielding IXs.

Because the formation of IX is a consequence of the dissociation of excitons resident in the same layer, the emission of intralayer exciton is strongly quenched, which is a good indicator of interlayer coupling.

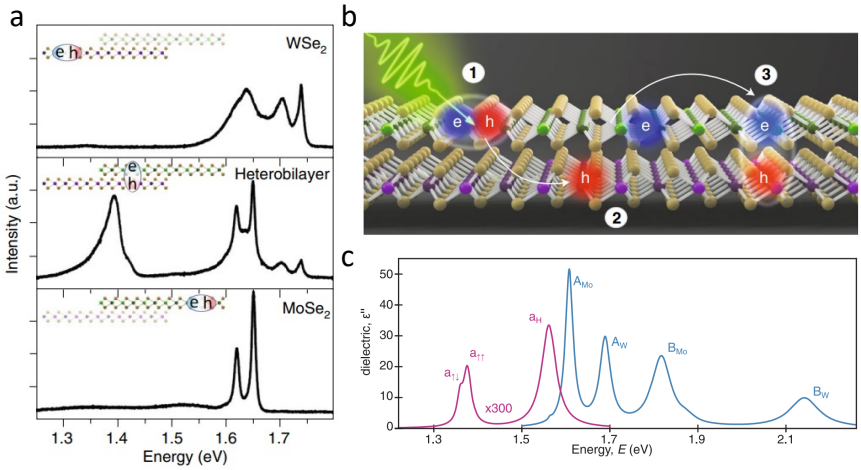

Figure 1.8. Optical properties of IXs. (a) PL spectra from $MoSe_2/WSe_2$ heterobilayers and individual monolayers, taken from Ref. [39]. (b) Illustration of the IX formation process in MoS_2/WS_2 heterostructures as revealed by transient absorption spectroscopy, taken from Ref. [40]. (c) The imaginary dielectric function obtained from electro-modulation spectroscopy (magenta) and from typical reflection contrast method (blue) in $MoSe_2/WSe_2$ heterobilayers, taken from Ref. [41].

Optical properties of IXs

As mentioned in Section 1.1, the interlayer coupling at Q/Γ valley is strong in multilayer TMDs, which can lead to an indirect band gap. In the case of heterobilayers, calculation and experiment show that the CBM and VBM are predominantly located at the ±K valleys in individual layers, resulting in fundamental bright K-K exciton [42, 43]. The spatially separated electrons and holes still experience strong Coulomb interaction and thus the formed IXs exhibit a large binding energy ∼150 meV [39].

Due to the spatial separation between electrons and holes, the oscillator strength of IX is so weak that its optical absorption is challenging to be measured by the typical reflection contrast method. A recent breakthrough in the field comes from the research conducted by Tony F. Heinz's group. By using electro-modulation spectroscopy, they directly measured the absorption of IX and reported that the IX oscillator strength is three to four orders of magnitude smaller than that of intralayer exciton [41] (see Fig. 1.8(c)).

Owing to the small wave function overlap of electrons and holes, the recombination of IX is suppressed, leading to a long exciton lifetime (∼ns) [39, 44], which is orders of magnitude longer than lifetimes of intralayer excitons (∼ps). The long lifetime will allow IXs to cool down and potentially create a degenerate exciton gas.

A remarkable achievement by Kin Fai Mak and Jie Shan's group is the observation of exciton condensation at high temperatures (> 100 K) [45]. A two- to three-layer hBN is inserted between the $MoSe_2/WSe_2$ van der Waals heterobilayer in order to further suppress interlayer electron–hole recombination. Additionally, the extended lifetime is beneficial to laser applications [14, 15], as it facilitates the establishment of a population inversion and results in a low-threshold lasing.

Tunability of IXs

IXs show richer tunability compared to intralayer excitons. The light emission of IXs can be tailored by changing the constituting material, applying external stimuli (e.g., electric field and strain), and tuning the twist angle of bilayers. We will now discus each of these tuning mechanisms in more detail.

Constituting material

Stacking of monolayers with different band offsets will tailor the existing excitonic states and tune their emission energies. For example, in $MoSe_2/WSe_2$ heterobilayers, the IX emission energy is $\sim$1.35 eV [46], and IX in MoS_2/WSe_2 has a lower energy of $\sim$1 eV [47]. In the case of $WS_2/MoSe_2$ heterobilayers, the small conduction-band offset leads to hybridization between the corresponding intra- and interlayer exciton transitions where the electron resides in both layers, referred to as hybrid excitons [48, 49].

Electric field

IX has a permanent out-of-plane electric dipole moment, thus has shown excellent electrical tunability (energy tuning range from 80 to 200 meV) by applying a vertical gate voltage [47, 50] (see Fig. 1.9(a)). The shift in IX energy $\triangle\varepsilon$ exhibits a linear dependence with bias voltage E due to the linear Stark effect and can be expressed as $\triangle\varepsilon = -ed \cdot E$, where e is electron charge and d is electron-hole interlayer separation. The derived d value is approximately 0.5-0.8 nm, corresponding to the interlayer distance of the heterobilayer. In addition, the lifetime also depends on the applied electric field. When the electric field antiparallel to the IX dipole moment, it pulls the two carriers apart and changes the overlap between the electron and hole wave functions, thus reducing the IX recombination rate and extending the IX lifetime [50].

However, the IX electric dipole illustrated in Fig. 1.8(b) is actually not entirely accurate. Strictly speaking, the majority of dipoles are oriented in-plane. A complete out-of-plane orientation would challenge the vertical excitation and collection of IX resonance. In 2022, Alexander W. Holleitner's group successfully obtained the contributions of the in- and out-of-plane transition dipole moments in $MoSe_2/WSe_2$ heterobilayers by measuring the far-field PL intensity distribution of IX [51]. They concluded that the transition dipole moments for all observed interlayer exciton transitions were $(99 \pm 1)\%$ oriented in-plane. The dominated in-plane orientation can also be inferred from the Bohr radius of IX. In 2022, Keshav M. Dani and Tony F. Heinz's group reported a direct measurement of IX diameter of around 5.2 nm [52]

in MoS_2/WSe_2 heterobilayers. This value is significantly larger than the interlayer distance of 0.65 nm.

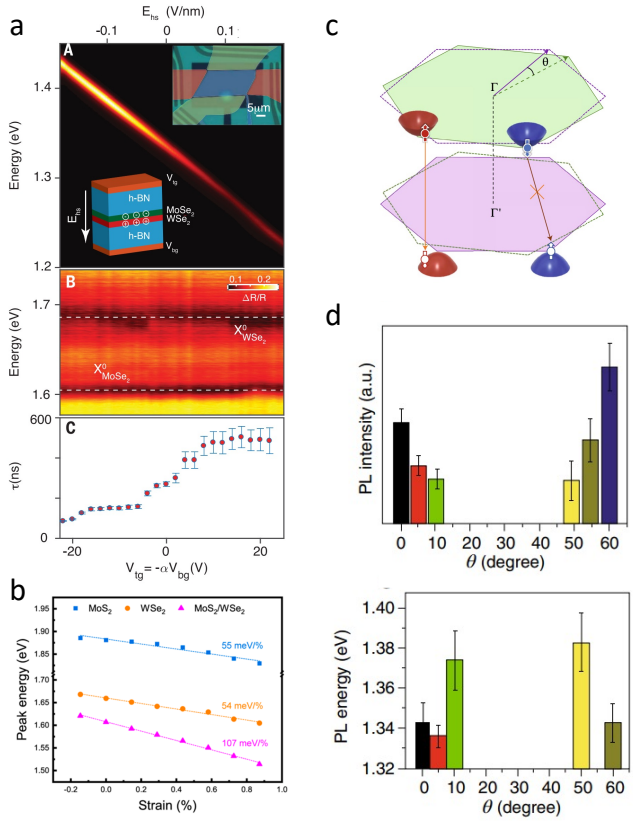

Figure 1.9. Engineering of IX properties. (a) IX emission energy (top), intralayer exciton emission energy (middle) and IX lifetime (bottom) as a function of applied vertical electric fields, taken from Ref. [50]. (b) Exciton energy shift as a function of uniaxial strain, taken from Ref. [53]. (c) Displacement of CB and VB edges in momentum space due to the twist angle between two constituent layers, taken from Ref. [40]. (d) PL intensity of IX (top) and IX emission energy (bottom) as a function of the twist angle, taken from Ref. [54].

Strain

A TMD monolayer can withstand a strain on the order of 10% [55,56]. The applied strain tunes the lattice constant of the monolayers, resulting in a change in the band structure. In MoS_2/WSe_2 heterobilayers, the bandgap change of Γ-K IX transition is around 107 meV/% uniaxial strain, approximately twice that of the intralayer excitons in the constituent monolayers (55 meV/% for MoS_2 and 54 meV/% for WSe_2) [53] (Fig. 1.9(b)). The shift for the indirect-band gap peak for $MoSe_2/WSe_2$ (22.7 meV//% strain) is about twice that of the K-K transition (11.2 meV//% strain). The strain

dependence can be used to verify the transition from different valleys, as the valence band at the K valley is insensitive to strain [57]. Through strain tuning, type-II band alignment can even transform to type-I in the MoS_2/WSe_2 lateral heterojunction [58].

Twist angle

The twist angle between the two layers leads to a displacement of the conduction and valence band edges at ±K valleys in momentum space, as illustrated in Fig. 1.9(c). A small momentum mismatch can be compensated for by the finite exciton center-of-mass momentum to a direct transition. Otherwise, assistance from phonons or impurities is required for radiative recombination [59].

Fig. 1.9(d) shows the IX PL intensity and energy from $MoSe_2/WSe_2$ heterobilayers as a function of the twist angle [54]. The strongest PL intensity is observed when the twist angle is close to 0° (or 60°) and gradually vanishes beyond 10° (or $< 50°$). And the IXs emission energy rises as the twist angle increases. In addition, the IX lifetimes also dramatically change with twist angle by one order of magnitude [60].

Furthermore, the presence of twist angle and/or lattice mismatch between the two layers generates a long-period moiré pattern in the heterobilayer, giving rise to intriguing phenomena. In the forthcoming section, we will delve into a detailed exploration of the impact of moiré patterns on excitons.

1.4 Excitons in moiré superlattices

The superposition of atomic lattices in two layers can give rise to a periodic spatially varying atomic registry known as moiré patterns, as illustrated in Fig. 1.10(a), which exhibits a larger-scale periodicity than the lattice constant. This intriguing moiré pattern emerges due to a small lattice mismatch δ and/or small twist angle θ between two constituent layers. The moiré period a_M can be given by $a_M \approx a_0/\sqrt{\delta^2+\theta^2}$ [61], where the lattice constant mismatch δ is defined as $\left|a_0 - a_0^{'}\right|/a_0$, and a_0 and $a_0^{'}$ are the lattice constants of the two layers.

The R- and H-typed heterobilayers exhibit a similar moiré superlattice. Here, we employ the R-typed heterobilayer as an illustrative example. The superlattice hosts three types of high-symmetry points, which are labelled as $R_{\mathrm{h}}^{\mathrm{h}}$, $R_{\mathrm{h}}^{\mathrm{X}}$ and $R_{\mathrm{h}}^{\mathrm{M}}$, representing that the hexagonal centre (h) in the hole layer is aligned to the hexagonal lattice centre (h), chalcogen atom (X) or metal atom (M) in the electron layer respectively. The interlayer spacing varies with different atomic registries, resulting in the change of local bandgap (see Fig. 1.10(b)) and forming a periodically modulating energy landscape, known as moiré potential (Fig. 1.10(c)). The optical selection rules for IX depend on the local atomic registry, e.g., the exciton residing at the $R_{\mathrm{h}}^{\mathrm{h}}$ ($R_{\mathrm{h}}^{\mathrm{X}}$) site only couples to $\sigma+$ ($\sigma-$) polarized light (Fig. 1.10(d)). The confined excitons in the moiré potential are commonly denoted as moiré excitons, which hold promises in realizing identical quantum emitter arrays [62] and trigger immense enthusiasm within this research field.

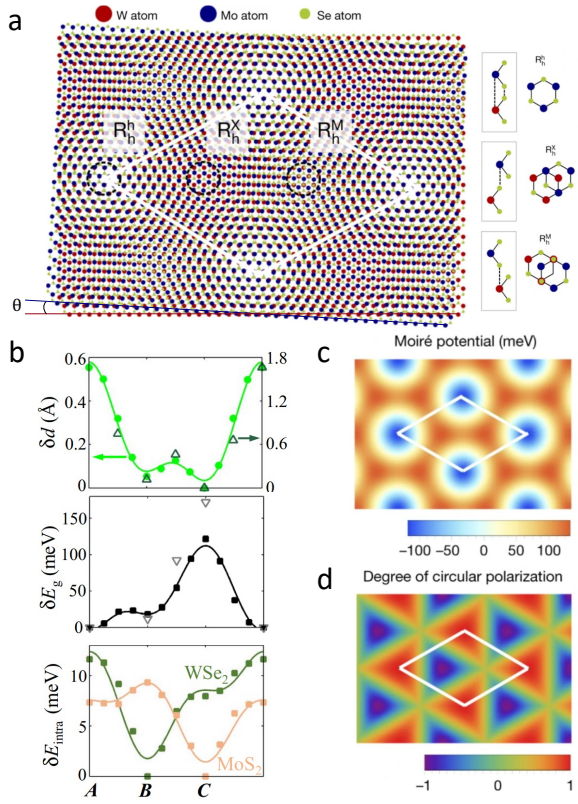

Figure 1.10. Moiré superlattices. (a) Illustration of a R-type moiré superlattice (white diamond shape) formed by stacking monolayer $MoSe_2$ and WSe_2 with a twist angle θ. Three high symmetry points are labelled as R_h^h, R_h^X and R_h^M. Their local atomic registry is shown on the right, taken from Ref. [46]. (b) Dependence of interlayer distance (top), the local bandgap of IX (middle) and intralayer excitons (bottom) on the atomic registries, taken from Ref. [62]. (c) Potential distribution of IXs in moiré superlattices, taken from Ref. [46]. (d) Degree of circular polarization of IX in moiré superlattice, taken from Ref. [46].

Observation of moiré excitons

Despite the growing interest in moiré excitons, experimental detection of their existence has not been achieved until 2019, when four works [46, 48, 63, 64] independently reported the evidence of moiré excitons were published back-to-back in Nature. Among them, two research groups have reported the observation of moiré IX in the same type of heterobilayer ($MoSe_2/WSe_2$ heterobilayer). Xiaoqing Li's group [46] reported the multiple IX PL peaks (Fig. 1.11(a)). They attributed them to quantized energy levels due to the confinement of IXs within the moiré potential (see the bot-

tom panel in Fig. 1.11(a)). The resonance spacing in the ∼2° sample (∼27 meV) was larger than that in the ∼1° sample (∼22 meV) due to the tighter lateral quantum confinement of the ∼2° sample. Xiaodong Xu's group observed narrow IX emission peaks with a linewidth of ∼80 μeV at a low excitation power of ∼10–100 nW [63]. The narrow-line emission is suppressed at temperatures greater than 30 K. The sharp resonance is believed to originate from IX trapped in zero-dimensional moiré potentials, akin to quantum dots. The quantum nature of the sharp emission lines is further confirmed by power saturation and photon antibunching behaviour in other works [65]. Interestingly, in 2022, John R. Schaibley's group reported that the narrow IX resonances come from extrinsic fluctuations instead of moiré potentials [64]. This conclusion is drawn based on the findings that narrow resonances still persist when suppressing the moiré potential by inserting a bilayer hBN spacer between the TMD layers, and it exhibits a similar dependency on doping, electric field, and temperature.

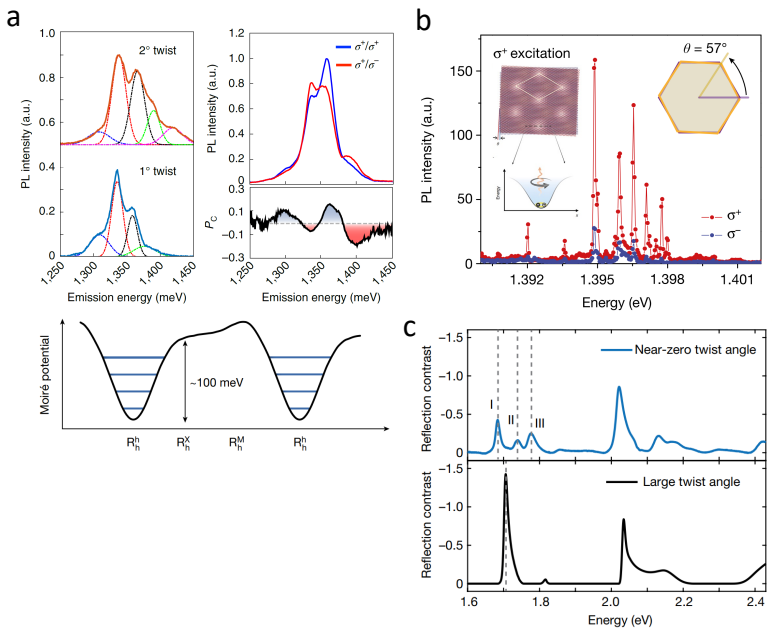

Figure 1.11. Initial experimental demonstrations of moiré excitons at low temperatures. (a) Multiple IX resonance in PL spectra in $MoSe_2/WSe_2$ heterobilayers with twist angle of 1° and 2° at 15 K, taken from Ref. [46]. (b) Helicity-resolved narrow IX PL spectra of twisted $MoSe_2/WSe_2$ heterobilayer at 1.6 K, taken from Ref. [63]. (c) Multi absorption peak around WSe_2 A exciton in rotationally aligned WS_2/WSe_2 heterobilayers compared to those with a large twist angle at 10 K, taken from Ref. [66].

The presence of moiré potential not only can trap IXs, but also affect the optical properties of intralayer excitons. Theoretical calculations predict that the moiré

potential results in the energy splitting of intralayer excitons [67]. Feng Wang's group observed that the WSe_2 A exciton splits into three multiple peaks in the absorption spectra of WS_2/WSe_2 heterobilayer with a twist angle smaller than 3° at 10 K [66]. And the phenomenon is well reproduced by their theoretical model where sufficient moiré potential generates multiple flat exciton minibands.

In addition to these observations based on far-field optical spectroscopy, the existence of moiré excitons was demonstrated by time-resolved and angle-resolved photoemission spectroscopy [52, 68], exciton transport measurements [69], and electron-beam-based hyperspectral imaging [70]. First-principles calculations have predicted the moiré potential depth to be approximately 100–200 meV [46, 62, 71]. In 2017, Chih-Kang Shih's group employed scanning tunnelling microscopy (STM) and scanning transmission electron microscopy (STEM) to directly measure the moiré pattern in a rotationally aligned MoS_2/WSe_2 heterobilayer (Fig. 1.12(a)). Their result shows a periodically varying interlayer separation and electronic bandgap, indicating a periodic moiré potential modulation up to 150 meV [71], which remarkably exceeds the thermal energy (∼25 meV) at room temperature. A very recent experiment [72] correlates the multipeak feature in IX emission spectra from free-standing WS_2/WSe_2 heterobilayers with moiré IXs (see Fig. 1.12(b)), however still lacking strong evidence for the presence of moiré IX at room temperature.

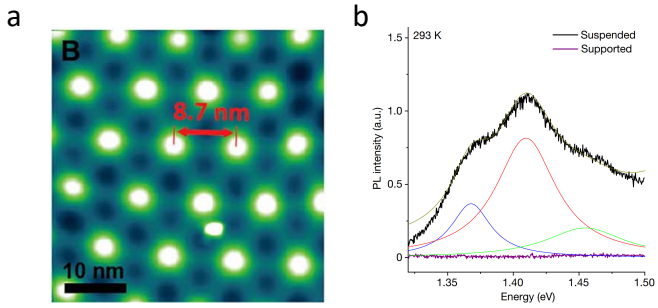

Figure 1.12. Experimental demonstrations of moiré excitons at room temperature. (a) STM image of moiré pattern in MoS_2/WSe_2 heterobilayers, taken from Ref. [71]. (b) Multiple IX resonance in suspended WS_2/WSe_2 heterobilayers, taken from Ref. [72].

Atomic reconstruction of moiré patterns

The ideal moiré pattern is a rigid lattice with the atomic registry varying smoothly. However, atomic reconstruction is known to occur in twisted bilayer graphene [73] and has been observed heterobilayers with a small twist angle and a small lattice mismatch [74, 75].

The superlattice will relax and expand the regions of lowest energy to reduce the overall energy, leading to discrete commensurate domains separated by narrow

domain walls [74] (Fig. 1.13(a)). Thus the exciton does not experience lateral confinement, exhibiting a behaviour that closely resembles that of commensurate domains. Multiscale modelling shows that atomic reconstruction only appears in near-commensurate heterobilayers with twist angle $\theta < 2.5°$ or $\theta > 59°$ [76]. Whereas heterobilayers with large angle or large lattice mismatch behaves as almost rigid crystals. The crossover angle is in agreement with TEM results ($\theta < 2°$ or $\theta > 59.1°$) [75].

The atomic reconstruction leads to in-plane strain redistribution and is reported to contribute to moiré flat bands in incommensurate heterobilayers [70, 77]. Direct imaging of reconstruction in a rotationally aligned WS_2/WSe_2 moiré superlattice was achieved by annular dark-field scanning transmission electron microscopy (ADF-STEM) [70]. In conjunction with low-loss electron energy-loss spectroscopy (STEM-EELS), it was observed that the moiré intralayer exciton is restricted to a radius of $\sim$2 nm at the R_h^h site. Note that the EELS measured the local probability of creating an exciton rather than the excitons themselves.

Further, it has been reported that the atomic reconstruction includes both a large in-plane strain distribution and a prominent out-of-plane buckling by comparing scanning tunnelling spectroscopy (STS) with ab initio simulations [78], as shown in Fig. 1.13(b). The strong 3D reconstruction dominates the effective moiré potential and the corresponding moiré flat bands.

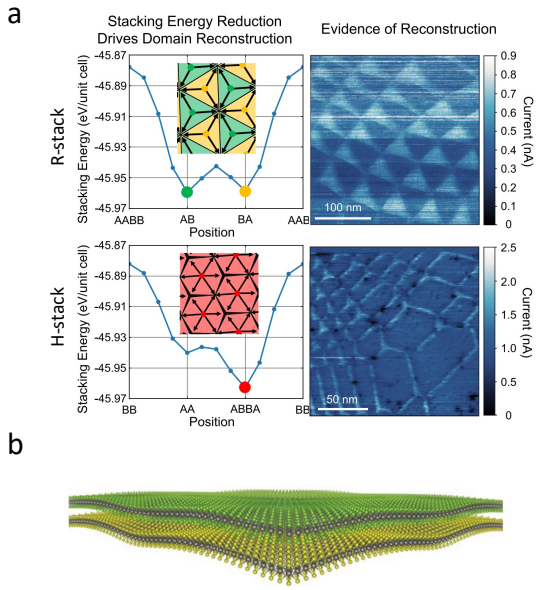

Figure 1.13. Atomic reconstruction of moiré superlattices. (a) Atomic reconstruction in $MoSe_2/WSe_2$ heterobilayers. Left panel: Interlayer stacking energy at various atomic registries. Right panel: Conductive AFM images, taken from Ref. [74]. (b) Schematic of the reconstructed moiré superlattices in 3D, taken from Ref. [78].

1.5 Lasers based on atomically thin TMDs

Van der Waals TMDs have gained significant attention due to their strong excitonic emission, which holds the immense potential of ultralow threshold lasing. So far, lasers based on atomically thin TMDs have been successfully demonstrated in conjunction with various photonic cavities. In this section, we give an overview of the remarkable progress in utilizing TMDs as active materials for lasing.

The first demonstration of a TMD-based laser was reported by Xiaodong Xu's group in 2015 (Fig. 1.14(a)). By coupling monolayer WSe_2 to an L3 photonic crystal (PhC) cavity, they show evidence of lasing at 740 nm with an optical pumping threshold as low as 27 nW (1 W/cm^2) at 130 K [79]. In the same year, Xiang Zhang's group reported a monolayer excitonic laser from a monolayer WS_2 coupled to a microdisk resonator at 10 K [80]. Lasing happened at the visible wavelength ($\sim$ 612 nm) at a threshold of 5-8 MW/cm^2.

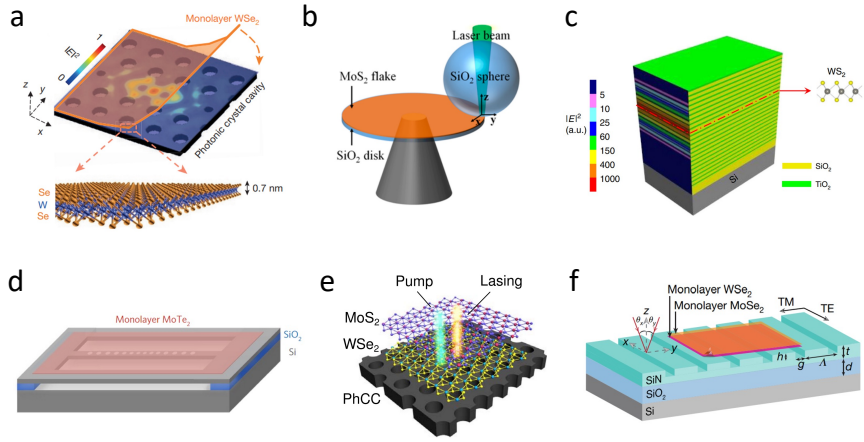

Figure 1.14. Experimental demonstrations of lasers based on TMDs. (a) The first demonstration of lasing from monolayer WSe_2 coupled to L3 PC cavities at low temperature, taken from Ref. [79]. (b) The first demonstration of room-temperature lasing from MoS_2 embedded between a silica microsphere and a microdisk cavity, taken from Ref. [81]. (d) Single-mode lasing from monolayer WS_2 embedded in DBRs, taken from Ref. [82]. (c) The first demonstration of room-temperature silicon-integrated lasing from monolayer $MoTe_2$ integrated with a Si nanobeam cavity, taken from Ref. [11]. (e) Interlayer exciton lasing from a MoS_2/WSe_2 heterobilayer on a L3 type silicon PC cavity, taken from Ref. [14]. (f) Interlayer exciton lasing from a $MoSe_2/WSe_2$ heterobilayer on a grating cavity, taken from Ref. [15].

Soon after, Zetian Mi's group achieved the first room-temperature TMD laser at a wavelength range of 600 - 800 nm [81] (Fig. 1.14(b)). Four-layer MoS_2 was embedded between a silica microsphere and microdisk cavity, which significantly enhanced

the coupling between the gain medium and the optical cavity modes, leading to an ultralow lasing threshold (∼5 µW). In 2017, a single-mode laser was realized by burying monolayer WS_2 into TiO_2/SiO_2 DBR cavities (Fig. 1.14(c)), showing an ultra-low lasing threshold (0.44 W/cm^2) [82].

Then, the lasing wavelength is further extended to near-infrared through the utilization of $MoTe_2$ material, thereby achieving compatibility with the silicon platform. Cunzheng Ning's group reported the first silicon-integrated TMD laser at ∼1130 nm from silicon nanobeam cavities [11] (Fig. 1.14(d)). Subsequently, Xuehua Wang's group extended this wavelength to ∼1310 nm, encompassing the OFC O-band, and achieved the single-mode $MoTe_2$-on-silicon laser [13].

In type-II heterobilayers, ultrafast interlayer charge transfer and extended IX lifetime allow efficient accumulation of carriers and the establishment of population inversion. In 2019, IX lasers have been realized in MoS_2/WSe_2 [14] and $MoSe_2/WSe_2$ [15] heterobilayers. Weibo Gao's group observed IX lasing at 1128 nm from silicon L3 photonic crystal [14] (Fig. 1.14(e)). Most TMD-based lasers are demonstrated by superlinear light in-light out (L-L) curve and linewidth narrowing. Here, they also observed an increase in coherence time above the lasing threshold by performing Michelson interference experiments. The other work from Hui Deng's group demonstrated IX lasing at 918 nm using a Si_3N_4 grating cavity [15] (Fig. 1.14(f)). They measured an abrupt increase in first-order spatial coherence from 2.38 µm to 5 µm across the threshold. It is worth noting that the Q-factor of their cavities is much lower (around 500-600) than that of intralayer exciton lasers, thanks to the nature of IX.

1.6 Goal of this PhD project

The additional confinement on IX with moiré potential holds great promise for laser applications. Although great achievements in moiré excitons and TMD-based lasers have been made, the question about the existence of moiré IX at room temperature and their potential for laser applications still needed to be answered. In this project, we will focus on answering these two questions.

CHAPTER 2

Fabricating TMD heterostructures and photonic crystal cavities

To couple IX to the cavity mode, we need to prepare a MoS_2 -WSe_2 heterobilayer and place it onto the cavity. However, this process can be challenging without the use of a thin layer of bottom hBN. Encapsulating the heterobilayer between two hBN flakes brings many benefits, such as preventing degradation of the heterobilayer, creating a uniform dielectric environment and increasing heat dissipation. In this chapter, we will focus on the preparation process of the ultimate device, hBN/MoS_2/WSe_2/hBN heterostructures on the cavity, which is divided into two main sections.

The first section presents the exfoliation and stacking of 2D materials. In this process, the most important objective is to maintain a clean interface between materials, avoiding any impurities that may affect the optical properties by causing non-radiative recombination. We will discuss the exfoliation method for 2D materials and some details that need attention during the process. We will also explain how we maintain an interface that is as clean as possible to prepare high-quality heterobilayers, which are crucial for our later research on moiré excitons.

In the second section, we introduce the fabrication method for a silicon-based high-Q microcavity, which involves a series of standard silicon nanofabrication techniques. This is a relatively mature process, and the recipe has already been developed by DTU Nanolab. We will mainly focus on how we use the existing techniques to explore suitable parameters for processing and preparing our microcavity, and ultimately achieve a high-Q cavity. The transfer of heterostructures onto microcavities is also addressed in the first section dedicated to transfer techniques.

Overall, this chapter will provide a detailed introduction to the process of sample and device fabrication. We believe that the content of this chapter can help readers better understand our research and provide valuable references for future work.

2.1 Mechanical exfoliation

To obtain high-quality heterostructures, it is necessary to first fabricate high-quality monolayer TMDs. We employ the standard method of mechanical exfoliation, which takes advantage of the lack of covalent bonds between layers in 2D materials to thin bulk crystals down to atomic thickness. This technique results in better optical properties for monolayers than other methods, although it has the drawbacks of limited area and time-consuming preparation. The quality of the obtained monolayers ultimately depends on the quality of the bulk crystal. For instance, the flux-grown TMDs have significantly fewer defects than CVT-grown ones [83]. Fig 2.1 shows the pictures of bulk crystals. During the exfoliation process, it is crucial to maintain a clean and flat surface to avoid introducing impurities that could reduce the quality. We aim for large flakes with long straight edges that can facilitate angle alignment during the later stacking process.

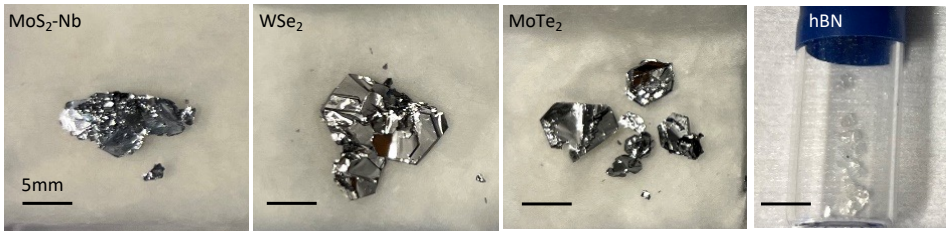

Figure 2.1. Picture of bulk crystals of MoS_2, WSe_2, $MoTe_2$ and hBN bought from HQ Graphene.

The process to achieve monolayer TMD flakes can be divided into three parts: preparation of master tapes, transfer to substrate and monolayer identification.

Preparation of a master tape

The preparation of a master tape is the cornerstone of monolayer TMD fabrication. A good master tape should have large thin flakes without cracks as well as low tape residues, which will increase the yield of getting a clean monolayer with a large size. The first graphene layer has been obtained via Scotch tape which is commonly used in office settings and leaves significant residue. To get a cleaner surface, a silicone-free adhesive film is widely employed. The adhesive film is often used in semiconductor wafer processing and provides a much cleaner process and more consistent adhesive properties. It also known as blue tape due to its blue colour and will be referred to as such in the subsequent discussion. Here we use the blue tape 1007R-6.0 (from Ultron Systems, Inc.), and the steps to obtain a master tape are the following:

1. Put a bulk crystal onto a small piece of blue tape and cover it with another piece.

2. Apply gentle pressure with your finger to ensure good contact between the tape and the surface of the crystal.

3. Slowly peel the two pieces of blue tape apart and store the bulk crystal if it can be picked up with tweezers.

4. Put tapes together at an angle to avoid overlap of flakes, and repeat steps 2-4 until around one-third of the flakes lose metallic luster. If the tape is full of thick flakes, use a fresh piece of blue tape.

To get a good master tape, try to avoid folding the tape and reduce repeating step 2-4. Good contact between the tape and the flakes is important as it keeps the flakes intact.

Transfer on substrate

When a master tape is ready (Fig 2.3(a)), we can place it onto a substrate of interest, and peel the master tape off.

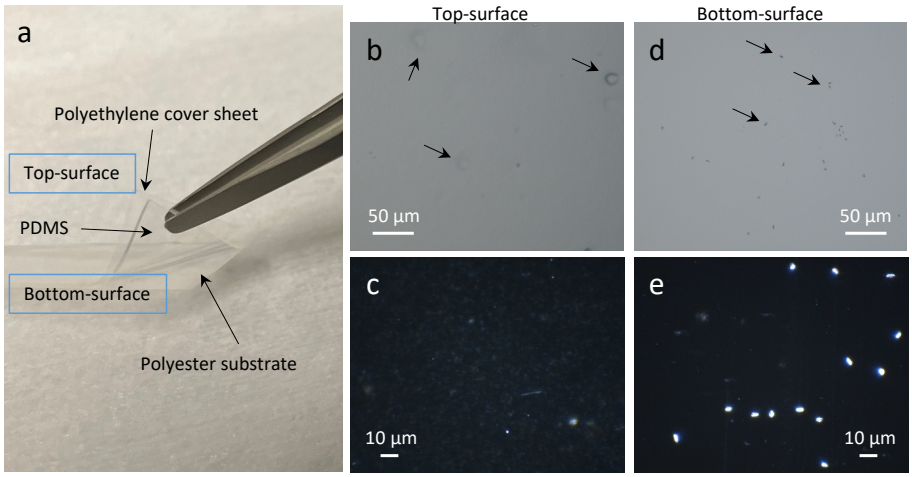

Figure 2.2. Surfaces of double-sided PDMS film. (a) Image of the PDMS film, consisting of three layers: polyester substrate, gel material and polyethylene cover sheet. Optical microscope image of the top surface between gel material and polyethylene cover sheet, in bright field (b) and dark field (c).Optical microscope image of the bottom surface between gel material and polyester substrate, in bright field (d) and dark field (e).

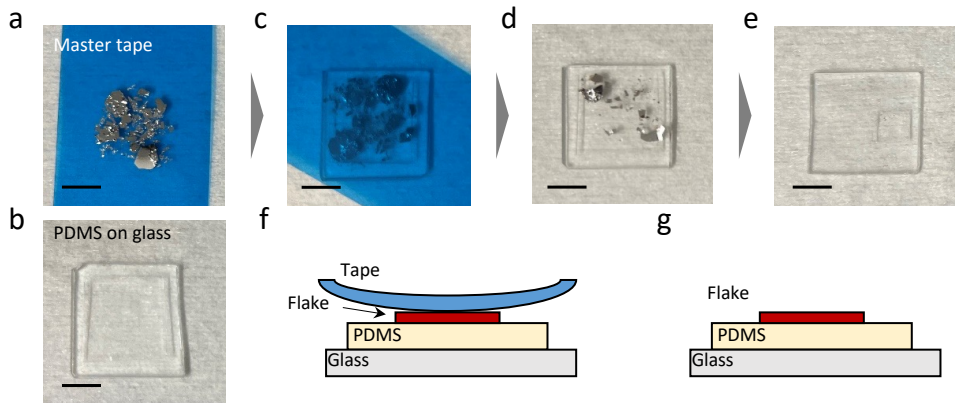

Figure 2.3. Mechanical exfoliation process. (a) A piece of master tape. (b) Substrate for TMD exfoliation: PDMS on glass. (c) Master tape is placed onto the substrate. The cross-section diagram is illustrated in (f). (d) Remove the master tape from the substrate. The cross-section diagram is illustrated in (g). (e) Final monolayer sample. Scale bar: 5 mm.

In order to employ the all-dry transfer method, we utilize a polydimethylsiloxane film (PDMS, PF-40/17-X4 from Gelpak) for monolayer TMD exfoliation. The double-sided film consists of three layers: polyester substrate, gel material and polyethylene coversheet. Despite the salesperson's state that the gel material and its properties are the same for both sides, we discover significant differences between them. As depicted in Fig. 2.2, the interface between gel material and polyethylene cover sheet (top surface) displays a cleaner surface with minor bubbles underneath, while the interface between gel material and polyester substrate (bottom surface) shows more visible dots. In addition, we find there is a slight difference in tack. The bottom surface is more adhesive, suggesting more free polymer chains and residue. Thus, we place the bottom surface onto a solid substrate and use the top surface to touch the TMD flakes on a master tape. The PDMS is cut to a size of 1 cm $\times$ 1 cm and gently placed onto a glass substrate (1.2 cm $\times$ 1.2 cm) (Fig 2.3(b)). Due to the softness of the PDMS, this process should be done slowly and gently to prevent any strain on PDMS and to ensure that there are no bubbles trapped between the PDMS film and the glass substrate.

To peel monolayer from blue tape (Fig 2.3(c)), the adhesion between PDMS and flakes should be larger than that of blue tape. The adhesion between PDMS and flakes is determined by the peeling speed owing to the viscoelastic behaviour of the PDMS [84]. By fast peeling off, the PDMS behaves as an elastic solid and attaches more flakes from blue tape. On the contrary, at a slow peeling speed, PDMS detaches and releases the flake to the adhere-preferential surface. This is also the working principle for the all-dry transfer method (see Section 2.2). As the adhesion is kinetically controllable, developing good hands-on skills for exfoliation requires practice.

After identifying a desirable monolayer in the sample (Fig 2.3(d)), a smaller piece

(3 mm × 3 mm) of the sample is cut (Fig 2.3(e)) and stored in a vacuum. A high-quality master tape typically yields good flakes and can be reused multiple times until the yield decreases. It is important to make a new master tape when the yield is low, as hunting for good flakes on a bad tape can be time-consuming and unproductive. The good master tape can be stored by covering with PDMS for future use, but long-time storage may increase residue on samples, possibly due to the adhesive bond between the tape and PDMS.

Monolayer identification

There are several methods to identify whether a TMD sample is a monolayer or not, including atomic force microscope (AFM), Raman spectroscopy, optical contrast of microscope image and photoluminescence. Among them, evaluating optical contrast is widely used, which turns out to be a fast, accurate and reliable method to identify the thickness of layered TMD materials. Before using optical contrast, calibration is necessary to correspond optical contrast to thickness. We then confirm the monolayer TMD thickness by its photoluminescence (the optical set-up will be discussed in Chapter 3). Once the calibration is done, the measurement conditions for the microscope, such as illumination intensity and exposure time are set for future use. Fig. 2.4(a) shows an optical microscope image of the WSe_2 on PDMS sample and the optical contrast for different layers is recognizable to the naked eye. Fig. 2.4(b) shows the PL of monolayer WSe_2 (blue line) centered at ∼750 nm and its intensity is five times stronger than the bilayer (red line), which is fully consistent with band-gap nature and previously reported references [85].

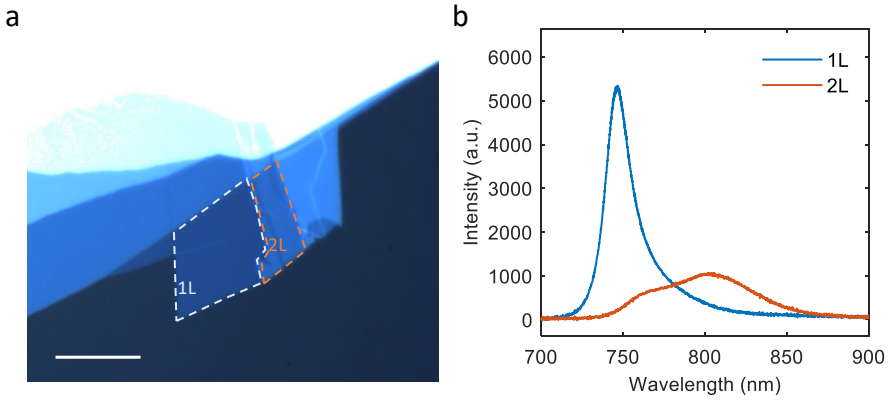

Figure 2.4. Monolayer WSe_2 identification. (a) Optical microscope image of WSe_2 on PDMS, showing different optical contrast for different layers. Scale bar: 10 µm. (b) PL spectra of monolayer and bilayer WSe_2.

hexagonal Boron Nitride (hBN)

A thin layer of bottom hBN is needed for transferring the heterobilayer onto the cavity. The thickness of the bottom-hBN should be thin to bring the heterobilayer closer to the cavity mode. For thin hBN flake exfoliation, oxidized silicon wafers are widely used to enhance contrast due to interference enhancement (Fig. 2.5(a)). We have not seen any reports using PDMS to peel hBN. We are still interested in knowing if it is possible to obtain thin enough layers using PDMS peeling. If so, we can use an all-dry transfer method for the ultimate device.

Since hBN cannot be identified by its thickness using PL due to its large band gap of ∼5 eV, we first fabricate hBN flakes on PDMS and transfer them onto a ∼90 nm SiO_2/Si substrate (The transfer method will be described in Section 1.2.1). We can calibrate the optical contrast by measuring the thickness using AFM performed by Hanlin Fang at Chalmers University of Technology.

The results are shown in Fig. 2.5, showing microscopy images of the same hBN flake on PDMS and SiO_2/Si substrate. The thinnest hBN material we were able to locate on PDMS corresponds to a thickness of 6 nm, which is sufficient for our project. However, the contrast of this hBN layer on PDMS is significantly low, as depicted in Fig. 2.5(b). It is important to note that this optical image is captured by a 100X objective. When searching for flakes, we typically use a 20X objective to make the process faster. At lower magnifications, the contrast is poorer as shown in Fig. 2.5(c) and is barely detectable. This can also be distinguished from the colour of bulk materials, as displayed in Fig. 2.1. In bulk form, TMD is completely opaque, while hBN remains transparent. Therefore, we use SiO_2/Si substrate for hBN exfoliation as it significantly improves the contrast.

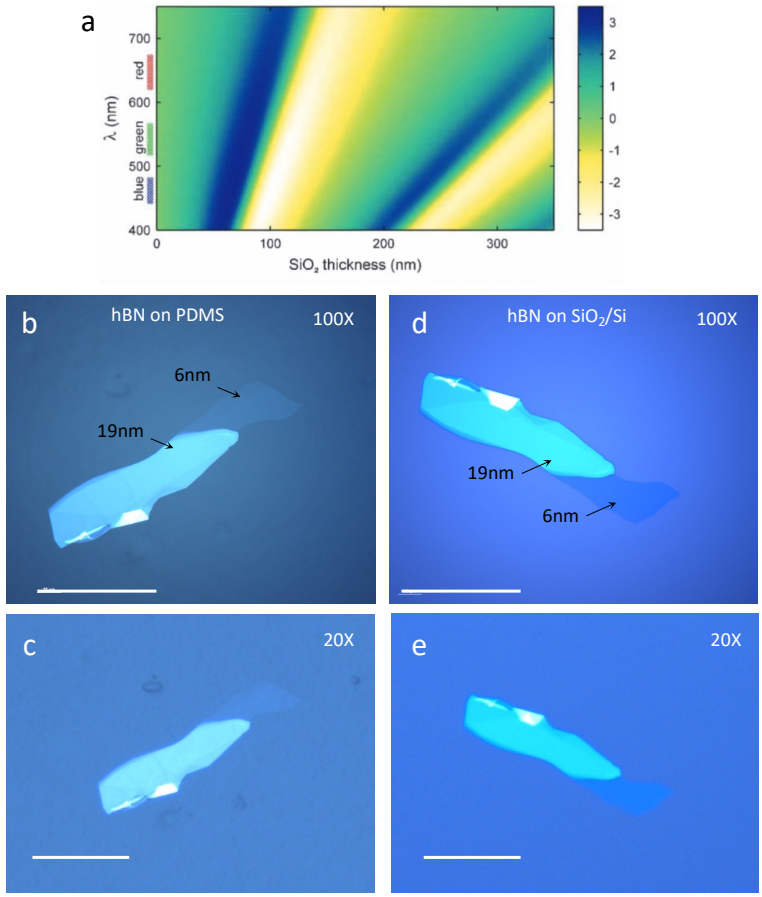

Figure 2.5. Optical contrast of hBN. (a) Color plot of the optical contrast of monolayer BN as a function of wavelength and SiO_2 thickness, taken from Ref. [86]. Optical microscope image of thin hBN flake on PDMS under 100X (b) and 20X (c) objective. Optical microscope image of the same hBN flake on 90 nm SiO_2/Si under 100X (d) and 20X (e) objective. Scale bar: 50 µm.

2.2 Home-built transfer setup and techniques

A clean interface is crucial to obtain a high-quality heterostructure on optical performance. Here, we use the all-dry viscoelastic stamping method [87] to assemble heterobilayers, and the fast pick-up transfer technique [88] to protect the heterobilayer by hBN and to place it onto photonic crystal cavities.

Both of these two methods require a transfer setup. Fig. 2.6(a-c) shows the images

of our homemade transfer setup, which is initially designed by our collaborator Hanlin Fang and optimized in use. It basically consists of a microscope imaging system (blue box), a stamp stage (green box)and a substrate stage (orange box). The working principle of the transfer setup is to lower the stamping stage until the stamp touches the substrate then leave the flake on the substrate, and use the microscope simultaneously to trace the process and deterministically place the flake to the position of interest. The specification of the transfer setup is shown in Table 2.1.

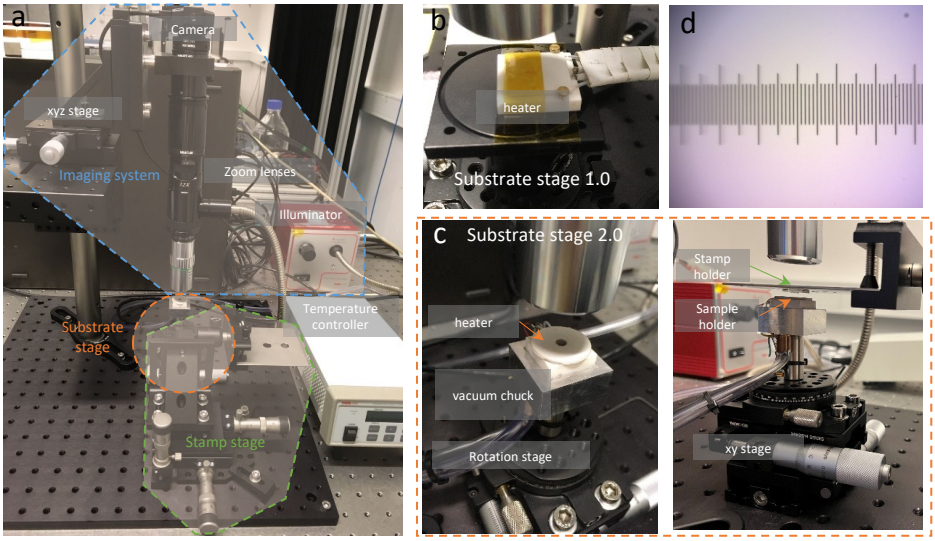

Figure 2.6. Homemade dry transfer setup for van der Waals heterostructure transfer. (a) Picture of the transfer setup. (b) First generation of the substrate stage. (c) Top view (left panel) and side view (right panel) of the second generation of the substrate stage with a vacuum chuck. (d) Micrometer image taken by the 7X microscope system, showing a 0.65 mm field of view.

For the microscope imaging system, an 20X objective with a working distance of 20 mm is used to allow enough space for stamp insertion. In the meantime, the long working distance corresponding to a small numerical aperture results in an inevitable blur image under large magnification. One major feature of our designed system is that we have a continuously adjustable magnification microscope system from 7X to 85X. Typically, a conventional microscope system requires multiple objective lenses to provide different magnification levels, which inevitably increases the cost of the transfer system. Our continuously adjustable microscope system can avoid switching objectives back and forth during the transfer process and always allow us to find a suitable magnification for different sizes of flakes. Apart from this, the translation stage for the imaging system compensates for the limited field of view, giving the possibility to observe the status of whole samples during transfer.

For the stamp stage, a customized steel plate with holes is connected to a precise xyz translation stage. The stamp will be mounted on the hole via double-sided polyimide tape, as shown in the right panel of Fig. 2.6(c).

The substrate stage is one of the key elements of the transfer setup and can be rotated 360° with a resolution of 0.477°, allowing the possibility of alignment of crystal flake when stacking heterobilayers. The twist angle between two monolayers strongly affects the properties of the bilayer and will be discussed in Chapter 4. In addition, the substrate can be heated up to 200 °C. Note that the 200 °C heating range here is limited by our heater controller (TC200 from Thorlabs). The maximum temperature of the heater is 400 °C. To hold a substrate, we initially use a double-side polyimide tape (Fig. 2.6(b)). The polyimide tape, also called Kapton tape, is heat resistant with a use temperature range from -75°C to 260 °C. However, the adhesion is too good to release the sample, which causes the risk of cracking fragile substrates like silicon and GaAs. After several uses, the fragments left on the tape cause adhesion vanishing and substrate skew. Therefore, we customize a new holder with a vacuum chuck (Fig. 2.6(c)), which perfectly solves this problem. In this case, we always need to remember to turn on the vacuum pump when transferring, as sudden separation breaks TMD flakes into small pieces.

Table 2.1. Specification of homemade transfer setup

	Specification
Microscope system	Objective 20X, W.D. 20 mm, N.A. 0.42 Magnification: 7X-85X continuously Field of View: 0.65-0.054 mm + 25 mm Sensor: 1/3 inch
Stamp stage	xyz travel range: 13 mm, 50 µm/rev, resolution: 0.5 µm
Substrate Stage	Maxium temperature: 200°C 360° of continuous rotation, resolution: 0.477°/rev xy travel range: 25 mm, resolution: 500 µm/rev

2.2.1 The all-dry viscoelastic stamping method

The generation of interlayer excitons is achieved through charge transfer between two adjacent monolayers. The cleanliness of the interface between the two layers plays a critical role in the efficiency of this process. In order to prepare high-quality heterobilayers, a clean and efficient method is required. Here, we employ the all-dry viscoelastic stamping method [87], which avoids any wet chemistry step and relies on viscoelastic stamps. The process of heterobilayer stacking is illustrated in Fig. 2.7. First, two exfoliated monolayer TMD flakes are mounted on the dry transfer sample and substrate stages, respectively (Fig. 2.7(a)). The monolayer areas are positioned via the imaging system and the substrate stage is rotated to control their twist angle, and then fix the angle. The sample stage is gradually lowered, and their

relative position is adjusted during the lowering process. When the two surfaces come close, interference fringes emerge, and a clear boundary between the contact and non-contact areas appears as shown in Fig. 2.7(b). Once the layers are in contact (Fig. 2.7(c)), wait for 5-10 minutes to ensure good contact between the monolayers, and do not move the relative xy position. The sample stage is raised back up to separate the two stamps (Fig. 2.7(d)). As the adhesion between PDMS and flakes is determined by the peeling speed, this process should be slow so that the van der Waals force between the heterobilayer is stronger than that between monolayers and PDMS. The resulting heterobilayer (Fig. 2.7(e)) can be either on the sample stage or substrate stage. Heating throughout the entire transfer process can typically increase the yield, usually at a temperature of 60 °C. The speed of the process can be controlled by gradually increasing the temperature by 1-5°C, allowing for a slow, continuous and controllable transfer.

Throughout the entire transfer process, the surface of the monolayer does not come into contact with any colloids or chemicals, and no high-temperature heating is required, to the best of my knowledge, making this the cleanest approach for preparing heterobilayer interfaces. Furthermore, the transfer process of this method is very simple and fast. During the exfoliation process, the TMD crystals tend to break preferentially along specific crystal axes, especially the zigzag edge (the middle and right panel of Fig. 2.7(a)). Thus, we can align these axes during the transfer process and identify the twist angle by examining the crystal axes after the transfer (right panel of Fig. 2.7(e)), providing the possibility for us to study the effects of twist angle systematically.

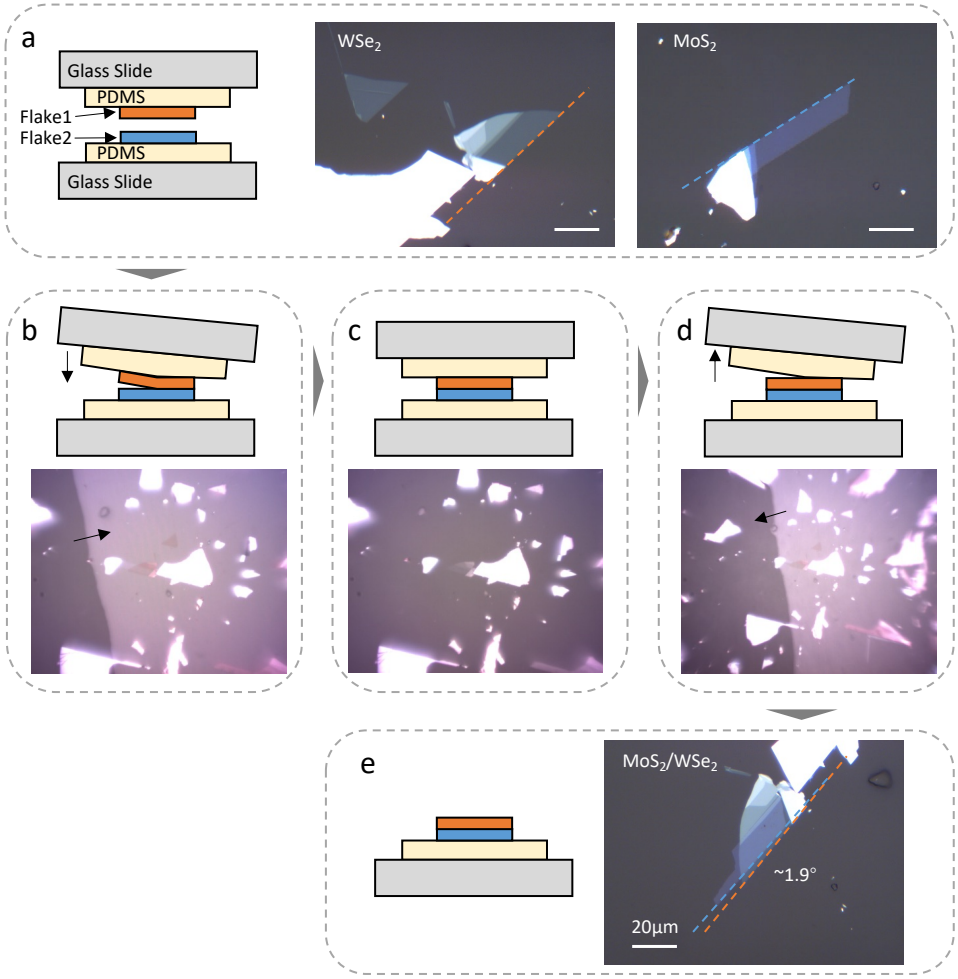

Figure 2.7. Step illustrations of van der Waals heterostructure assembly via all-dry viscoelastic stamping method. (a) TMD samples are mounted on the dry transfer stages and aligned at a desired angle. The middle and right panels show optical images of monolayer WSe_2 and MoS_2. The dashed lines highlight the crystal axes. The sample stage is gradually lowered (b) until the two layers are in full contact (c), after which it is raised back up (d). The experimental images during the process (b-d) are shown in the lower panel. (e) Obtained heterobilayer on PDMS substrate. The optical image is displayed in the right panel. Scale bar: 20 µm.

2.2.2 The fast pick up transfer method

After obtaining a high-quality heterobilayer, the subsequent step is to transfer it onto a photonic microcavity. The all-dry viscoelastic stamping method facilitates the transfer of flakes on stamps onto substrates with a strong affinity to the flakes, such as gold and SiO_2/Si. Nevertheless, this technique is not suitable for substrates with a small effective area, including pillars, gratings, and nanobeam cavities. Furthermore, it is challenging to pick up hBN on SiO_2/Si substrates using this method. However, the fast pick-up technique [88] can effectively resolve this issue.

The principle behind this technique is to take advantage of the strong van der Waals force between polycarbonate (PC) film and 2D flake, enabling pickup flake from substrates like SiO_2/Si. The polymer is then melted by heating it to 180°C, higher than the glass transition temperature. Using this method, the material can be transferred to almost all substrates, even those with weaker adhesion to the material than polymer.

This PC-mediated transfer process involves high-temperature heating and the use of chemical reagents. To maintain the high quality of the heterobilayer, we encapsulate it between two hBN flakes. The presence of hBN serves to shield the heterobilayer from oxidation during high-temperature heating and prevents contamination from polymers and chemicals. Moreover, hBN provides a uniform dielectric environment that reduces excitonic linewidths [89] and protects against further oxidation caused by time, beam damage, and increased heat dissipation.

In this section, we will discuss the preparation of the PC stamp and explain the pick-up and drop-down process to making an hBN/MoS_2/WSe_2/hBN heterostructure on a cavity. Moreover, we will discuss the use of a dome-shaped stamp instead of a flat stamp to improve the transfer process further.

Preparation of the PC stamp

The stamp for this method is a thin PC film placed on top of PMDS on glass. The schematic cross-section is displayed in the top half of Fig. 2.8(a). To prepare a thin PC film, we first dissolve the polycarbonate particles (CAS Number: 25037-45-0 from SigmaAldrich) in chloroform to form a PC solution with a concentration of 6%. Then we ultrasound it until the particles are fully dissolved. Next, we drop this solution onto a glass slide and immediately cover it with another slide. As soon as the solution spreads out, we rapidly slide the two slides. As the chloroform quickly evaporates into gas, we obtain uniform PC film on glass slides after a few seconds. It is important to note that the procedure should be carried out in a fume hood to ensure safety.

Although HQ Graphene company sells pre-made PC solutions, they are sold in small quantities and are quite expensive, with a price of around 570 euro for just 30 ml. Consequently, we have decided to prepare the solution ourselves, using the polycarbonate obtained from SigmaAldrich at a cost of 210 euro for 250 g. This amount is sufficient to prepare around 4 liters of solution!

We place a PDMS onto a flat glass substrate and use a scalpel to cut it into a small piece with a size of 4 mm. Then, we attach four pieces of Scotch tape to the edges of a PC film, forming a square aperture at the center that is larger than the PDMS. Press the tape to increase adhesion. Detach the PC film from the glass slide so that a thin film of PC is suspended across the hole in the scotch tape. and lay it across the PDMS. Note the PC aperture must be larger than the PDMS stamp to prevent the melting of Scotch tape during high temperature, which leaves a residue that is difficult to remove. One can heat the stamp to 90°C before use to evacuate any trapped air between the PC and PDMS layers. Once the PC stamp is prepared, it can be mounted to the stamp stage. It is then ready for picking up flakes.

Pick-up and drop-down process

The process of the fast pick-up transfer method is similar to the all-dry viscoelastic stamping method, with the main difference lying in temperature control. Fig. 2.8 depicts the schematic of the PC transfer process, mainly involving two steps: pickup and dropdown.

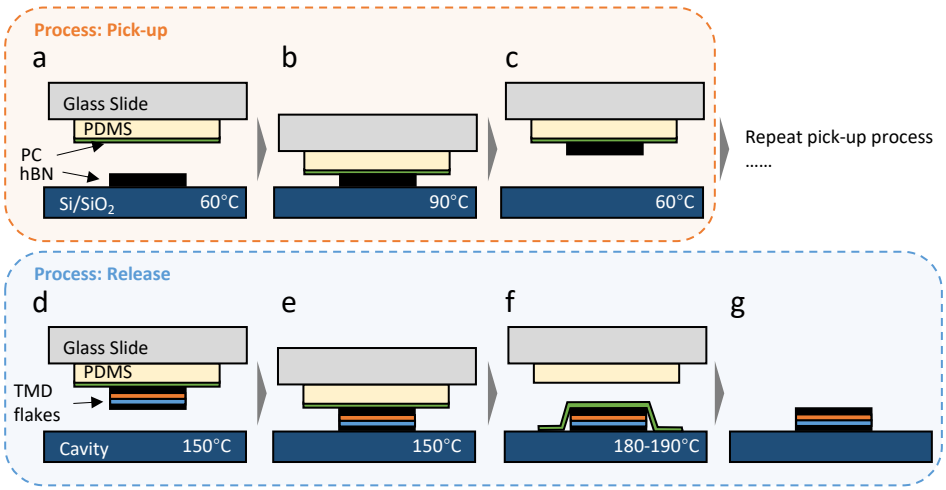

Figure 2.8. Schematic of the PC transfer process, consisting of pickup (a-c) and dropdown (d-g) steps.

Similar experimental phenomena as in Section 2.2.1 are observed with the emergence of interference fringes and a clear boundary between the contacted and non-contacted regions. To pick up the first flake, top-hBN in our case, the top-hBN/SiO_2/Si substrate is pre-heated to 60°C. When it comes into contact with PC film, the temperature is increased to 90°C and we wait for 5 minutes. Then the temperature is cooled

down to 60°C and the bottom hBN is lift by the PC film. This process is then repeated to collect the heterobilayer and bottom-hBN materials. Then heterostructure of bottom-hBN/heterobilayer/top-hBN on the PC stamp is obtained, as illustrated in the cross-section schematic shown in the top half of Fig. 2.8(d).

Once the pickup process has been completed, the heterostructure is ready to be positioned onto a desired cavity. Preheat the cavity to 150°C and after the heterostruture is brought into contact with the cavity, the temperature is increased gradually to 180-190°C. The temperature is kept high for 10 minutes to melt the PC film, after which the sample holder can be slowly lifted. Finally, the PC is removed by rinsing in chloroform for 1 minute and then in IPA solution (Isopropyl Alcohol). In this way, we can successfully transfer hBN/MoS_2/WSe_2/hBN on the desired cavity.

Dome stamp

When using flat stamps, several issues arise. Firstly, there is relative motion between the stamp and substrate as the contact area increases. In addition, the contact area is large around 4 mm, which is the same size as the PDMS stamp. The surrounding structures are covered with unexpected flakes, rendering them unusable for further experiments. The dome stamp offers a highly effective solution to these issues, with its innovative use first reported in the tear-and-stack technique of 2014 [90]. Upon pressing the stamp onto the substrate, the resulting contact area takes on a circular shape and expands outward radially. By controlling the size of the contact area, the dome stamp can achieve a smaller contact area compared to flat stamps, while also enabling precise control over the applied pressing force, thereby ensuring a reliable and repeatable outcome.

The dome stamp is prepared at Chalmers University of Technology. The liquid PDMS (SYLGARD 184) is made by thoroughly mixing the silicone elastomer base with the curing agent. A droplet of the liquid is then carefully pipetted onto a flat PDMS film, where the surface tension of the liquid causes it to naturally form a hemisphere shape. The dome stamps are cured for 1 day. And the rest of the PMDS film is cut off, resulting in the semi-sphere PDMS stamp (Fig. 2.9(a)).

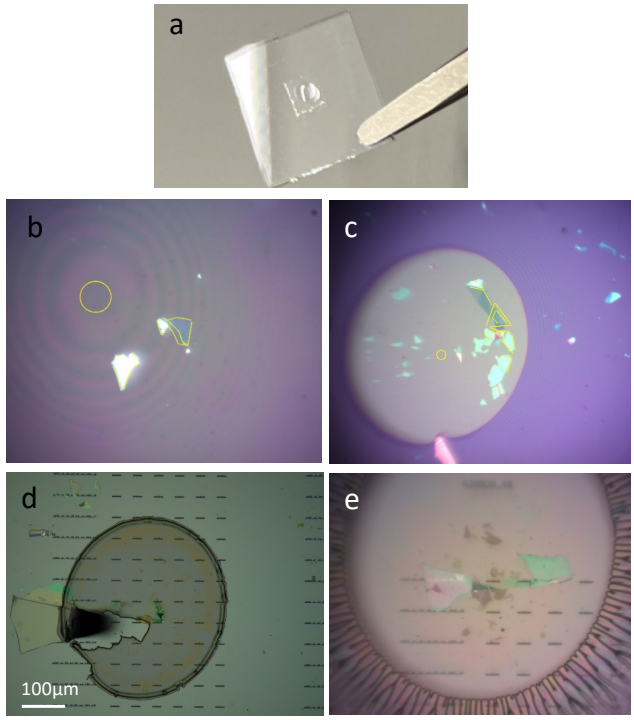

Figure 2.9. PC transfer with the dome stamp. (a) Image of a semi-sphere PDMS stamp on glass. (b) Newton's rings when the top and bottom layer comes close. (c) Picking up flakes. (d) Released flakes on the cavity. (e) Dendritic pattern due to insufficient heating temperature.

The transfer process for the dome stamp is similar to that of a flat stamp, but with a few notable differences. The dome stamp acts as an optical lens that improves image quality in the center, while blurring the surrounding area. Upon contact, Newton's rings are observed (Fig. 2.9(b)).

During the pickup process, it is advisable to maintain as small a contact area as possible, as this will lead to fewer flakes being picked up and a cleaner PC film. It is possible to achieve this by lifting the PC slightly during the heating process, which prevents the contact area from expanding any further. However, as our translation stage is manually controlled, it tends to produce shaking when hands touch the micromanipulator. For instance, when lowering the dome stamp to make contact with the substrate surface, it may retract back to an uncontacted state upon the release of hands. That brings challenges in controlling the speed of the process, especially when positioning desired flakes precisely at the center of the dome. Rapid detachment may result in flake breakage before reliable contact can be established. To mitigate this issue, we place the flake at a distance from the center (Fig. 2.9(c)) and

regulate the process through temperature control. In the future, an upgrade to an electrically-controlled translation stage may be considered.

In contrast to the large contact area of approximately 4 mm observed with flat stamps, the image in Fig. 2.9(d) shows a much smaller contact radius of around 100 µm after melting the PC using the dome stamp.

A potential issue that may arise during the experiment is illustrated in Fig. 2.9(e). If the releasing temperature is not high enough, it can result in the formation of a dendritic pattern.

With this technique, we successfully achieve to achieve hBN/MoS_2/WSe_2/hBN on a desired cavity, as shown in Fig. 2.10(a). Due to the low optical contrast of hBN on Si, we utilize a 585 nm bandpass filter with a bandwidth of 36 nm (#33-907 from Edmund) to enhance the contrast. The resulting images (Fig. 2.10(b)) show several flakes observed on top of the cavity, indicating the successful transfer of the heterostructure.

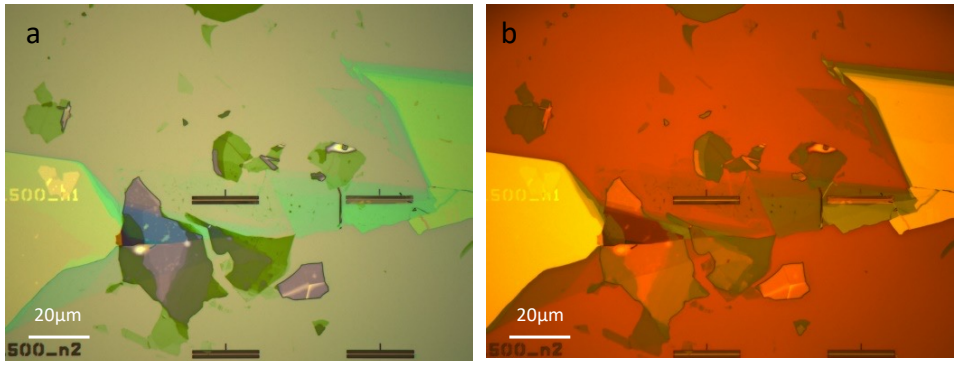

Figure 2.10. Microscope images of hBN/MoS_2/WSe_2/hBN heterostructures on the cavity without (a) and with (b) a bandpass filter.

2.3 Fabrication of photonic crystal cavities

The objective of this section is to describe the fabrication of a silicon microcavity with a high-Q factor. The cavity design we employed is a topological nanobeam cavity. More detail will be described in Chapter 5. To achieve this experimentally, it is necessary to obtain precise dimensions in the fabricated structure that match the design specifications as closely as possible. Additionally, it is important to minimize surface roughness, which can cause scattering losses and diminish the Q factor.

To accomplish this goal, we have tested different etching recipes to determine the sidewall roughness and verticality, as well as any resulting structural size deviations. Then we compensate for any pattern deviations through the use of layout design.

Sidewall test

To observe the sidewalls, it is necessary to cut the sample and observe the cross-section after etching. The substrate used for the test sample is a Si wafer for the following reasons: 1) Si wafers are thinner and easier to cleave into smaller pieces compared to SOI wafers (Silicon on Insulator), which is the formal substrate for cavities; 2) they can be used to test etching depths; 3) Si wafers are cheaper than SOI wafers.

The perpendicularity and roughness of the sidewalls are closely related to the etching technology. There are two facilities in DTU Nanolab that can be used to etch silicon: ASE and DRIE-Pegasus. We conducted etching experiments on samples using both machines, and the results are shown in Fig. 2.11. We found that the samples etched by ASE had much better sidewalls than those etched by DRIE. The holes etched by DRIE showed a droplet-shaped pattern, with a narrower upper part and a wider lower part, and got numerous particles on the inner wall. This may be due to the instability of the DRIE instrument at the time. On the other hand, the sidewalls etched by ASE were smooth and had better perpendicularity. Therefore, we use ASE to conduct the following etching tests.

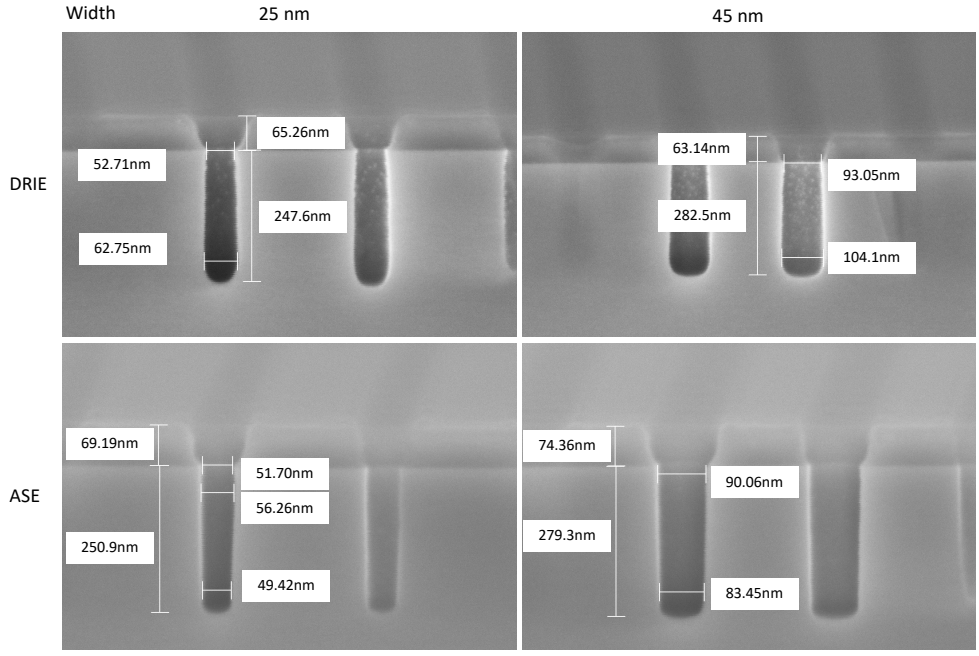

Figure 2.11. Sidewall test comparison of ASE and DRIE. Top(bottom) row: SEM images under DRIE(ASE) etching processes.

Etching deviation test

In addition to sidewall perpendicularity and roughness, we also need to test whether the existing fabrication process can achieve the critical dimensions we need, i.e., whether the dimensions are deep and narrow enough. We conducted tests on a series of structures with different sizes and etching times.

The etching depth strongly depends on the etching time. The etching time must be long enough to ensure complete etching. When the Si layer on the SOI substrate is etched through, plasma bombardment occurs on the SiO_2 layer and reflects onto the sidewall. Overetching may cause problems such as oversize dimensions, inadequate resist mask thickness, and compromised sidewall perpendicularity. The cross-sections of holes under the same etching time are displayed in Fig. 2.12, showing the etching depth depends on the size and shape of the hole. We determined the appropriate etching time under the condition of ensuring that the smallest hole we need could be etched through.

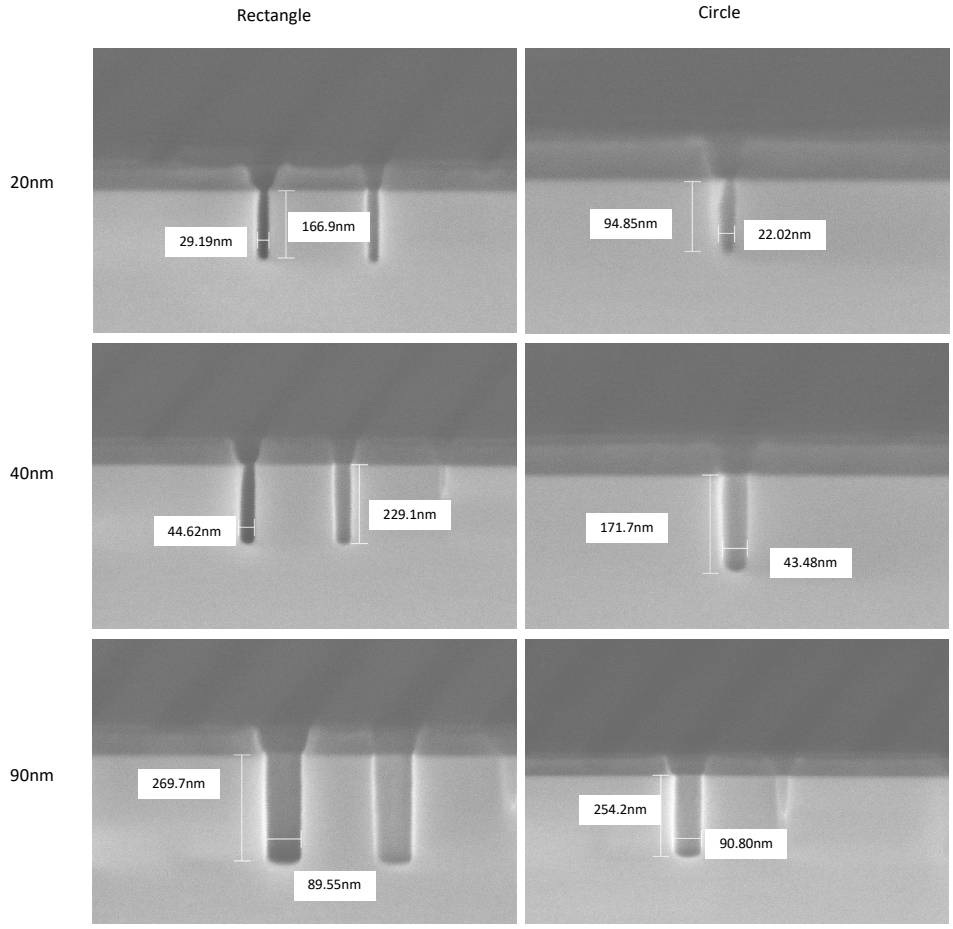

Figure 2.12. Cross section SEM images of a test sample under 12 cycles of dry etching. Left column: rectangular mask with a 140 nm length and different width. Right column: circular mask with different diameters.

Since the actual cavity is composed of holes of various sizes, and their etching time is the same, there are varying degrees of deviation between the designed size and the final prepared size. Therefore, we get the deviation from the actual prepared size and made corrections to the layout accordingly.

Cavity fabrication

Once testing conditions are determined, we are ready to fabricate our formal sample. The complete fabrication process flow is illustrated in Fig. 2.13, including six steps: substrate cleaning, resist spin coating, electron beam writing, development, etching,

and resist stripping. We do not hollow out our cavity, as this can compromise its structural stability, which is essential for transferring to heterogeneous structures in the future.

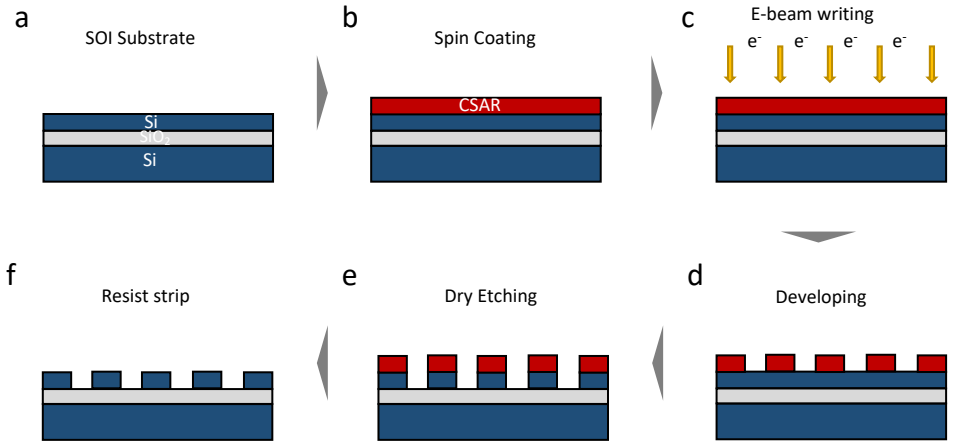

Figure 2.13. Schematic of nanofabrication process for silicon cavity. (a) SOI substrate cleanning. (b) Resist spin coating. (c) Electron beam writing. (d) Development. (e) Dry etching. (f) Resist stripping.

We use a 220 nm SOI wafer with a structure comprising a 220 nm top layer of silicon and a 2 µm SiO_2 layer separating it from the handle silicon layer. The standard EBL positive resist CSAR (AR-P 6200.09 from AllResist) is coated on the pre-cleaned chip with a thickness of 180 nm. After e-beam exposure, the sample is developed with AR 600-546. After dry etching, resist are dissolved in 1165 solution. More fabrication parameters details are described in Table.2.2

As two pieces of equipment are only capable of handling wafers, spin coater and ASE dry etching machine, we bond our SOI chips to 4" carriers using Crystalbond, wax with a flow point of approximately 65°C. Bonding and debonding are achieved using a hotplate, and residue from the Crystalbond can be removed by acetone, IPA and DI water.

The results are depicted in Fig. 2.14, exhibiting a clean surface and sidewall with matching dimensions to our design. In addition, our optical measurements (discussed in Chapter 5) observed a high-Q cavity mode, affirming the successful implementation of the fabrication process.

Table 2.2. Fabrication recipe for Si cavity

Step and tool	Parameters
Substrate	220 nm SOI (2 µm BOX)
Substrate cleaning:	Ultrasonic immersion in 1165 for 30 min IPA for 5 min
Spin coating: Spin Coater: Gamma e-beam & UV	180 nm CSAR (AR-P 6200.09 from AllResist) 4318-DCH 100mm CSAR 180nm spun at a speed of 4500rpm soft bake at 180°C for 3min
E-beam writing: JEOL JBX-9500FSZ	Dose: 320 µC/cm^2 Current: 0.8 nA
Development: Developer: E-beam	immersion in AR 600-546 for 60s IPA for 60s N_2 blow-dry
Dry etching: ASE	12 cycle of the Bosch process: Etch: 5 seconds C_4F_8 50 Sccm + SF_6 50 Sccm, Coil: 500W, Platen: 30W Passivation: 3 seconds C_4F_8 50 Sccm, Coil: 400W, Platen 0W
Resist strip:	Ultrasonic immersion in 1165 at 60°C for 2 hours.

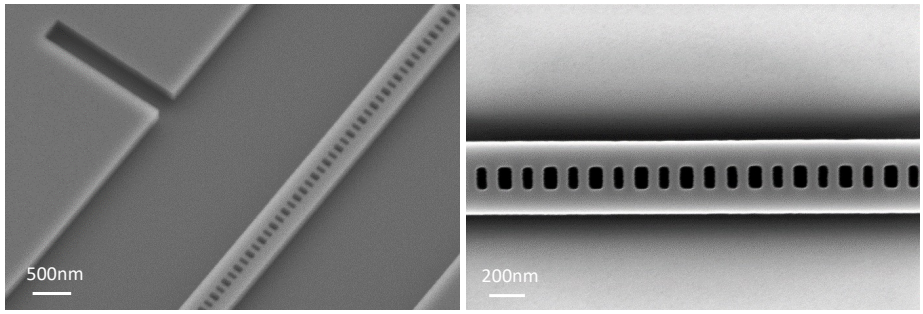

Figure 2.14. SEM images of cavity, taken by Xingyu Huang.

CHAPTER 3

Building an optical characterization setup

After preparing the samples, we characterized them using optical methods. To characterize the optical properties of intralayer excitons and interlayer excitons, we constructed a multifunctional optical testing platform with a working wavelength ranging from visible to near-infrared. Starting from an old Andor SR500i spectrometer, which was not used for many years, we invested significant efforts in building this optical setup from scratch and also troubleshooting issues with the old spectrometer.

This chapter is divided into two main parts. The first section provides an overview of our home-built optical setup and the challenges we faced during its construction. Specifically, we discuss the difficulties we encountered while debugging the old spectrometer, which is the most crucial equipment in the platform. We also explain how we overcame the challenges related to the near-infrared linear array detector and optimized the grating to achieve optimal performance.

In the second section, we describe the specific measurement techniques we used with this home-built setup to characterize our samples, including

- Micro-photoluminescence spectroscopy (μ-PL),
- Differential reflectance spectroscopy (DRS),
- Time-correlated single photon counting (TCSPC),
- Polarization-resolved second harmonic generation (SHG).

We also explain how we gather and process the raw data.

Overall, we believe that this chapter provides readers with a comprehensive understanding of our experimental setup and the techniques we used to characterize the samples.

3.1 Home-built optical characterization setup

Fig. 3.1 shows the images of our home-built optical setup. Here we use the cage system to construct the setup, which uses four rigid steel rods and optics are mounted along

a common optical axis, as it provides robust stability and accurate alignment.

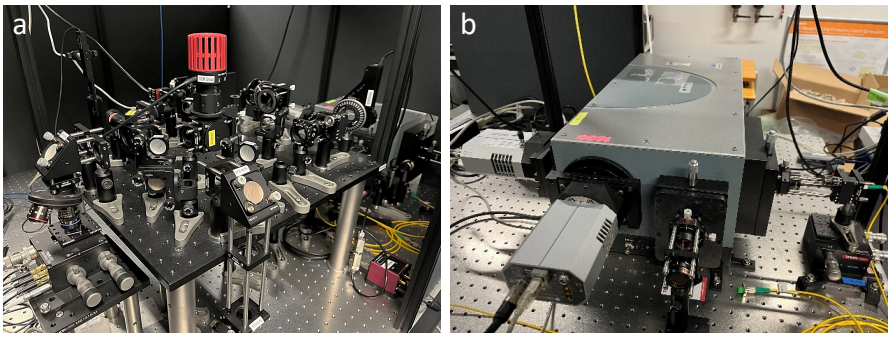

Figure 3.1. The home-built optical setup for optical experiments on TMDs. (a) Image of the setup. (b) Image of the spectrometer SR500i with dual input and output ports.

Optical components

For supporting a wide spectral range from visible to near-infrared, the optical components selected for the multifunctional setup, including a collimator (protected silver reflective collimator, operation wavelength: 450 nm - 20 µm), mirrors (protected silver mirror, 450 nm - 20 µm)), beam splitters (UVFS substrate, 600 nm - 1700 nm), and objectives (LCPLN50XIR from Olympus, 400 nm - 1300 nm), are chosen to be as broadband as possible. The multifunctionality inevitably results in some compromise in efficiency. For example, the use of a dichroic mirror could double the PL collection efficiency compared to a fifty-fifty beam splitter, but it cannot be used for DRS and SHG measurements.

Microscope system

The dimensions of the heterobilayers and cavities are on the order of tens micrometers of magnitudes. In order to locate the sample and precisely identify the location where the excitation laser is aimed, a microscope imaging system is required. Fig. 3.2(a) shows the schematic of the reflective imaging system, where the sample is illuminated by a light-emitting diode (LED), and the reflected signal is collected by a 50x near-infrared objective lens (LCPLN50XIR from Olympus) and focused onto the camera (DCC1645C from Thorlabs). Fig. 3.2(b) displays a image of the heterobilayer sample, showing the clear boundary of the heterobilayer and good optical contrast for monolayer and bilayer TMD. By calibrating the system with a stage micrometer, our microscope provides a 56x magnification, with a sufficiently large field of view of 65.5 µm × 82.0 µm. With a camera pixel size of 3.6 µm, corresponding to 64 nm, the system's resolution is high enough to enable imaging of the focused laser spot.

Additionally, we have equipped the system with a microscope objective lens turret (OT1 from Thorlabs) and low-magnification objectives (5x and 10x), which help with rapid sample location and positioning.

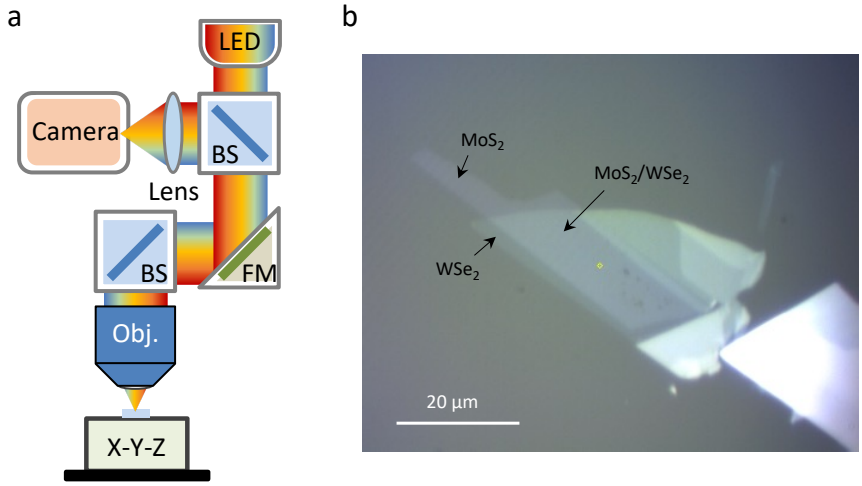

Figure 3.2. Imaging system. (a) Schematic of the imaging part of the setup. BS: beam splitter, FM: flip mirror, Obj.: Objective. (b) Image of a MoS_2/WSe_2 heterobilayer on PDMS taken under the imaging system.

Spectrometer system

In our optical setup, the most critical component is the spectrometer with an internal structure shown in Fig. 3.3(a). It separates light of different wavelengths in space using a diffraction grating and finally focuses it onto different positions on the detector to obtain the spectral signal. The spectrometer (SR500i from Andor) was provided by our collaborator Kresten Yvind and equipped with a silicon array camera (DU440A-BU) and InGaAs line camera (DU491A-1,7).

Upon initial use, we found that the efficiency of the spectrometer is low, making it impossible to measure the IX signal. During the process of debugging the spectrometer, we encountered difficulties in adjusting the beam spot to the center due to the inadequate threaded knob of the tilt adjustment screws. An additional challenge was the adjustment of the near-infrared detection path owing to the line array of the InGaAs camera. The InGaAs camera is a linear CCD with 1024 pixels in the x-direction and only one pixel in the y-direction with a width of 500 µm. In contrast, the Si camera is an area CCD with 2048 x 512 pixels, and the y-dimension can reach up to 6.9 mm in size. However, the spectrometer initially had only one output port with a flange that could be connected to a camera. An additional output port with an

array camera would be beneficial for the adjustment as well as the measurement of the intralayer exciton. Thus, we decide to send the instrument back to the manufacturer.

To improve the efficiency, we procured a new turret equipped with three new diffraction gratings. The parameters of gratings are listed in Table.3.1. Compared to the old gratings, these new gratings are designed to achieve optimal diffraction efficiency (blaze wavelength) close to the wavelength of our interest with protected silver coating to maximize efficiency in the NIR region.

Table 3.1. Specification of gratings of the old and new turret for the spectrometer.

The old turret	**The new turret**
Grating 1: 300 l/mm Blaze: 500 nm	Grating 1: 150 l/mm Blaze: 800 nm SIL
Grating 2: 600 l/mm Blaze: 1900 nm	Grating 2: 600 l/mm Blaze: 1200 nm SIL
Grating 3: 1200 l/mm Blaze: 500 nm	Grating 3: 1200 l/mm Blaze: 1000 nm SIL

After upgrading the spectrometer, we performed adjustments and calibration of the diffraction gratings. A top view of the new turret is displayed in the bottom panel of Fig. 3.3(b), showing two pairs of push-pull screws for each grating, referred to as the tilt and roll adjustment screws. These adjustment screws rotate the grating in different planes and result in diffracted light variation. As illustrated in Fig. 3.3(c), the roll adjustment screws change the rotation angle of diffracted light and the tilt shifts the position. Our old turret (see the top panel of Fig. 3.3(b)) cannot reach the tilt screws with a cover lid, making the adjustments much more inconvenient. When the diffracted light hits the edge of the InGaAs line detector, a comb feature with intensity decreasing appears, like the red and blue curve in Fig. 3.3(d). The yellow curve shows a well-aligned spectrum.

The adjustment process for the roll and tilt screws is a time-consuming one, as even a slight tilt change of 0.03° can lead to a significant image shift of 10 × 26 µm pixels on the sensor [91]. Additionally, these screws are push-pull screws, which means that tightening one screw requires the loosening of the other. Therefore, it is crucial to proceed with caution and patience during the adjustment process, especially when approaching the final stages. For the Si array camera we used, it takes at least 13 seconds to capture a complete image. To shorten the acquisition time, we can read only a few rows of the image in the readout area when the beam spot moves within a small range.

The adjustment process is as follows:

1. Set the grating to zero order to serve as a mirror, adjust the height of the monochromatic incident light until a signal can be detected by the InGaAs line scan camera, then rotate the flip mirror to switch to the Si array camera to correspond to the height of the line scan.

2. Adjust the tilt adjustment screws on the turret to make the beam spot at the same horizontal line when rotating the grating to 0th, 1st, and 2nd orders.

3. Adjust the roll adjustment screws on the turret to align the beam spot with the height of the InGaAs line camera.

4. Repeat steps 1-3 for the remaining two gratings to ensure that the three gratings on a turret produce images at the same heights. Make sure all the screws are tightened.

Finally, we performed the calibration by setting the grating offset utility in the Shamrock control panel, and the spectrometer is now ready for use.

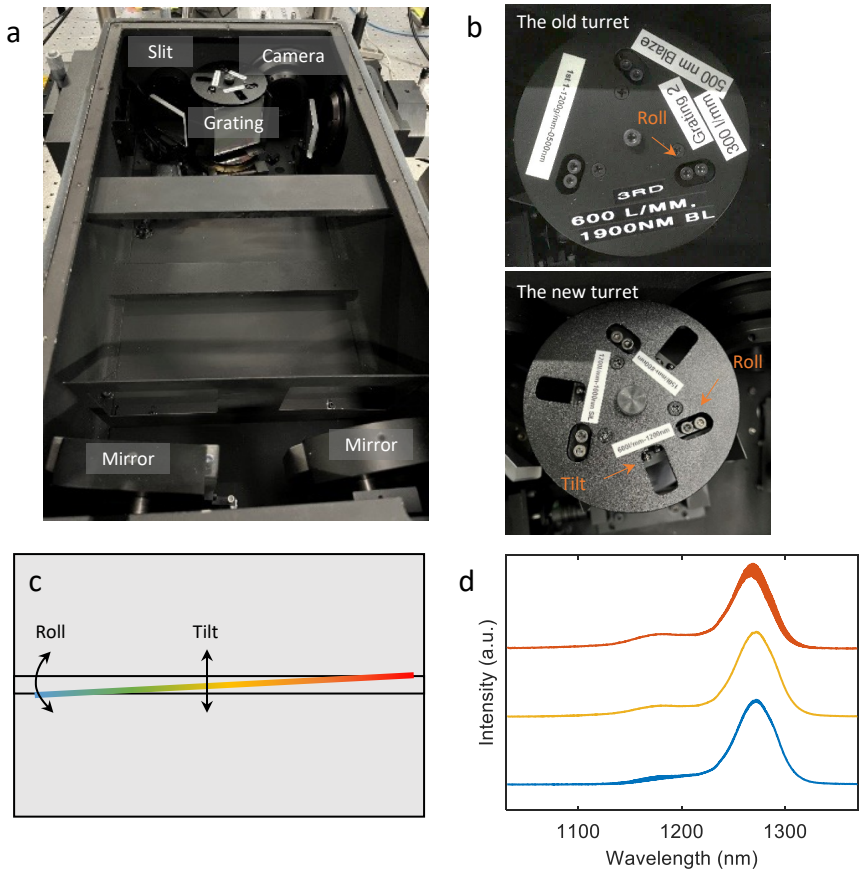

Figure 3.3. Problem-shooting of the spectrometer. (a) Internal structure of the spectrometer, consisting of entrance slits, a pair of mirrors, diffraction gratings, and a detector. (b) Top view comparison of old and new turrets. The top panel shows the old turret while the bottom panel shows the new turret. (c) A schematic of diffracted light hitting a 2D/1D detector. A light beam is split by the diffraction grating, depicted as a colorful straight line. The angle and position of the line can be adjusted by the tilt and roll adjustment screws. (d) PL spectra for light hitting different positions of the line detector. The yellow curve shows a typical smooth spectrum from InAs/GaAs QDs. The red and blue curves show the spectra when the light is not parallel to the line detector and partially hits the edge of the InGaAs line detector.

3.2 Optical techniques with our setup

3.2.1 Micro-photoluminescence spectroscopy (μ-PL)

The photoluminescence (PL) process involves the absorption of high-energy photons that excite electrons from the valence band (VB) to the conduction band (CB). Through rapid relaxation process, the electrons transit to lower energy states and bind with holes to form excitons. Recombination can occur through both radiative and nonradiative processes. Thus, only the radiative recombination process can emit photons that are detectable by the camera.

The schematic of the μ-PL setup is displayed in Fig. 3.4(a). A 637-nm laser source is utilized with emission energy above the band gap of TMD samples. As mentioned above, the excitonic effects will dominate the light emission properties of the TMD samples. A small laser spot size ($\sim$ 1 μm) is realized by the use of a high numerical aperture objective (NA=0.65), enabling us to detect local PL emission features in the samples. The emitted photons are collected and sent to the spectrometer and analyzed by their emission energies and linewidths.

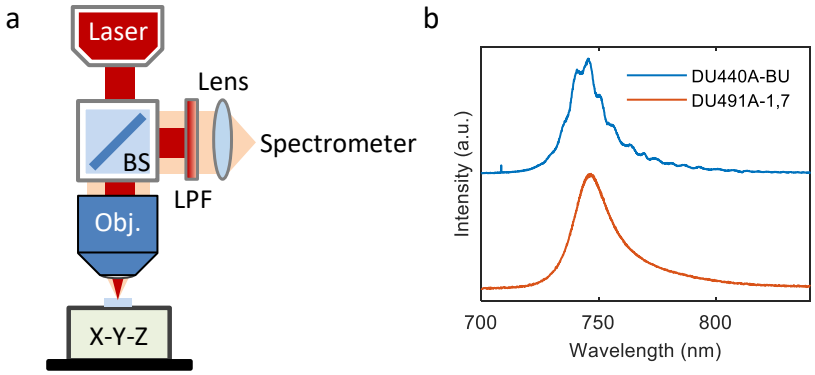

Figure 3.4. (a) A schematic of the PL setup. LPF: long-pass filter. The focal length of the lens in front of the spectrometer is 50 mm. (b) PL spectra of the monolayer WSe_2 detected by the Si line camera (DU440A-BU) and the InGaAs array camera (DU491A-1,7).

Fig. 3.4(b) shows the PL spectra of the monolayer WSe_2 detected by the Si array camera (DU440A-BU) and the InGaAs line camera (DU491A-1,7), respectively. We discovered that the back-illuminated Si array camera, which has an anti-reflective coating optimized for ultraviolet (UV) performance, exhibits interference fringes in the spectrum for wavelengths above 700 nm (blue curve in Fig. 3.4(b)). This characteristic makes it unsuitable for studying intralayer exciton.

However, the InGaAs line camera is capable of detecting signals in a range spanning from 600 nm to 1700 nm. Although the quantum efficiency of the InGaAs

camera at visible wavelengths is relatively low (e.g., 15% at 700 nm) compared to NIR wavelengths (e.g., 85% at 1200 nm), the strong luminescence of the intralayer exciton enables us to acquire its spectra (red curve in Fig. 3.4(b)). Figure 3.5 displays the PL spectra from different samples, showing a wide operation wavelength range from 700 nm to 1600 nm.

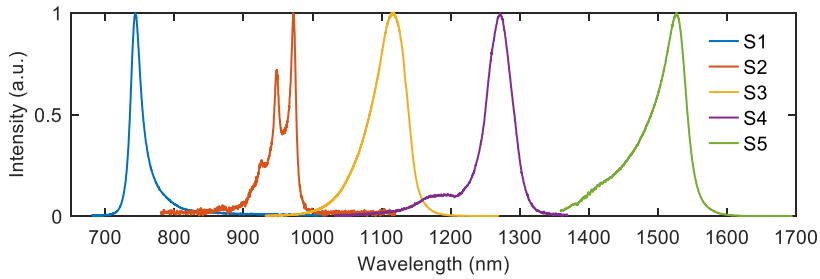

Figure 3.5. PL spectrum range of the optical setup using the InGaAs line camera. The samples (S1-5) shown here are monolayer WSe_2, InGaAs QW, InGaAs QDs, InAs/GaAs QDs, and InP QWs, respectively.

In addition, our setup is capable of weak signal detection. For example, we can measure the PL from monocrystalline silicon, which has relatively low luminescence efficiency due to its indirect bandgap nature. The raw data of the Si PL spectrum is depicted in the red curve in Fig. 3.6(a), showing a PL intensity of 1000 counts per second under 2680 µW excitation power. Since the signal is weak, the influence of background noise must be considered. This background noise may come from the read noise and thermal noise from the camera as well as unexpected noise from the dark experiment lab. The background is a spectrum taken under the same acquisition condition without excitation (blue curve in Fig. 3.6(a)) of the camera.

Therefore, we subtract the background and obtain a pure PL spectrum (see Fig. 3.6(b)). The cut-off at 1000 nm comes from a long-pass filter. [1]

For samples with strong PL, whether or not to subtract the background has little effect. For a better illustration, the PL spectra from the GaAs QDs sample are displayed in Fig. 3.6(c-d), showing a strong PL intensity at above 20000 counts per second under 6.7 µW excitation power. Since the signals from our heterobilayer samples are usually weak, the background has been subtracted from all the data in this thesis.

[1] A strong excitation laser at a short wavelength of 637 nm is used to pump the sample. A single long-pass filter is not sufficient to filter out the laser, resulting in the detection of the second-order diffraction light by the sensitive detector, i.e., a sharp peak at 1274 nm. Thus we add another long-pass filter to block the laser completely.

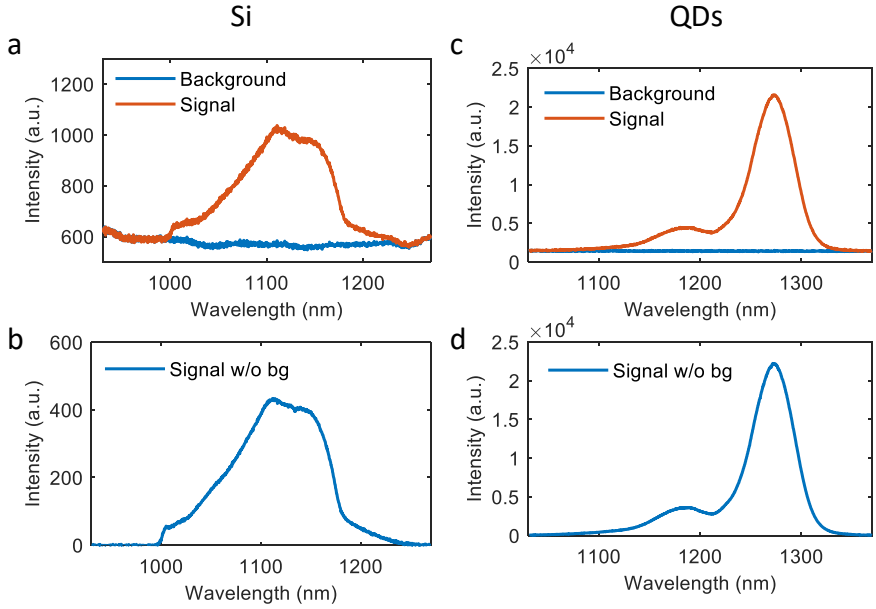

Figure 3.6. Weak signal detection. (a) Raw PL spectrum (red) from silicon by using an SOI substrate with an excitation power of 2680 µW, and background noise (blue). (b) Pure PL spectrum after subtracting the background. The cut-off at 1000 nm comes from a long-pass filter. (c) Raw PL spectrum (red) from GaAs quantum dots at 6.7 µW excitation power, and background noise (blue). (d) Pure PL spectrum after subtracting the background.

Scanning the sample and recording PL at each point results in a three-dimensional hyperspectral data set, and this type of measurement is known as PL mapping. The spatial distribution of optical properties provides more information about the homogeneity of the sample, as will be seen in Section 4.1.

3.2.2 Differential reflectance spectroscopy (DRS)

In TMD monolayers, the dominating oscillators are exciton resonances. Differential reflectance spectroscopy (DRS) is regarded as the way to measure of absorption spectra [92, 93], thereby providing valuable information on exciton optical transitions in TMDs.

DRS involves measuring the reflectivity of a non-absorbent substrate without (R_0) and with (R) an absorbent thin film on the top, respectively. It indicates the reflectivity change introduced by the presence of thin film and is defined as

$$\frac{\triangle R}{R_0} = \frac{(R - R_0)}{R_0} \tag{3.1}$$

Strictly speaking, measuring absorption (A) requires the measurement of both transmittance (T) and reflectance (R) where A = 1 − R − T. In practice, the differential reflectance over a wide spectral range is sufficient to determine the complex optical dielectric function and optical susceptibility [94, 95] using the Kramers-Kroning relation. The differential reflectance of the thin film layer (d $\ll \lambda$) at normal incidence is proportional to the absorption properties of the film and is expressed as [92]

$$\frac{\triangle R}{R_0} = \frac{4}{n_0^2 - 1} A(\lambda) \tag{3.2}$$

where $A(\lambda)$ represents the absorbance of the thin film and n_0 is the refractive index of the substrate which is assumed to be constant.

Our TMD samples supported by PDMS are ideal for implementing the DRS method because the PDMS has a refractive index of 1.43, resembling a transparent glass substrate. The supported layers preserve the absorbance spectral shape as the suspended layers [94].

The schematic of the DRS setup is illustrated in Fig. 3.7(a), which is similar to the PL setup as they share the same objective and BS. There are two distinctions between them. Firstly, DRS utilizes a broadband light source to illuminate the sample; Secondly, the reflected light is guided to the same spectrometer without the need for a long-pass filter to block the pumping laser. The broadband light source employed in our study is a supercontinuum light source (compact-SuperK from NKT photonics) which covers a wide spectrum typically ranging from 400 nm to 2400 nm. A 532 nm long pass filter is placed in front of the SuperK as the spectrometer is not sufficient to detect this short wavelength and we keep the incident power as low as possible to prevent damage to samples. The average intensity measured is around 67 nW.

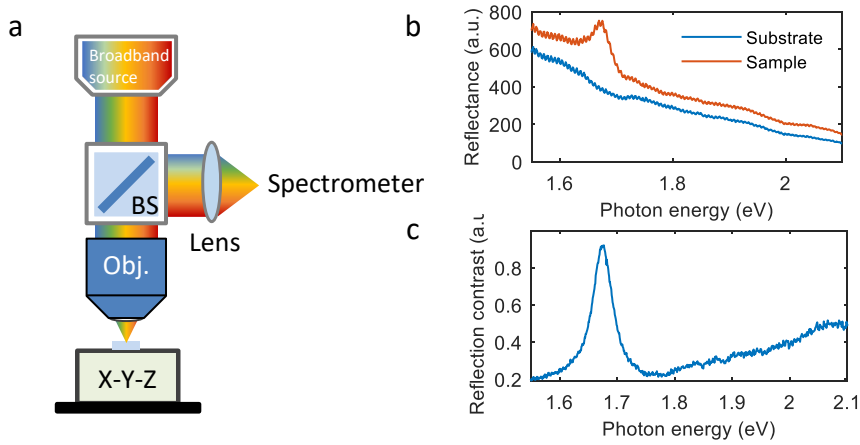

Figure 3.7. Differential reflectance spectroscopy. (a) A schematic of the DRS setup. Samples are illuminated by a broadband light source (compact-SuperK from NKT photonics). (b) Raw reflectivity recorded from the PDMS substrate R_0 (blue) and the monolayer WSe_2 on PDMS sample R (red). (c) Differential reflectivity $(R\text{-}R_0)/R_0$ of monolayer WSe_2 obtained by processing data from (b).

Figure 3.7(b) shows the reflectivity spectra obtained from the PDMS substrate (R_0, blue curve) and the monolayer WSe_2 on PDMS sample (R, red curve), respectively. The calculated differential reflectivity spectrum of monolayer WSe_2, illustrated in Fig. 3.7(c), clearly evidences the A exciton state at 1.673 eV. In addition, there appears a non-distinct broad peak around 2.069 eV, which is likely to be the B exciton. As this spectral range is challenging the detection limit of the instrument (corresponding to 600 nm, i.e., 2.067 eV), we will not discuss it further. From Fig. 3.7(b) and (c), we can tell the differential reflectivity eliminates the contribution of the substrate and strongly enhances the visibility of optical transitions.

Our results show a flat background thanks to the transparent substrate. The DRS technique has also been employed for TMD flakes on the SiO_2/Si substrate. In this case, the resulting peaks will be superimposed on a broad background, which arises from the interference effects induced by the SiO_2 layer located between the TMD layer and the Si substrate.[2]

DRS and PL

PL and DRS are both linear optical processes, and the nonlinear optical process will be discussed later in the second harmonic generation section (Section 3.2.3).

[2]Ref. [31] stated that the interference does not significantly impact the measured energies in their supplementary material. However, Ref. [96] reported that the substrate-related interference effect did affect excitonic features and suggested that the optimized SiO_2 thickness is 50-100 nm to investigate the exciton properties.

As mentioned before, DRS is regarded as the measure of the absorption from which the ground and excited excitonic states of the fundamental optical transition can be determined[3]. It is used to deduce the energy levels of materials, for instance, obtaining spin-orbit coupling-induced valence band splitting [97, 98] based on the presence of A and B exciton features.

The PL process involves absorption, relaxation and recombination. And the recombination of excited states can occur through radiative or nonradiative processes. A PL process is intricate, as the radiative recombination of states is susceptible to the influence of various factors, such as phonons and defects, and PL probes the population of states. PL spectroscopy is a powerful method to detect radiative optical transitions, including direct exciton transitions, defect states in the gap and exciton complexes that possess such a weak oscillator strength that it is difficult to trace in absorption. However, its application to indirect band gap semiconductors and detect dark exciton states are challenging, such as momentum indirect excitons, the quenched intralayer excitons, and hybrid excitons in heterobilayers.

By comparing the PL and DR spectra, one can gain great insight into the optical properties of states within a material. For instance, it can reveal the direct bandgap nature of monolayer TMDs[4] [20, 92], and obtain the binding energy charged-exciton states [97].

3.2.3 Polarization-resolved second harmonic generation (SHG)

The polarization-resolved second harmonic generation (SHG) is an efficient and sensitive tool for characterizing the crystal axis of the TMD flakes and determining the twist angle of the stacked bilayer [99–101]. In contrast to TEM microscopy, it is nondestructive and does not require special sample preparation.

Second harmonic generation is a second-order nonlinear optical process, shown in Fig. 3.8(a), where two lower energy photons with the same frequency ω are upconverted into a single photon with frequency 2ω. Under an incident electric field $E(\omega)$, the second-order nonlinear polarization $P^{(2)}(2\omega)$ be written as

$$P^{(2)}(2\omega) = \varepsilon_0 \chi^{(2)} E^2(\omega) \tag{3.3}$$

where ε_0 refers to the permittivity of free space, $\chi^{(2)}$ is the second-order susceptibility. The SHG can only occur in non-centrosymmetric crystals, that is, crystals without inversion symmetry.

The most commonly studied monolayer TMDs belong to the non-centrosymmetric D_{3h} point symmetry group with broken inversion symmetry along the armchair direction and possess large second-order susceptibilities $\chi^{(2)}$ ranging from 5 to 500 pm/V

[3]Ref. [31] observed the A, B, and C transitions from differential reflectance and the 1s, 2s, 3s, 4s, and 5s states of the A exciton by the derivative of the differential reflectance.

[4]In Ref. [20], the PL peak from monolayer MoS_2 matches the lower absorption resonance in both its position and width. And the bilayer PL emerges a low energy peak ∼300meV below the A exciton absorption peak. Besides, the quantum yield of MoS_2 strongly decreases by more than a factor of 1000 from the monolayer (direct band gap) to the multilayer (indirect band gap).

depending on excitation wavelength [102] and sample quality [103]. As a comparison, the typical value of $\chi^{(2)}$ in conventional crystals such as $NH_4H_2PO_4$ (ADP) and KH_2PO_4 (KDP) is in the range of 1 pm/V [104]. In addition, the atomic thickness of 2D TMDs eliminates the requirement for phase matching , resulting in the monolayer TMDs exhibiting strong optical SHG.

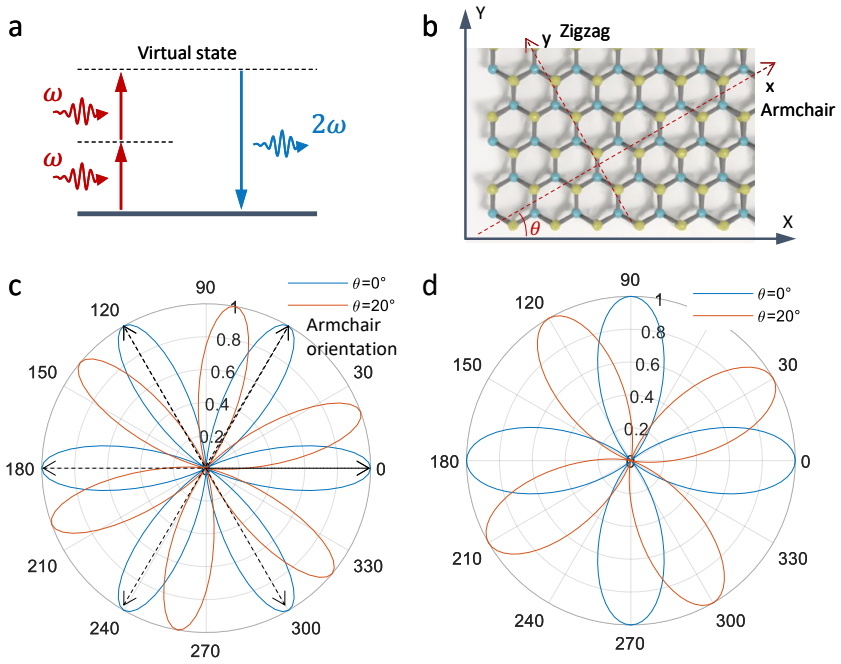

Figure 3.8. Second harmonic generation for the crystal axes determination in monolayer TMDs. (a) A schematic of the SHG process. (b) The crystalline and the laboratory coordinate systems. The armchair (x-axis) is oriented at angle θ from the laboratory X-axis. (c) Simulation of the parallel SHG intensity modulation as a function of the sample rotation θ for two different armchair orientations, θ=0° and 20°. (d) Simulation of the parallel SHG intensity modulation as a function of the linear excitation angle φ for θ=0° and 20° armchair orientations, showing a relationship of $\theta = \frac{2}{3}\varphi$.

Determination of the crystal axes of 2D TMDs [5]

The second-order nonlinear susceptibility tensor $\chi^{(2)}$ of monolayer TMD [105] has four non-zero elements $\chi^{(2)}_{xxx}$=-$\chi^{(2)}_{xyy}$=-$\chi^{(2)}_{yyx}$=-$\chi^{(2)}_{yxy}$, where x and y denote the armchair and zigzag direction, respectively. Thus, the second-order polarization in the crystal coordinate system (x, y, z) is given by

[5]This section is partially adapted from [105]

$$\begin{aligned}\begin{pmatrix} P_x^{(2)} \\ P_y^{(2)} \\ P_z^{(2)} \end{pmatrix} &= \varepsilon_0 \chi_{xxx}^{(2)} \begin{pmatrix} 1 & -1 & 0 & 0 & 0 & 0 \\ 0 & 0 & 0 & 0 & -1 & -1 \\ 0 & 0 & 0 & 0 & 0 & 0 \end{pmatrix} \begin{pmatrix} E_x E_x \\ E_y E_y \\ E_z E_z \\ 2E_y E_z \\ 2E_x E_z \\ 2E_x E_y \end{pmatrix} \\ &= \varepsilon_0 \chi_{xxx}^{(2)} \begin{pmatrix} E_x E_x - E_y E_y \\ -2E_x E_z - 2E_x E_y \\ 0 \end{pmatrix}\end{aligned} \tag{3.4}$$

Now a linearly polarized electric field normally incident on monolayer TMD at an angle φ with respect to the lab coordinate (X, Y, Z), that is $\begin{pmatrix} E_X \\ E_Y \end{pmatrix} = E_0 \begin{pmatrix} \cos(\varphi) \\ \sin(\varphi) \end{pmatrix}$. The crystalline and laboratory coordinate systems are illustrated in Fig. 3.8(b). The armchair (x-axis) orients at angle θ from the X-axis. The incident electric field in the crystal coordinate is achieved by multiplication with a rotation matrix

$$\begin{pmatrix} E_x \\ E_y \end{pmatrix} = E_0 \begin{pmatrix} \cos(\theta) & \sin(\theta) \\ -\sin(\theta) & \cos(\theta) \end{pmatrix} \begin{pmatrix} \cos(\varphi) \\ \sin(\varphi) \end{pmatrix} = E_0 \begin{pmatrix} \cos(\theta - \varphi) \\ -\sin(\theta - \varphi) \end{pmatrix} \tag{3.5}$$

Using Eq. (3.2), the second-order nonlinear polarization can be expressed in the crystal coordinates by

$$\begin{pmatrix} P_x^{(2)} \\ P_y^{(2)} \\ P_z^{(2)} \end{pmatrix} = \varepsilon_0 \chi_{xxx}^{(2)} E_0^2 \begin{pmatrix} \cos(2\theta - 2\varphi) \\ \sin(2\theta - 2\varphi) \\ 0 \end{pmatrix} \tag{3.6}$$

The second-order nonlinear polarization can be expressed in lab coordinates by multiplication with a rotation matrix.

$$\begin{aligned}\begin{pmatrix} P_X^{(2)} \\ P_Y^{(2)} \\ P_Z^{(2)} \end{pmatrix} &= \varepsilon_0 \chi_{xxx}^{(2)} E_0^2 \begin{pmatrix} \cos(\theta) & -\sin(\theta) \\ \sin(\theta) & \cos(\theta) \end{pmatrix} \begin{pmatrix} \cos(2\theta - 2\varphi) \\ \sin(2\theta - 2\varphi) \\ 0 \end{pmatrix} \\ &= \varepsilon_0 \chi_{xxx}^{(2)} E_0^2 \begin{pmatrix} \cos(3\theta - 2\varphi) \\ \sin(3\theta - 2\varphi) \\ 0 \end{pmatrix}\end{aligned} \tag{3.7}$$

Thus, the SHG intensity of the components parallel to the X axis with respect to the polarization of the incident field and the crystal axes is given by

$$I_{monolayer}^{(2\omega)} = [A \cos(3\theta - 2\varphi)]^2 \tag{3.8}$$

where $A = \varepsilon_0 \chi_{xxx}^{(2)} E_0^2$. The generated SHG follows the $\cos^2(3\theta)$ or $\cos^2(2\varphi)$ dependence, corresponding to a six-fold or four-fold rotational symmetry, according to

different experiment configurations [6]. When the TMD sample is rotated while the polarization of the excitation laser and SHG signal are fixed, the SHG pattern exhibits a known six-fold rotational symmetry [99, 106, 107] (see Fig. 3.8(c)), where the maxima of the measured SHG signal correspond to the armchair direction. In the case of only the polarization of incident light rotation, the SHG response shows a four-fold pattern [100, 101, 106] (see Fig. 3.8(d)), and the armchair direction of monolayer TMDs is determined by $\theta = \frac{2}{3}\varphi$.

In our experiment, due to the limited size of exfoliated TMD flake, rotating the polarization of the excitation laser is a more feasible way compared to rotating the sample, as it ensures the accuracy of the measurement position. Fig. 3.9(a) illustrates the schematic of our SHG setup. Nonlinear process requires an intense electric field, thus a 100 fs pulsed laser is used at a wavelength of 1550 nm with a repetition rate of 80 MHz and propagates through a polarizer to ensure its linear polarization. The orientation of the laser polarization is often controlled by the zero-order half-waveplate to avoid laser spot shifting resulting from polarizer rotation. The half-waveplate is placed in front of the objective [108, 109], so that the generated SHG signal (at 775 nm) is also modulated, which leads to the same phenomenon as sample rotation. Simultaneously rotating both the polarization of the excitation laser and the collection analyzer [110, 111] also results in a six-fold pattern in SHG response. The excitation laser is blocked using a short-pass filter. The parallel component of SHG I_X is filtered by an analyzer aligned with the first polarizer. The SHG signal is then focused on the spectrometer.

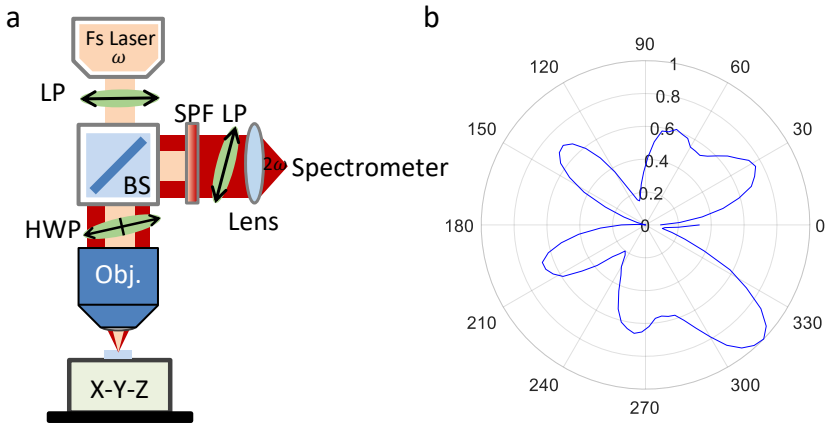

Figure 3.9. Second harmonic generation for the crystal axes determination in monolayer TMDs. (a) A schematic of the SHG setup. LP: linear polarizer, HWP: half-wave plate, SPF: short-pass filter. (b) Polar diagrams of the experimental SHG intensity as a function of the excitation polarization angle.

[6] A clear comparison of SHG patterns with respect to experiment configurations can be found in the supplementary material from Ref. [106]

The result of the experimental SHG intensity polar diagrams is displayed in Fig. 3.9(b), showing a six-fold symmetry pattern with different maxima and minima in each petal. We attribute the butterfly pattern to the polarization-dependent beam splitter (BSW29R from Thorlabs). The BS shows strong polarization dependence with 60% (40) reflectance for S-(P-)polarized light, resulting in a change of SHG intensity and polarization. Therefore, in this project, the SHG experiments are performed at Aalto University with the help of Yi Zhang.

Determination of the stacking order of TMD bilayers

In the bilayer scenario where two monolayers are stacked together, the total SHG generated by the twisted bilayer is a result of the interference of SHG from two individual monolayers and is described by

$$I_{Bilayer}^{(2\omega)} = [A_1 cos(3\theta - 2\varphi) + A_2 cos(3(\theta + \triangle\theta) - 2\varphi)]^2 \tag{3.9}$$

where A_1 and A_2 refer to the two monolayers, $\triangle\theta$ is the twist angle between them. When the two monolayers are aligned $\triangle\theta$=0°, i.e., in the R stacking, the SHG signal from the bilayer is a result of constructive interference, resulting in total SHG intensity larger than that of each monolayer. For instance, in a homobilayer where A_1=A_2, the SHG intensity is four times stronger than that of the monolayer. In the case of H stacking $\triangle\theta$=60°, destructive interference occurs, leading to a quenching of SHG intensity. Therefore, the twist angle of the bilayer can be determined.

3.2.4 Time-correlated single photon counting (TCSPC)

Time-correlated single photon counting (TCSPC) is a commonly used technique to investigate the time-dependent behaviour of photon emission. This technique enables the determination of the average duration for which a particle remains in an excited state before undergoing a transition to another state, commonly referred to as lifetime.

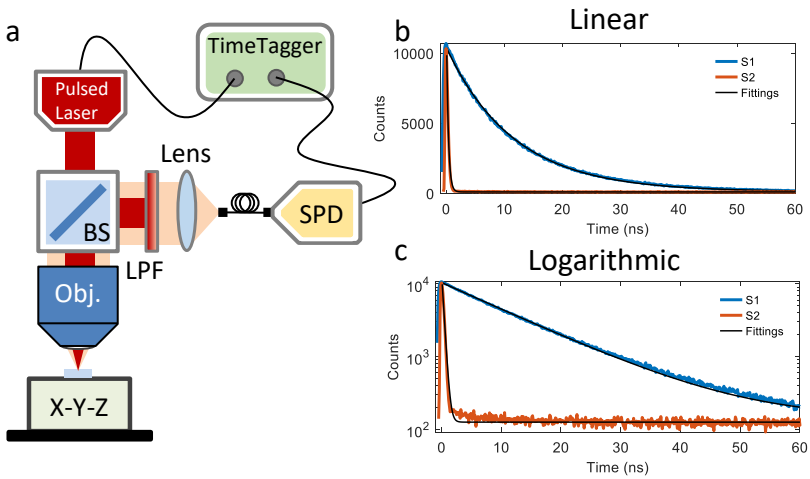

Figure 3.10. Time-correlated single photon counting (TCSPC) measurement. (a) Schematic of the TCSPC setup. SPD: single photon detector. The photon decay of different MoS_2/WSe_2 heterobilayer samples (red and blue curve) as a function of time interval on a linear scale (b) and a logarithmic scale (c). The black curves are the exponential fit for each lifetime dataset.

The schematic of our TCSPC setup is illustrated in Fig. 3.10(a), which comprises a pulsed laser (Laser Head: LDH-IB-640-B, Driver: Taiko PDL M1 from PicoQuant), a single photon detector (ID220-FR-MMF from IDQ), and a time tagger (TT20 from Swabian Instruments) that measures time intervals. The laser sends an optical pulse to excite the sample and simultaneously synchronizes the electrical pulse signal to trigger the time tagger (t_{start}). The single photon detector detects the emitted photon from the sample, which sends an electrical signal to the time tagger (t_{stop}). The arrival time (t_{stop}-t_{start}) is determined between the excitation pulse and detected photons and is recorded in a histogram [112]. With periodic excitation, fluorescence decay can be reconstructed. This technique is essentially a statistical process.

In our experiment, the pulsed laser operates at a wavelength of 637 nm, the same as the CW laser, with a pulse width of less than 90 ps and a maximum repetition rate of up to 100 MHz, corresponding to a time interval of 10 ns. Since the IX lifetime is in the order of tens of nanoseconds, a lower repetition rate is required to ensure that

the photon fully decays before the next pulse arrives. Here, we typically employ a 10 MHz repetition rate to quantify the lifetime of the IX.

Fig. 3.10(b) displays typical exponential decay curves we measured from different MoS_2/WSe_2 heterobilayers, where sample 1 (S1) exhibits a much slower decay than sample 2 (S2). The experimental data are fitted by utilizing the equation $y = e^{-\frac{t}{\tau}}$, where τ represents the lifetime. To visually evaluate the quality of the data falling upon an exponential curve, plotting the data on a logarithmic scale is recommended (see Fig. 3.10(c)). As shown in the figure, the fitting results align well with the data points. By employing this method, we obtain the lifetime of S1 and S2 as 11.62 ns and 320 ps, respectively.

The fast decay indicates that our system possesses a narrow Instrument Response Function (IRF) width of less than 320 ps. Since we do not have a suitable laser for the required wavelength, we have not measured the IRF of our equipment. We believe the fast decay is already approaching our system's IRF, given that the timing resolution of our SPD is at a minimum of 250 ps. For a sample with a short lifetime, deconvolution is necessary as the measured decay is the convolution of the physical process of exponential decay and the IRF. However, for the sample with a longer lifetime in the nanosecond range, this short IRF has practically no effect.

When conducting TCSPC measurements, it is important to pay attention to certain details. For example, the voltage range that TT20 can accept is -0.3 to 5V, but the sync output voltage signal of the pulsed laser is negative (< -0.8 V). Therefore, a signal inverter (SI100) is required to convert the electrical signal into a positive value. It is also important to note that the sync output voltage will change with the change in repetition rate.

During testing, we need to set some parameters of the time tagger, such as dead time and trigger level. We have found that the trigger level has a significant impact on the measurement results, and we also encounter data overflow problems, which require the use of conditional filters to solve. These two points are discussed in detail below.

Trigger Level

The trigger level is a crucial parameter for the measurement as it affects the time resolution. Even though the SPD detector has a very clean rectangular response with a peak voltage of 3.44 V (see Fig. 3.11(c)), we observe significant differences in decay curves when adjusting the trigger level of the SPD channel to 1 V and to 1.6 V, as shown in Fig. 3.11(a-b). Specifically, the 1 V setting shows a sharp rising edge, while the 1.6 V setting exhibits a broader rising edge, accompanied by oscillations in decay.

To achieve the highest time resolution, one should select a trigger level at which the slope of the detector pulse is highest (i.e. the slew rate is highest), where fluctuations have the least impact on the time. Around 1.6 V, the slope appears to fluctuate (see the arrows in Fig. 3.11(c)), which might explain this phenomenon. In practice, it is recommended to sweep the trigger level until time resolution is optimized. In our

experiment, we choose a trigger level of 1 V for the SPD channel and 0.5 V for the pulsed laser channel.

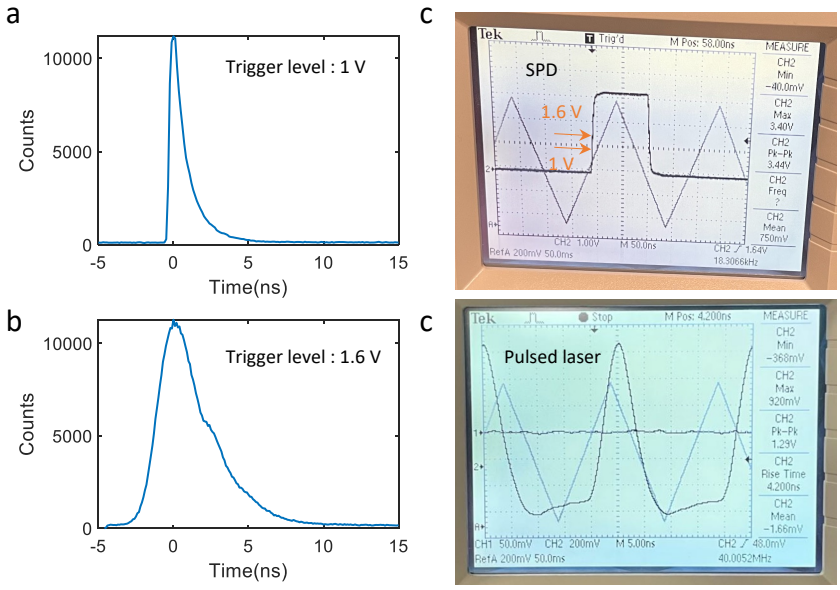

Figure 3.11. (a) A typical decay at an SPD trigger level of 1V, showing a sharp rising edge. (b) A decay at an SPD trigger level of 1.6 V, showing a broadening rising edge. (c) Electrical signal from the SPD in oscilloscope (d) Electrical signal from the pulsed laser after SI100 in oscilloscope

Overflow and Conditional Filter [7]

The time tagger (TT20) is capable of continuous streaming of about 8 million tags per second on average. Due to the high-frequency signal from the pulsed laser, buffer overflows occur, causing parts of the time tags lost. So we employ the conditional filter to decrease the time tag rate, using the SPD channel to filter the high data rate channel. One may find the lifetime curve is cut and one part is shifted by one period, as shown in Fig. 3.12. This indicates that there is a physical delay between these two channels. Given that the TT20 lacks the capability to introduce adjustable hardware delay, the delay can only be compensated by external delays, either optical path length or coaxial cable length. In order to introduce an additional delay of approximately 30 ns (see Fig. 3.12), one would need to increase the optical path length by around 9 meters or add around 6 meters of coaxial cable (the speed of an electrical signal is about 2/3 that of light). Given the length, we process the data by

[7]This section is partially adapted from [113]

cutting and linking the signal from the left to the right. We have not observed any issues with processing the data in this manner, as illustrated in Fig. 3.10(b-c).

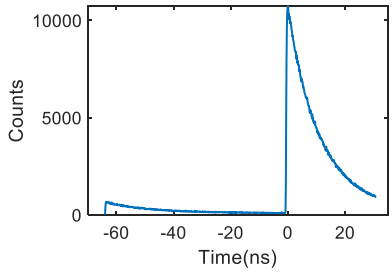

Figure 3.12. The photon decay curve as a function of time with condition filter.

CHAPTER 4

Measuring moiré excitons at room temperature

It is by now widely recognized that moiré superlattices can form due to a small twist angle and lattice mismatch between two monolayers [114]. The appearance of moiré superlattices creates a lateral periodic potential for excitons, resulting in exciton localization (known as moiré excitons), which has been widely observed at cryogenic temperatures [46, 66, 115]. From first-principle calculations [46, 62], the depth of the moiré potential is predicted to be approximately 100-200 meV, much larger than the thermal energy of ∼25 meV at room temperature. A very recent experiment [72] correlates the multipeak feature in IX emission spectra from free-standing WS_2/WSe_2 heterobilayers with moiré IXs. However, strong evidence for the presence of moiré potential at room temperature is still lacking. In this chapter, we will focus on the experimental studies about the MoS_2/WSe_2 heterobilayer on PDMS, followed by a detailed discussion of the results about the existence of moiré potential at room temperature and its impact on excitonic emission. This chapter is divided into four sections.

The first section gives basic optical properties of MoS_2/WSe_2 heterobilayers. Our hyperspectral imaging result shows a good sample quality, evidenced by the homogeneity in the strong quenching of WSe_2 exciton emission and emergence of IX emission.

The next three sections are based on our unpublished article *arXiv:2302.01266 (2023)* [116]. In the second section, we show the existence of room-temperature moiré excitons in MoS_2/WSe_2 heterobilayers by twist angle-dependent PL measurements, power-dependent PL measurements, and twist angle-dependent differential reflectance spectroscopy.

In the third section, we carry out the time-resolved PL dynamics to study the influence of the moiré potential on the IX. The moiré-suppressed non-radiative recombinations give rise to a long IX lifetime, which is beneficial for our further study on laser applications.

The fourth section summarizes the impact of moiré potential on IX at room temperature and its potential benefits for laser applications.

4.1 Fundamental optical properties of MoS_2/WSe_2 heterobilayers

Compared to thrive $MoSe_2/WSe_2$, the optical study of MoS_2/WSe_2 has been progressing slowly, possibly due to the fact that the fundamental IX emission of MoS_2/WSe_2 heterobilayers (below 1.1 eV) cannot be detected by Si detectors. At the initial studying stage, several experiment works reported an observation of IX emission wavelength in MoS_2/WSe_2 heterobilayers around 800 nm (1.55 eV) [117, 118]. However, the density functional theory (DFT) calculation and STS measurement have predicted that the IX resonance is below 1.3 eV [37, 71]. And the observed exciton emission around 800 nm has been proven to originate from the indirect K-Γ transition rather than K-K transition [119]. In 2019, Tony F. Heinz's group [47] and Weibo Gao's Group [14] did observe a fundamental IX emission below 1.1 eV (1240 nm and 1120 nm, respectively). Such a long wavelength emission is compatible with the well-developed silicon photonics platform.

In our study, we focus on MoS_2/WSe_2 heterobilayers. The band alignment of MoS_2 and WSe_2 monolayers around ±K point is illustrated in Fig. 4.1, showing a bright K-K transition of IX around 1240 nm [47]. Monolayer MoS_2 and WSe_2 are exfoliated mechanically and stacked with the dry transfer technique (see fabrication details in Chapter 2) to obtain a clean interface and high-quality optical properties. All the measurements mentioned in Chapter 4 are carried out at room temperature on MoS_2/WSe_2 heterobilayer on the PDMS substrate unless specified otherwise.

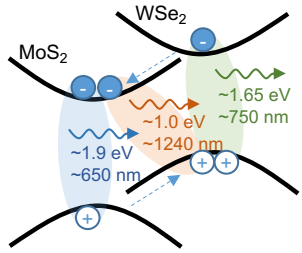

Figure 4.1. Schematic of the type-II band alignment in MoS_2/WSe_2 heterobilayers. The blue and green colours indicate intralayer excitons in monolayer MoS_2 and WSe_2, and the orange indicates IX in MoS_2/WSe_2 heterobilayers. The dashed arrows show interlayer charge transfer processes.

PL of MoS_2/WSe_2 heterobilayers

We performed hyperspectral imaging for a representative heterobilayer sample shown in Fig. 4.2(a). The sample has several regions, including monolayer and bilayer WSe_2 regions (denoted as Regions I and II), and heterobilayer regions with different interlayer couplings (Regions III and IV). The sample is excited using a CW 637 nm laser with a spot size of 1 µm at a power of 50 µW. The mapping area is highlighted by the black box in Fig. 4.2(a), scanned with a step size of 500 nm.

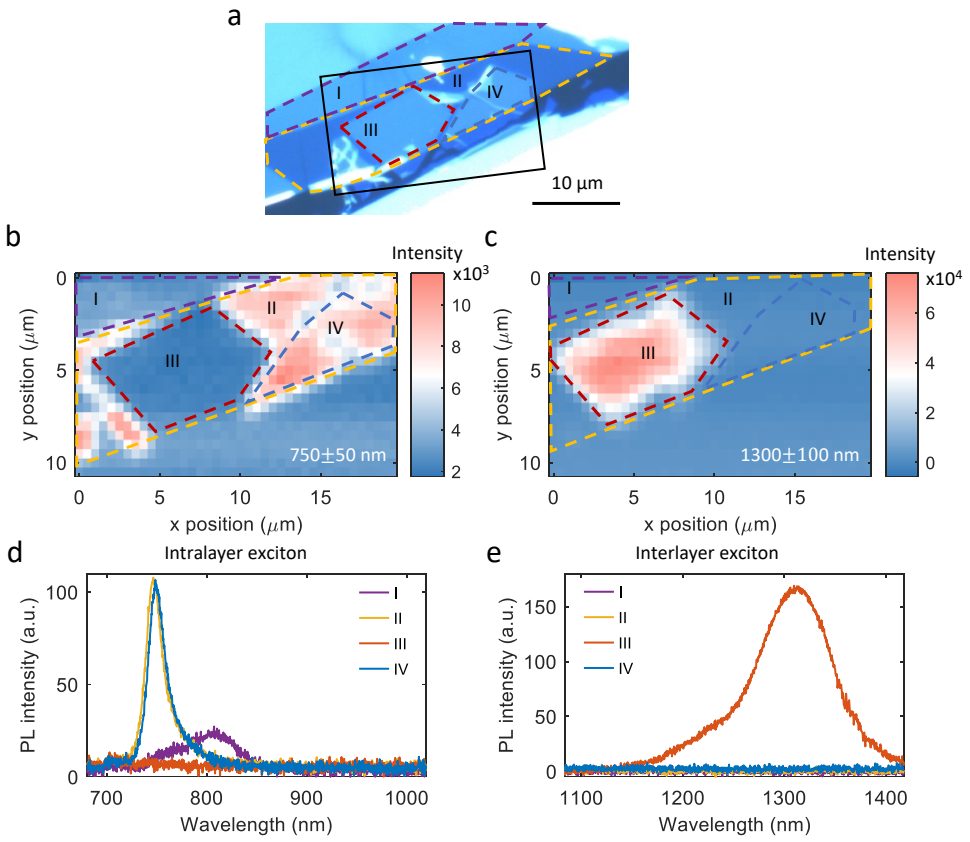

Figure 4.2. Hyperspectral imaging of MoS_2/WSe_2 heterobilayers. (a) Optical microscope image of a representative heterobilayer sample. Purple (Region I), yellow (Region II), red (Region III) and blue (Region IV) dashed lines encircle, respectively, bilayer WSe_2, monolayer WSe_2 regions, and heterobilayer regions with strong and weak interlayer coupling. The black box highlights the PL mapping area. 2D images of PL intensity distribution of the WSe_2 excitons (b) and IX (c) in the heterobilayer sample. The corresponding PL spectra from these regions are displayed in (d-e).

We display PL 2D images by integrating emission intensity around WSe_2 A exciton resonance (750 ± 50 nm) and IX resonance from K-K transition (1300 ± 100 nm) in Fig. 4.2(b) and (c), respectively. The comparison of PL spectra from these regions is shown in Fig. 4.2(d-e). The monolayer WSe_2 (Region II) and bilayer WSe_2 regions (Region I) can be clearly resolved by their significant discrepancy in emission energy and PL intensity thanks to the direct band gap nature of monolayer WSe_2. heterobilayer Region IV remains the same optical properties of monolayer WSe_2 (Region II), indicating a weak interlayer coupling between monolayer MoS_2 and WSe_2.

On the contrary, Region III exhibits good quality. We observed over three orders of magnitude quenching of intralayer exciton emission compared to the monolayer WSe_2 in a strong interlayer coupling HB. Due to the interlayer charge transfer, the population of intralayer excitons in heterobilayers decreases, thereby decreasing the PL yield of intralayer exciton. The strong PL emission from IX resonance (less than 1.1eV) is in good agreement with its bright K-K transition. Besides, it shows good homogeneity in intralayer exciton quenching and IX emission. In all, such good samples give us the opportunity to observe moiré exciton at room temperature.

DRS of MoS_2/WSe_2 heterobilayers

To further investigate the optical properties of MoS_2/WSe_2 HB, we carry out differential reflectance spectroscopy (DRS), which gives information about optical transitions. The absorption spectrum is more robust against the influence of defects than PL data [41]. The experimental details are described in Section 3.2.2.

Fig. 4.3 displays the absorption spectra of monolayer MoS_2 (red), WSe_2 (blue) and MoS_2/WSe_2 heterobilayer (green). Monolayer MoS_2 and WSe_2 exhibit strong oscillator strength of A exciton at 1.675 eV and 1.906 eV, respectively. heterobilayer shows a generally larger absorption range from 1.426 eV to 2 eV (right part of the green line) than the absorption of each monolayer because heterobilayer consists of two monolayers. The heterobilayer also exhibits absorption peaks shift relative to the two intralayer excitons.

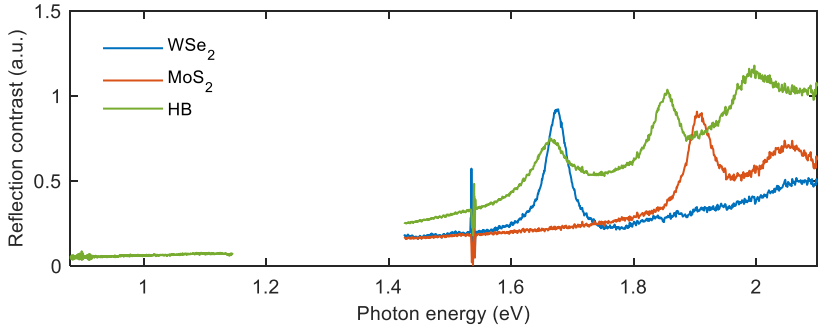

Figure 4.3. Differential reflectance spectra of monolayer MoS_2 (red), WSe_2 (blue) and MoS_2/WSe_2 heterobilayer (green). Monolayer MoS_2 and WSe_2 exhibit strong oscillator strength of A exciton at 1.675 eV and 1.906 eV, respectively. The heterobilayer shows strong oscillator strength at the intralayer exciton range (1.426 eV - 2 eV) and small oscillator strength at the IX range (below 1.14 eV).

On the contrary, the transitions coming from interlayer excitons (left part of the green line) are difficult to observe. The absorption phenomenon is indeed different from the PL, where the emission of intralayer excitons is strongly quenched and IX emerges. The explanation for this lies in the formation of IX states. In type-II HB, the excited intralayer excitons quickly separate into electrons in MoS_2 and holes in WSe_2 via an ultrafast charge transfer process. Our result clearly shows the weak absorption of IX, which could be a good candidate for lasing applications.

As the IXs do not have a sufficient oscillator strength, it is difficult to measure the absorption directly via DRS method. In 2022, Tony F. Heinz's group [41] reported a direct measurement of the optical absorption of IX states in $MoSe_2/WSe_2$ heterobilayers using electromodulation spectroscopy, showing the oscillator strengths of IX are three to four orders of magnitude smaller than those of the intralayer resonances.

Blisters

Blisters are inevitable in heterobilayers. It has been stated in Ref. [68] that blisters do not dominate the photoemission yield from the MoS_2/WSe_2 heterobilayer. Furthermore, it has been systematically studied in MoS_2/WSe_2 heterobilayers in Ref. [120] using the tip-enhanced photoluminescence (TEPL) technique which gives a high spatial resolution down to 30 nm. They observed that the PL of intralayer exciton from the blister exhibits a redshift due to strain, but the PL emission from IX can only be observed in the flat areas due to the strong interlayer coupling between the layers. Therefore, blisters found in the heterobilayers increase interlayer spacing and prevent the formation of IX emission. We believe that the measured PL emission of IX only comes from the clean regions.

4.2 Twist-angle-dependent optical properties

The twist angle between two layers affects the momentum mismatch of K valley and moiré pattern, thus having a significant impact on excitons. Here, we study the behaviour of excitons in heterobilayers in relation to twist angles. We prepare more than 25 MoS_2/WSe_2 heterobilayer samples with diverse twist angles. The twist angles of stacked heterobilayers are determined based on the straight edges of the constituent materials and will be discussed later.

4.2.1 Twist-angle-dependent PL

Fig. 4.4(a) displays the normalized PL spectra from different heterobilayer samples, showing a broad emission range from around 1100 nm to 1300 nm. The peak energy of IX emission as a function of the twist angle θ is plotted in Fig. 4.4(b). We observe a strong twist angle-dependence below 3°. As the twist angle increases, the IX emission peak tends to shift to higher energy. However, at large angles, it remains constant. For angles above 10°, we barely detect a signal from the IX.

The angle-dependent evolution of the IX peak has been observed in $MoSe_2/WSe_2$ heterobilayers [41, 54]. Tony F. Heinz's group [41] ascribed the energy shift to the moiré potential on top of the twist angle-dependent momentum mismatch, as shown in the magenta line in Fig. 4.4(c). When considering only the momentum mismatch between the K valleys of the constituent materials, the calculated energy shift (cyan line) is small and not enough to explain the magnitude of the observed energy shift. In our case, we observe a remarkable energy shift of 200 meV and we believe it has a connection with the moiré effect.

The light red line in Fig. 4.4(b) is a guide to the eye, showing the threshold of the twist angle around 3°, consistent with the experimentally observed moiré exciton in WSe_2/WS_2 heterobilayers with a large lattice mismatch at a temperature of 10 K [66].

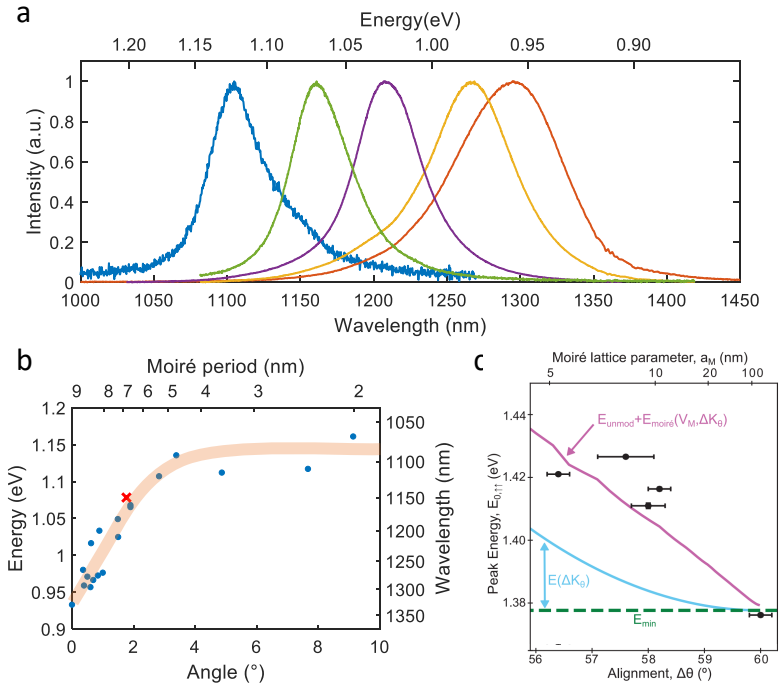

Figure 4.4. Twist angle-dependent IX emission from MoS_2/WSe_2 heterobilayer. (a) PL spectra of IX emission from different heterobilayer samples. (b) IX emission energy as a function of twist angle. The light red line is a guide to the eye. The red cross marks the data achieved from polarization-resolved SHG measurement, taken from Ref. [116]. (c) Theoretical IX energy shift as a function of twist angle when considering only the momentum mismatch (cyan line) between the K valleys of the constituent materials and considering moiré effect (magenta line), taken from Ref. [41].

Angle determination

There are many ways to determine the twist angle, such as TEM microscopy and polarization-resolved SHG measurements (details in Section 3.2.3). Here, we obtain the twist angle based on the straight edges of the stacked heterobilayers, same as reported in previous works [65, 106]. Compared to other methods, reading angle data directly from images is much more convenient and time-saving. Although this method is not rigorous, it is still very credible if a large amount of data is analyzed. Ref. [106] has shown a linear relationship between the angle from photos and from SHG measurements. We also carried out a polarization-resolved SHG measurement at Aalto University, as shown in Fig. 4.5. The measurement was performed by Yi Zhang and was carried out with an excitation wavelength of 960 nm (repetition rate 2 kHz) from an amplified Ti:sapphire femtosecond laser system (Spectra-Physics Solstice Ace). The polarization orientation of the excitation beam was tailored by rotating a

half-wave plate (HWP). The laser light after the HWP was focused onto the sample by a 40x objective lens (NA=0.75, Nikon). The transmitted SHG signal was collected by another 40x objective lens (NA=0.5, Nikon), and passed through a linear polarizer. A 700-nm short-pass filter was placed after the polarizer to cut off the excitation beam. The final signal was detected by a photomultiplier tube (PMT) (Hamamatsu).

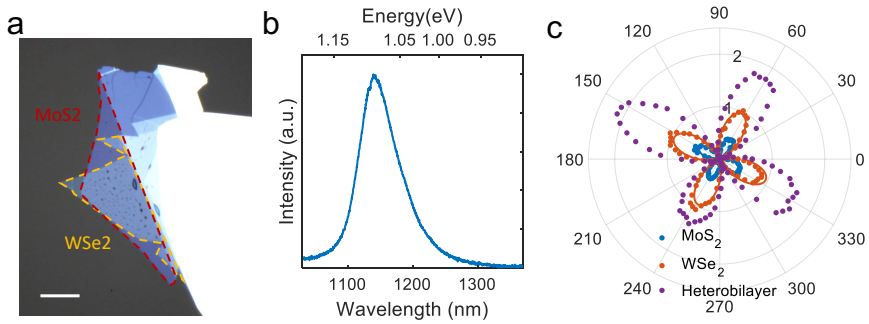

Figure 4.5. Twist angle determined by polarization-resolved SHG measurement. (a) The optical microscope image of the sample. Scale bar: 10 µm, taken from Ref. [116]. (b) IX emission spectra, taken from Ref. [116]. (c) Polarization-resolved SHG pattern from monolayer MoS_2 (blue), WSe_2 (red) and MoS_2/WSe_2 heterobilayer (purple). The experimental data are represented by dots, and fitting results are represented by curves. The twist angle derived from SHG measurements is ∼1.77°, corresponding to an IX energy of ∼1.089 eV, taken from Ref. [116].

As mentioned in Section 3.2.3, this kind of measurement configuration results in a four-fold SHG pattern (Fig. 4.5(c)). The polarization-resolved SHG data from monolayer MoS_2, WSe_2 and MoS_2/WSe_2 heterobilayer area are marked by red, blue, and purple dots. The heterobilayer is R-stack, evidenced by the constructive interference of SHG signal from heterobilayers compared to the constituent monolayers. We obtain a 2.65° relative angle between the petals of monolayer MoS_2 and WSe_2, resulting in a twist angle of 1.77°. The data is marked as a cross in Fig. 4.4(b), showing a reasonable agreement with the twist angle dependence of the IX energy.

4.2.2 Power-dependent PL

We further perform power-dependent PL measurements. Fig. 4.6 displays the power-dependent evolution of the IX PL spectra for two representative samples with different twist angles up to the same pumping level.

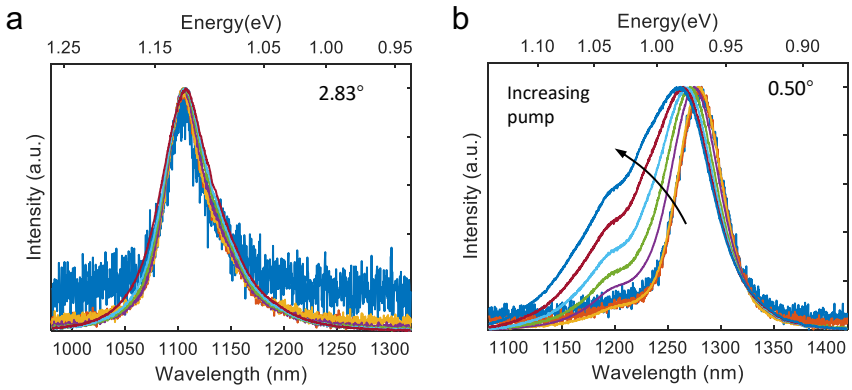

Figure 4.6. Power-dependent PL spectra of heterobilayers with twist angles of 2.83° (a) and 0.50° (b) up to the same maximum power level of 500 µW. For the heterobilayer with a small twist angle in (b), the evolution with power exhibits a strong blue shift and the emergence of high-energy states, indicated by the black arrow, taken from Ref. [116].

For a heterobilayer of $\theta = 2.83°$ (Fig. 4.6(a)), the IX has an emission energy of ∼1.12 eV (∼1107 nm) and this energy remains constant with increasing power. In stark contrast, a remarkable blueshift and the emergence of high-energy states are observed when $\theta = 0.50°$ (Fig. 4.6(b)). We attribute these to the existence of the moiré potential that acts as an exciton reservoir for different exciton states and enhances the exciton-exciton interaction. As the potential confines excitons laterally resulting in quantized energy level [46], IXs obtain a larger chance to fill higher-energy moiré excitonic states when the pumping power increases. The filling to higher-energy states leads to the occurrence of the blue shift for the emission envelope.

We also report the observation of spectrally resolved moiré states in hBN encapsulated heterobilayers, which will be discussed in the Chapter 5.

4.2.3 Twist-angle-dependent DRS

We study the angle dependence of optical transitions on the energy range from 1.6 eV to 2 eV. The angle-dependent evolution of differential reflectance spectra is displayed in Fig. 4.7(a). The top three spectra come from monolayers WSe_2, MoS_2 and uncoupled trilayer (1L-WSe_2/2L-MoS_2) [1]. As a reference, the vertical blue, red and green dashed lines present A exciton transitions from monolayer WSe_2, MoS_2 and bilayer MoS_2, respectively. From the top to the bottom, the IX emission wavelength becomes shorter, corresponding to the larger twist angle. We put the IX emission wavelength here instead of the measured twist angle because the emission energy serves as a more accurate indicator of the angle in such a small angle range.

[1]The uncoupled 1L-WSe_2/2L-MoS_2 trilayer is evidenced by unquenched intralayer exciton emission, no IX emission, and unshifted WSe_2 exciton absorption.

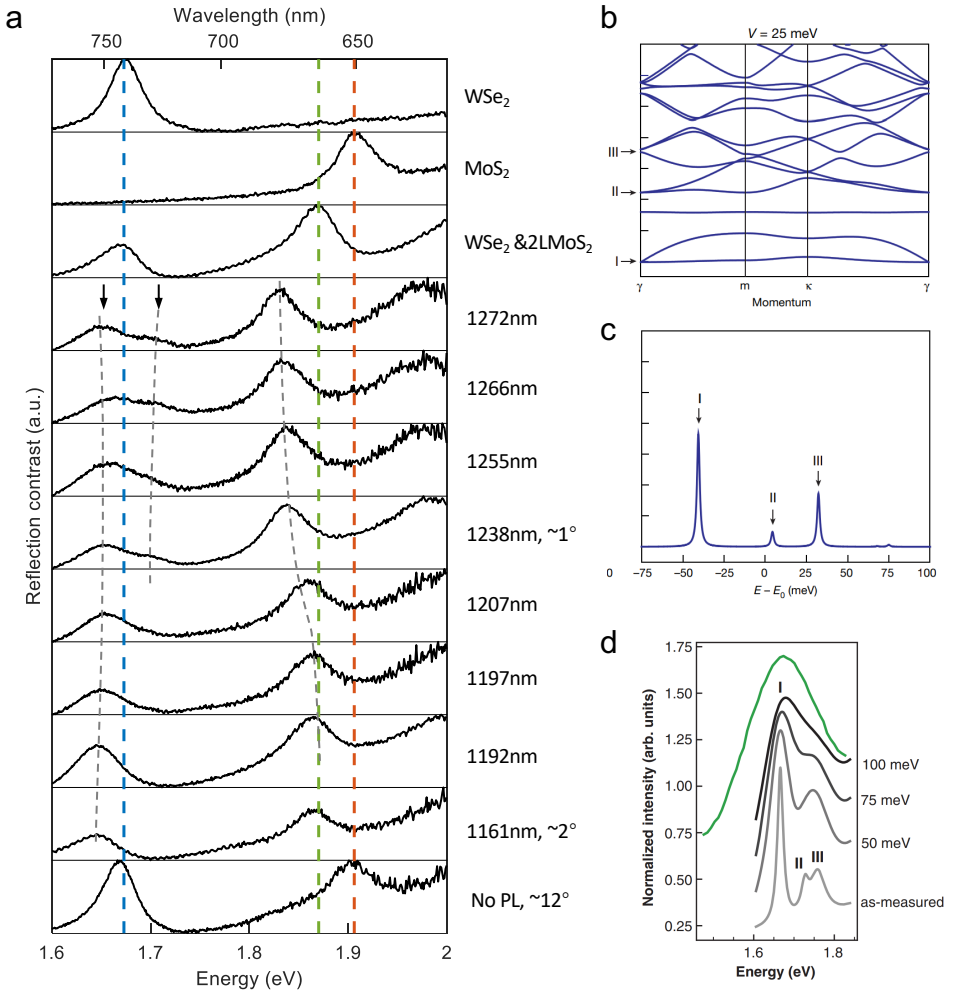

Figure 4.7. Evidence of moiré intralayer exciton. (a) Evolution of differential reflectance spectra with twist angles. The curves are shifted vertically for clarity, and the grey dashed lines track the excitonic peak evolution. The top three spectra come from monolayers WSe_2, MoS_2 and uncoupled trilayer (1L-WSe_2/2L-MoS_2). As a reference, the vertical blue, red and green dashed lines are referred to as A exciton peaks for monolayer WSe_2, MoS_2 and bilayer MoS_2, respectively. The splitting of intralayer exciton peaks (two black arrows) indicates the existence of the moiré potential. (b) Calculated dispersion of intralayer exciton in mini-Brillouin zone with moiré potential, taken from Ref. [66]. (c) Calculated exciton absorption corresponding to the optically active exciton states labelled in (b), taken from Ref. [66]. (d) Multiple moiré intralayer exciton peaks evolution with Gaussian broadening, taken from Ref. [70].

Let us first focus on the WSe_2 A exciton (blue dashed line) in the range between 1.6 and 1.75 eV. The exciton peak changes pronouncedly upon twist angle. The heterobilayer with the large twist angle (12°) shows a single exciton resonance similar to the monolayer WSe_2. When the twist angle decreases to 2° (1160 nm), the single exciton resonance red-shift. When the twist angle decreases to smaller than 1° (wavelength larger than 1240 nm), we start to observe a splitting of WSe_2 A exciton peaks (highlighted by two arrows).

In order to extract the energy position, the absorption spectra are fitted by a sum of Gaussian peaks based on the Ref. [121]. Two representative absorption spectra with fitting are displayed in Fig. 4.8(a). The double peak feature of near-aligned heterobilayer (red dots) is well reproduced by a sum of two Gaussian peaks (red line) and these two peaks show comparable oscillator strengths, while the large-angle heterobilayers can only be fitted with a single Gaussian function with a reasonable agreement. The extracted peak energy is plotted in Fig. 4.8(b). For the twist angle smaller than 1°, the splitting of two peaks remains almost constant with a peak separation of 50 meV.

The splitting of intralayer peaks around the original WSe_2 A exciton serves as strong evidence for the presence of moiré excitons at room temperature. As the moiré potential not only traps IXs but also affects the distribution of intralayer excitons in real space, a large moiré potential modifies the exciton dispersion [66, 67], generating multiple flat exciton minibands (as shown in Fig. 4.7(b)) and thus multiple peaks in the absorption spectra (Fig. 4.7(c)). The splitting of intralayer exciton peak has been observed experimentally at cryostat temperature in diverse moiré superlattice systems, including WSe_2/WS_2 [66], MoS_2/WSe_2 [52] and $MoSe_2/WS_2$ heterobilayers [122]. The intralayer exciton is split into three exciton states with peaks separated by around 70-100 meV. However, we observe a doublet resonance feature at room temperature. We ascribe it to the difficulty to distinguish the feature of two additional peaks due to linewidth broadening. As shown in Fig. 4.7(d), the three resolvable moiré peaks turn into two with Gaussian broadening of 50 meV and finally unresolvable above 100 meV [70].

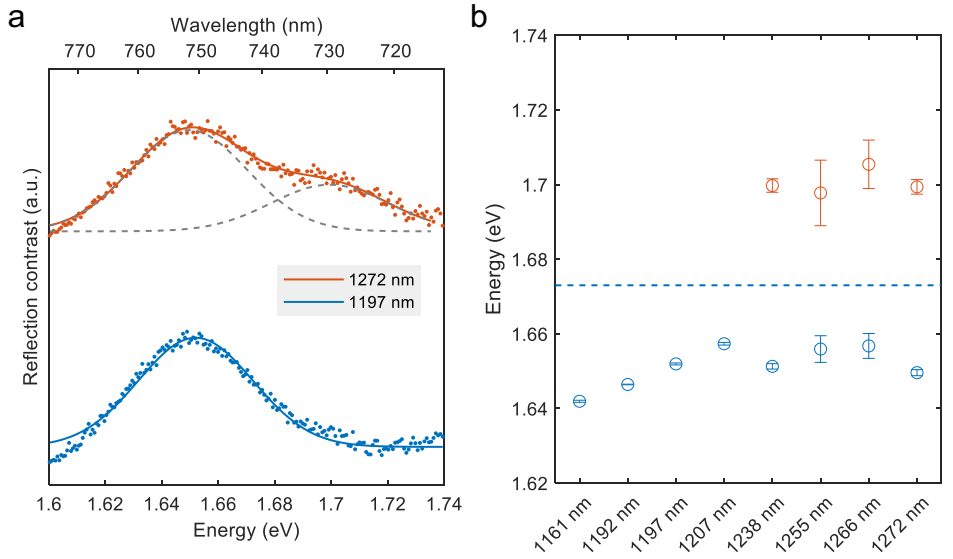

Figure 4.8. Twist angle-dependent differential reflectance spectrum evolution of WSe_2 excitonic transition. (a) Experimental differential reflectance spectra from two samples with IX emission wavelengths of 1272 nm (red dots) and 1197 nm (blue dots), respectively. The spectra are fitted with Gaussian functions (lines). (b) Energy evolution of exciton peaks extracted from Gaussian fitting. The blue dashed line refers to WSe_2 A exciton energy.

We find that the shift of the A exciton resonances serves as a good indicator for interlayer coupling between WSe_2 and MoS_2 monolayers. The best example of strong interlayer coupling is R/H-stacked homobilayers. It is free from moiré pattern due to its zero lattice mismatch and twist angle. And it has the smallest interlayer distance (around 0.61 nm), showing a redshift of A exciton resonance in the absorption spectrum [123,124]. While bilayers with weak interlayer coupling tend to preserve the properties of constituent monolayers. In Fig. 4.7(a), for the large twist angle of 12° (the bottom spectrum), the MoS_2/WSe_2 heterobilayer shows exciton resonances close to the monolayer WSe_2 and MoS_2 A exciton, indicating a weak interlayer coupling. We try to increase its interlayer coupling by squeezing heterobilayer with PDMS, but it does not help. Thus this weak interlayer coupling is not from fabrication imperfections but from the intrinsic interlayer distance.

Fig. 4.9 shows the evolution of MoS_2 A exciton peak with twist angles in heterobilayers. The A exciton resonance peaks of monolayer and bilayer MoS_2 locate at 1.906 eV (red dashed line) and 1.87 eV (green dashed line), respectively. The MoS_2/WSe_2 heterobilayer with a twist angle around 2° (1160 nm) exhibits a resonance peak close to the A exciton resonance of the bilayer MoS_2. Surprisingly, this resonance peak keeps red-shift to around 1.83 eV as the twist angle decreases. The redshift is likely caused by moiré potential because MoS_2/WSe_2 heterobilayer rarely

suffers from atomic reconstruction due to large lattice mismatch.

As we mentioned in Section 1.4, the emergence of moiré pattern changes the local stacking configurations. The energetically unfavourable stacking configurations lead to a strong repulsion and the largest interlayer distance (around 0.68 nm [123]), while the energetically favourable configurations have the smallest interlayer distance (0.61 nm). When solely considering the interlayer distance, the redshift observed in heterobilayers should not exceed that of homobilayers. Thus, we believe that the moiré potential may already play a role with twist angles smaller than 2° even though the splitting of WSe_2 exciton transition is not yet observed. The sudden drop at 1° (1240 nm) from 1.86 eV to 1.84 eV may come from the insufficient data between the two data points.

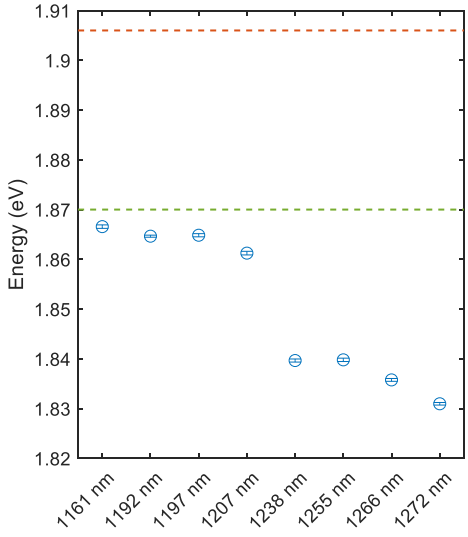

Figure 4.9. Energy evolution of exciton absorption peaks extracted from Gaussian fitting. The red and green dashed lines refer to the A exciton energy of monolayer and bilayer MoS_2, respectively.

4.3 Interlayer coupling mediated optical properties of IXs

Recent studies clearly show that the atomic registry of the moiré superlattice dictates the behaviour of interlayer electronic coupling [71], which can be used as a tuning knob for novel 2D electronic systems. Here we examine the influence of the moiré potential on the IX lifetime that plays a crucial role in population inversion.

The twist angle has a substantial impact on the IX lifetime, as it generates not only a relative shift in momentum space but also modifies the moiré supperlattices [60]. However, it is challenging to differentiate the contributions to radiative decay from the momentum mismatch (without moiré potential) and the moiré effect. To largely exclude the effect of the momentum mismatch, we choose a representative near-zero-twist-angle heterobilayer shown as the inset in Fig. 4.10(a), where the optical image shows two clearly distinguishable separated regions. These two regions (Region 1 and Region 2) can be identified by their different optical contrast, implying the presence of different interlayer coupling while simultaneously having the same twist angle.

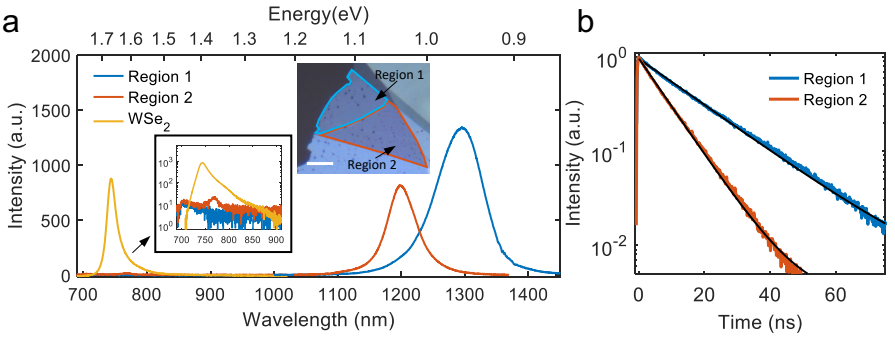

Figure 4.10. Moiré modulated IX emission. (a) PL spectra from Region 1 (blue), Region 2 (red) and a reference monolayer WSe_2 (yellow). The PL spectra of the intralayer exciton on a logarithmic scale (black frame inset) show the higher interlayer coupling in Region 1, taken from Ref. [116]. Inset: the optical image of the heterobilayer consisting of two artificially colored regions. Scale bar: 10 µm. (b) Time-resolved PL dynamics from two regions for IXs emission longer than 900 nm. The black curves are exponential fits to the data, giving an IX lifetime of 17.6 ns (8.5 ns) for Region 1 (Region 2), taken from Ref. [116].

The PL spectra shown in Fig. 4.10(a) cover the WSe_2 exciton emission (∼750 nm) and IX emission (∼1000-1400 nm). Both regions feature strong interlayer coupling supported by the approximately two orders of magnitude emission quenching of the WSe_2 A excitons. On the logarithmic scale (see the inset with black frame), the different intralayer exciton intensities from the two regions further indicate that Region 1 has a better coupling than Region 2. Compared to Region 2, the IX emission from Region 1 exhibits a brighter emission intensity and lower emission energy (see the right part of Fig. 4.10(a)). These results can be explained by:

1. Stronger interlayer coupling, i.e., the increased overlap of the wavefunctions of the spatially separated electrons and holes, results in a larger probability of IX radiative recombination.

2. The interlayer coupling determines the depth of the moiré potential [46], and stronger interlayer coupling leads to a deeper moiré potential which thus can trap IXs in lower energy states.

The increased radiative recombination due to the strong interlayer coupling usually leads to fast decay. However, our time-resolved PL measurements (Fig. 4.10(b)) show that the IXs in Region 1 feature a longer lifetime (∼17.6 ns) than Region 2 (∼8.5 ns). This counterintuitive result can be explained by the strong suppression of non-radiative recombination at elevated temperatures due to the spatial confinement of IXs with moiré potential [125] that impedes the exciton diffusion to non-radiative centers [69, 126]. We conclude that the moiré potential not only enhances the light emission of IX but also prolongs its lifetime, which is favourable for low-threshold lasing applications.

Twist angle-dependent lifetime

One may want to know the twist-angle-dependent lifetime. Unfortunately, we cannot make a conclusion about that. To illustrate it, we take an extreme example. Fig. 4.11(a) exhibits the optical properties of two heterobilayer samples (S1 and S2) with similar twist angles. The close twist angles are also evidenced by the similar IX emission energy. The quenching of intralayer exciton emission suggests that both of them have a good interlayer coupling. However, the emission IX intensity of S1 is two orders of magnitude stronger than that of S2, and there is a big difference in lifetime (Fig. 4.11(b)). The lifetime of S1 is 13.36 ns while the S2 is 310 ps, which basically reaches the time resolution limit of our setup. We attribute the weak emission and fast decay of IX in S2 to fast non-radiative recombination, probably from defects.

It has been widely reported that defect can act as centers for non-radiative recombination, lower the photoluminescence quantum yield, and obscures the intrinsic exciton radiative lifetime [83,127,128]. Defects are inevitable in atomically thin TMD crystals for now. On the one hand, the grown bulk crystal has an intrinsic defect density that varies from synthesis techniques. TMD crystals grown by chemical vapor transport (CVT) are commonly used as a typical source of exfoliation for research but suffer from high defect density. The flux-grown crystals we used possess 1−2 orders of magnitude lower defect density than the typical CVT-grown method, but it still has a defect density of $\sim 10^{11}/\mathrm{cm}^2$ [83]. On the other hand, as the atomically thin layer is susceptible to surface cleanness and strain, the van der Waals transfer technique could introduce additional defects, thus affecting their light emission at room temperature [129]. Control of the generation of extra defects is challenging and, as a consequence, affects the reproducibility of the quality of the fabricated samples. The non-radiative recombination introduced by defects would not affect the emission energy of the lowest optically active state, but will largely affect its population, thus affecting its emission intensity and lifetime. That is also why we do not compare the PL intensity and lifetime between different samples.

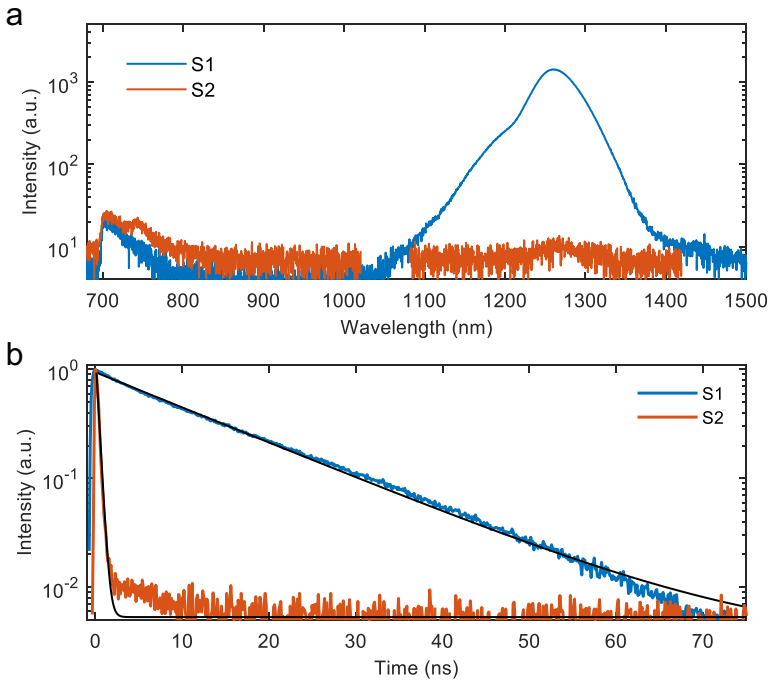

Figure 4.11. (a) PL spectra from two heterobilayers (S1 and S2) with close twist angles, plotted on a logarithmic scale. (b) Time-resolved PL dynamics from two heterobilayers for IXs emission longer than 900 nm. The black curves are exponential fits to the data, giving an IX lifetime of 13.36 ns (310 ps) for S1 (S2).

4.4 Summary

In this chapter, we have for the first time confirmed that the moiré potential can remarkably modulate the IXs at room temperature, evidenced by the strong twist angle-dependent IX emission energy shift (> 200 meV), the power-dependent energy shift, and the splitting of WSe_2 intralayer exciton resonance in absorption. The elongated IX lifetime and emission wavelength with moiré potential hold great promise for low-threshold lasing applications at optical fiber communication wavelengths.

To enhance the comprehensiveness of our experimental analysis, further low-temperature measurement is of great interest, as it enables us to compare with phenomena observed in low-temperature experiments conducted by other researchers, such as clearly resolved multiple peaks in absorption and PL spectra and rapid recombination of moiré exciton. The theoretical calculation of the emission energy of the IXs and the absorption peak of MoS_2 A excitons as a function of the twist angle when considering moiré effect is of great significance.

The observation of room temperature moiré excitons could stimulate future studies on the correlated physics, including excitonic Mott insulator and superconductivity in such twisted heterostructure systems at elevated temperatures.

CHAPTER 5

Studying the coupling of moiré IXs to a photonic cavity

In Chapter 4, we have demonstrated the presence of room-temperature moiré excitons and their potential advantages for laser applications due to the additional in-plane quantum confinement with moiré potential. This additional in-plane quantum confinement in moiré superlattices could enhance the quantum yield of light emission and potentially lead to a large optical gain at low pumping levels, akin to quantum dots which showed lower lasing thresholds than quantum wells and bulk materials [16]. However, the study of the moiré superlattice on laser performance has remained unexplored.

In this chapter, we for the first time, couple moiré IX to silicon topological photonic cavities (Fig. 5.1) and study the light-matter interaction in a weak-coupling regime. Our focus lies on investigating the impact of the moiré potential on laser performance, aiming to achieve a comprehensive understanding of optical gain from moiré excitons and its potential for energy-efficient lasers.

This chapter is based on our unpublished article *arXiv:2302.01266 (2023)* [116] and it is divided into three sections. In the first section, we briefly introduce the energy level structure of moiré IX states that allow the realization of optical gain.

The second section focuses on the photonic cavity. We explain the reason for choosing the topological nanobeam cavity reported in Ref. [130] and provide a brief introduction to the principles behind achieving a robust single mode. We adjust various parameters to obtain the desired cavity, and the simulation is carried out by Hanlin Fang at Chalmers University of Technology. The fabrication takes place in DTU Nanolab (Details in Chapter 2), and the optical properties of the cavity are characterized using our home-built PL setup (Details in Chapter 3).

The third section is the most important section of this chapter. In this section, we focus on hBN-protected MoS_2/WSe_2 heterobilayer on a nanobeam cavity, together referred to as a device. Optical characterizations of the devices primarily involve pump power-dependent PL measurements, through which we observe lasing-like behaviour.

Furthermore, we explore the threshold and spontaneous-emission suppression ratio variations when the cavity mode couples to different moiré IX states.

The fourth section provides a comprehensive summary of this chapter, highlighting both the strengths and weaknesses of our current work. Additionally, we discuss potential avenues for improvement in the future.

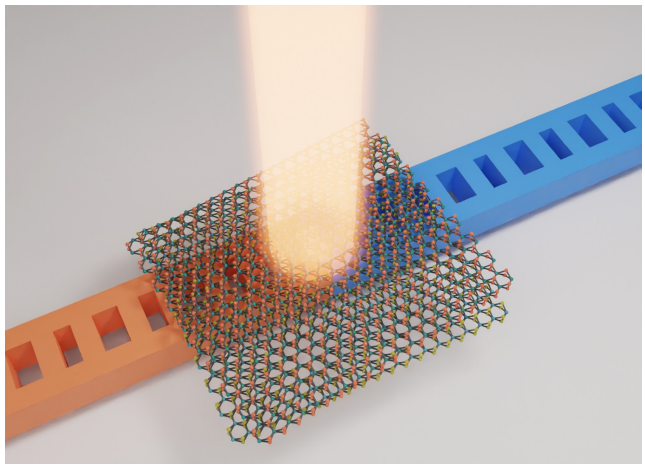

Figure 5.1. Sketch of MoS_2/WSe_2 heterobilayer on top of a topological nanobeam cavity that together exhibit lasing. hBN is absent for the clarity of moiré patterns.

5.1 Three-level systems

In order to achieve optical gain in a material, it is generally necessary to establish a state of population inversion. Fig. 5.2 shows the excitonic energy level diagram of the heterobilayer with type-II band alignment and moiré effect. It has been proposed that the type-II heterobilayer forms a three-level system and supplies optical gain for the realization of laser operation [15]. Intralayer exciton states |X> are first generated after optical pumping (cyan arrow) and follow the ultrafast charge transfer process (grey dashed arrow) to form IX states |IX>, thus achieving population inversion. The existence of moiré potential in real space leads to the formation of quantized IX energy levels, marked as |moiré IX,1>,|moiré IX,2>,|moiré IX,3>, etc. The dipolar repulsive interaction between IXs could result in a large energy shift of the absorption spectrum with respect to the PL emission spectrum, permitting optical amplification at low pump levels [131]. The potential trap in the moiré superlattice could enhance the IX-IX interaction and even form multi-exciton complexes including biexcitons and triexcitons [132]. In our system, the deep moiré potential could potentially endow the lowest energy state |moiré IX,1> with enhanced exciton binding energy and

interaction, which is beneficial for the realization of optical amplification at room temperature and low pump levels. With raising pump level, the low energy levels will be saturated and IXs tend to occupy high energy levels. This exciton-filling feature suggests that the different moiré IX states will play a role in offering optical gain at different pump levels. Designing cavity resonances to couple to those different moiré IX states is desired to understand their contribution to lasing. We will discuss it in Section 1.3.3.

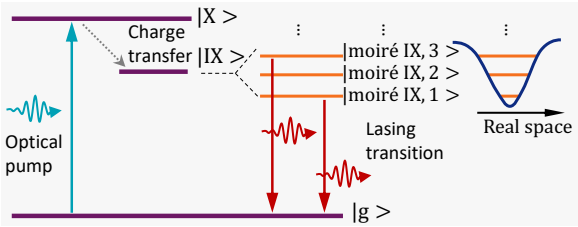

Figure 5.2. Energy level diagram of excitonic states in a type-II heterobilayer with moiré effect, taken from Ref. [116].

5.2 Topological nanobeam cavities

To explore the potential of moiré IX for laser applications, a high-quality optical cavity is desired for providing positive feedback. The cavity we adopted here is a topological photonic nanobeam cavity proposed in Ref. [130], where single-mode lasing was demonstrated from InAs quantum dots embedded in GaAs nanobeam cavity. This topological nanocavity possesses a near-diffraction-limited mode volume ($\sim 0.23(\lambda/n)^3$) and high Q factor ($> 10^4$). Its lasing application shows a high spontaneous emission coupling factor ($\beta\sim 0.03$), which is orders of magnitude larger than those for conventional semiconductor lasers [130]. High-β lasers have attracted attention for energy-efficient applications, as a large portion of the spontaneous emission is coupled into the lasing mode.

Photonic topological cavities are chosen here due to their demonstrated robust single-mode operation [130, 133], preventing mode competition, thus simplifying the study of moiré IX-cavity interaction. And the topological nanobeam cavity is robust against fabrication imperfections. Fig. 5.3(a) shows the sketch of the top view of the topological photonic crystal nanobeam cavity. The red and blue unit cells (dashed boxes) share the same periodicity (denoted as a) with different air-hole arrangements and the same band structure (Fig. 5.3(b)). However, the lowest band for the red (blue) nanobeam is topologically trivial (nontrivial), characterized by the Zak phase. At the center where the red and blue unit cells meet, a Dirac point appears at the band edge, as shown in the middle of Fig. 5.3(b). The abrupt interface formed with the inversion-symmetric points eliminates the existence of other localized modes that

are not of topological origin. I briefly introduce the amazing nanocavity here, and more details can be found in Ref. [130].

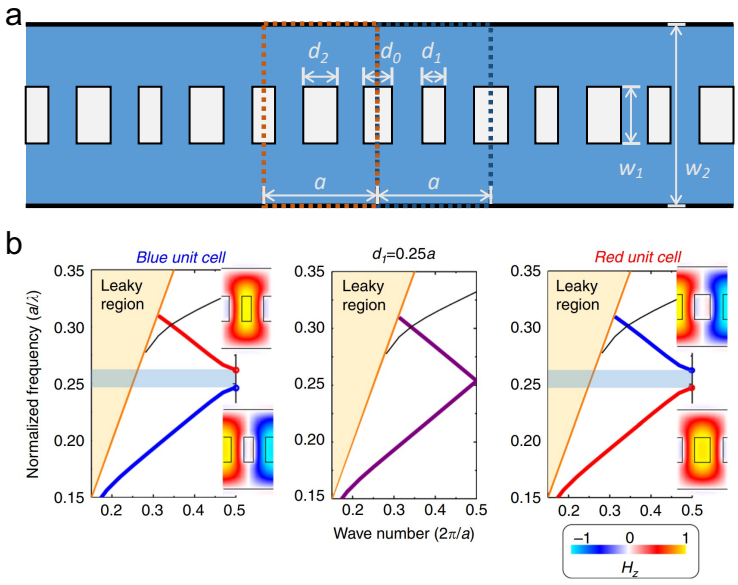

Figure 5.3. (a) Sketch of the top-view of the topological photonic crystal nanobeam cavity. The red and blue unit cells (dashed boxes) share the same periodicity (denoted as a) with different air-hole arrangements. The interface lies at the center where the red and blue unit cells meet, taken from Ref. [116]. (b) Band structures of the red and blue unit cells and wave functions at the band edges. For the case of d_1=d_2=0.25a, a Dirac point appears at the band edge, taken from Ref. [130].

In our work, we use an SOI wafer to fabricate the nanobeam, as silicon has a bandgap larger than the IX energy, and silicon is also compatible with the complementary metal-oxide-semiconductor (CMOS) process. To couple moiré IX to the topological nanobeam, the cavity mode and parameters are optimized to reach desired resonant wavelengths using the 3D finite-difference time-domain (FDTD) method (Lumerical, Ansys). We retain a SiO_2 layer to support silicon nanobeams as in Ref. [13], which is mechanically robust for the 2D material transfer process and is preferable for efficient heat dissipation. The SiO_2 supporting layer is taken into consideration in the simulation. The design and FDTD simulations for nanobeams are conducted by Hanlin Fang, one of our collaborators at Chalmers University of Technology. And fabrication is carried out by ourselves using standard e-beam lithography at DTU nanolab (fabrication details in Chapter 3). Table 5.1 lists the detailed structure parameters of the nanobeam with a fixed thickness of 220 nm. Fig. 5.4(a) shows an SEM image of the fabricated nanobeam around the center. The corresponding sim-

ulated mode profile is shown in Fig. 5.4(b). The field distribution shows the cavity mode localized at the interface.

Table 5.1. Structure parameters of the topological photonic crystal nanobeam cavities and their FDTD simulation results. The thickness of the nanobeams are fixed at 220 nm.

	a	d_0	d_1	d_2	w_1	w_2	Resonance	Q-factor
Device 1	300 nm	$0.25a$	$0.2a$	$0.3a$	$0.5a$	$1.6a$	1284.52 nm	17521
Device 2	260 nm	$0.25a$	$0.2a$	$0.3a$	$0.5a$	$1.6a$	1149.95 nm	19941

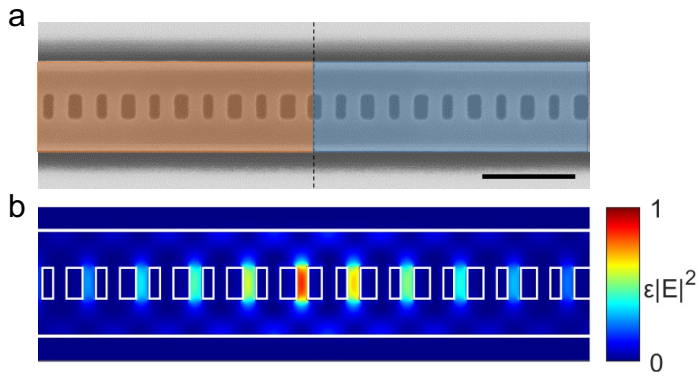

Figure 5.4. (a) SEM image of the cavity. The light red and blue areas illustrate two photonic crystals with different Zak phases, leading to the appearance of a cavity mode at their interface. Scale bar, 500 nm, taken from Ref. [116]. (b) The simulated mode profile, taken from Ref. [116].

We excite the silicon nanobeam with a CW 637 nm laser (details in Chapter 3) and observe cavity-enhanced PL spectra, as shown in Fig. 5.5. As mentioned in Chapter 4, strong pump power is required to get sufficient PL emission intensity due to the indirect-bandgap material. This creates many carriers inside the silicon nanobeam, which may lead to a blueshift in resonance and a reduction of the Q-factor. It is worth noting that this energy shift is negligible compared to the broad IX emission peak.

Thanks to the topological nature, all cavities exhibit a single-mode feature in a wide spectrum range of over 300 nm (Fig. 5.5(a)). The narrow peak originating from the cavity resonance is fitted by the Lorentz function and the extracted Q-factor is ∼3000, which is close to the resolution limit of a 600 lines/mm grating (Fig. 5.5(b)). Even though a denser grating provides a higher spectral resolution, it also results in a shorter detection window and a much weaker signal. It would be time-consuming to characterize a large number of cavities.

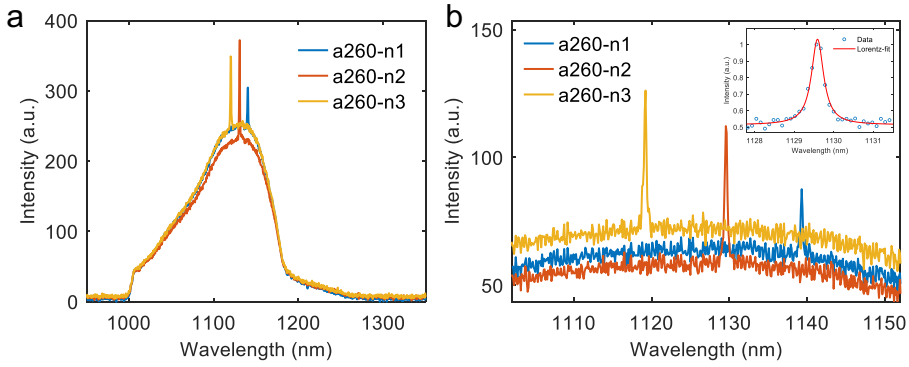

Figure 5.5. (a) PL spectra from bare silicon nanobeams with a 150 lines/mm grating. (b) PL spectra from bare silicon nanobeams with a 600 lines/mm grating. Inset: Lorentz fit to the cavity mode.

5.3 Moiré excitons coupled to a photonic cavity

To explore the potential of moiré IXs for laser applications, we integrate rotationally aligned MoS_2/WSe_2 heterobilayers with our fabricated high-Q nanobeam cavity. Before transferred to the nanobeam, the heterobilayer is encapsulated within two hBN flakes to prevent potential optical performance degradation in ambient environments [13] and to suppress inhomogeneous linewidth broadening [46, 134]. Thanks to this hBN encapsulation, we observe a multipeak feature in the PL spectra (Fig. 5.6), similar to those observed at room temperature in free-standing WS_2/WSe_2 in Ref. [72], which is an indication of the presence of moiré IX states. The high-energy (i.e. short-wavelength) exciton state gradually dominates the PL spectrum when increasing the pump level.

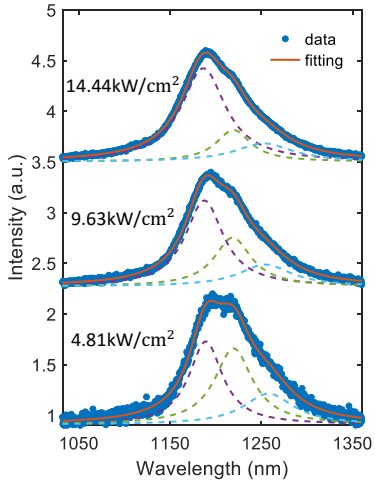

Figure 5.6. PL spectra of the hBN-encapsulated MoS_2/WSe_2 heterobilayer as a function of pump power density, taken from Ref. [116]. Experimental data (dots) are fitted with three Lorentzian functions (dashed lines).

The schematic cross-section of a device is illustrated in Fig. 5.7(a). In order to achieve good coupling between moiré IXs and the cavity mode, the bottom hBN layer is kept thinner than 10 nm. The hBN-encapsulated MoS_2/WSe_2 heterostructures were assembled and transferred to the nanocavities using the polymer-based dry-transfer method [88] (details in Chapter 2). Fig. 5.7(b) displays the spectra before and after hBN-encapsulated MoS_2/WSe_2 heterostructures transferred to the nanobeams. The presence of HS on top of the nanobeam leads to a redshift of cavity mode around 10 nm, which should be considered when selecting a desired cavity.

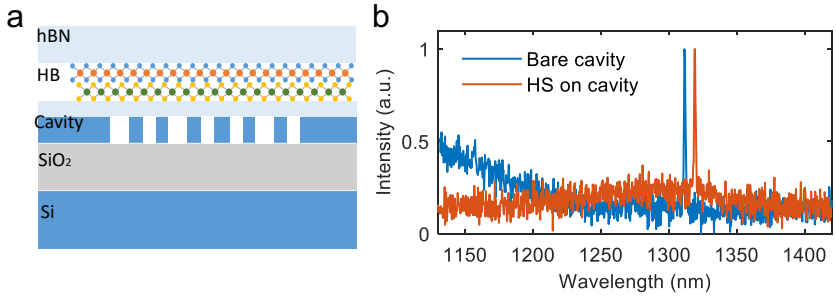

Figure 5.7. (a) Schematic cross-section of the hBN-encapsulated MoS_2/WSe_2 heterobilayer integrated with a SiO_2-supported silicon topological nanobeam cavity, taken from Ref. [116]. (b) Spectra before (blue) and after (red) hBN-encapsulated MoS_2/WSe_2 heterostructures transferred to the nanobeams, showing a resonance red-shift of around 10 nm.

5.3.1 Device 1

As mentioned in Chapter 4, the presence of moiré potentials extends the light emission of IX to the OFC O-band, which is essential for high-speed data transmission and other applications. By coupling the deeply trapped IX to the cavity mode at O-band, we observe a pronounced sharp emission line at ∼1321 nm (Fig. 5.8(a)) under optical pumping by a CW 637nm laser in a device that we denote as Device 1. The optical microscope image of Device 1 is shown in the inset of Fig. 5.8(a). Spectra evolution of Device 1 as a function of excitation power is shown in Fig. 5.8(c). We observe only a single mode dominating the spectrum throughout the pumping range, thus confirming that the topological nanobeam indeed has a large bandwidth with only a single cavity mode.

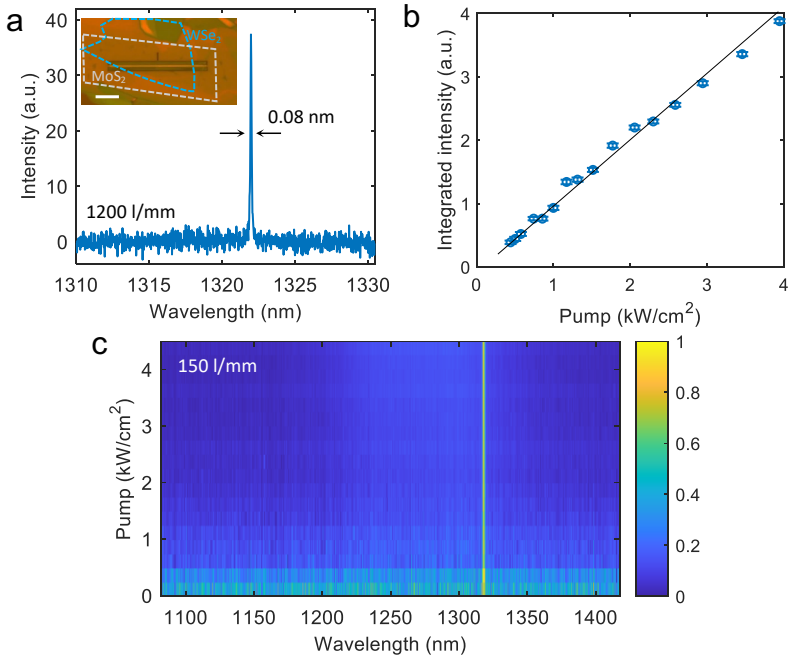

Figure 5.8. Charactrization of Device 1. (a) The emission spectrum of Device 1 at an excitation power intensity of ∼4.39 kW/cm^2. Inset: Optical microscope image of the device. The blue and grey dashed boxes outline the monolayer WSe_2 and MoS_2 areas. The top and bottom hBN layers are not shown. Scale bar, 5 µm. (b) Integrated intensity of the output of Device 1 as a function of pump intensity. (c) Spectra of Device 1 as a function of excitation power density.

The measured emission peaks are fitted to a Lorentz function and extracted a narrow linewidth of ∼0.08 nm, which is the highest spectral purity compared to all of

the reported 2D material lasers (see the comparison table in Table 5.2). It should be noted that the measured linewidth of ∼0.1 nm is limited by the spectral limit of our spectrometer with a high-resolution grating of 1200 lines/mm. This narrow linewidth corresponds to a coherence time of ∼45 ps [1], 26 times longer than the previously reported IX laser (1.7 ps) [14], thus giving strong evidence for highly coherent light emission, such as lasing.

Interestingly, we find that the output intensity of the lasing-like mode increases linearly with pump intensity (Fig. 5.8(b). The laser-like mode keeps dominating the emission spectrum from the lowest excitation power where the emission line can be distinguished. Regarding the high spectral purity and the threshold-less feature in light in-light out (L-L) curve, we suspect it could be an ultra-low-threshold laser thanks to the moiré effect.

5.3.2 Device 2

To reveal whether Device 1 lases or not, we fabricate another device (Device 2) where the cavity resonance (1168 nm) is mainly coupled to high-energy moiré IXs, as shown in Fig. 5.9(a). Compared to the low-energy moiré IX, the high-energy state is less localized, as the effective potential for the high-energy IXs becomes shallower. We expect to observe a clear lasing behaviour in Device 2, similar to the previously reported IX lasing at 1128 nm based on the same heterobilayer coupled to L3 photonic crystal cavity [14].

We carry out the pump power-dependent measurement for Device 2 and find that the cavity mode starts to dominate the emission spectrum at high pump levels. Fig. 5.9(d) shows the integrated intensity, linewidth, and peak position as a function of pump power density. The threshold region is highlighted by the light red shaded area. The L-L curve presents a super-linear behaviour, which is a typical signature of lasing.

[1]The coherence time was estimated by the formula [135]: $\tau_c = \sqrt{8ln2}\lambda^2/(c\Delta\lambda)$, where λ is the wavelength, $\Delta\lambda$ is the spectral linewidth.

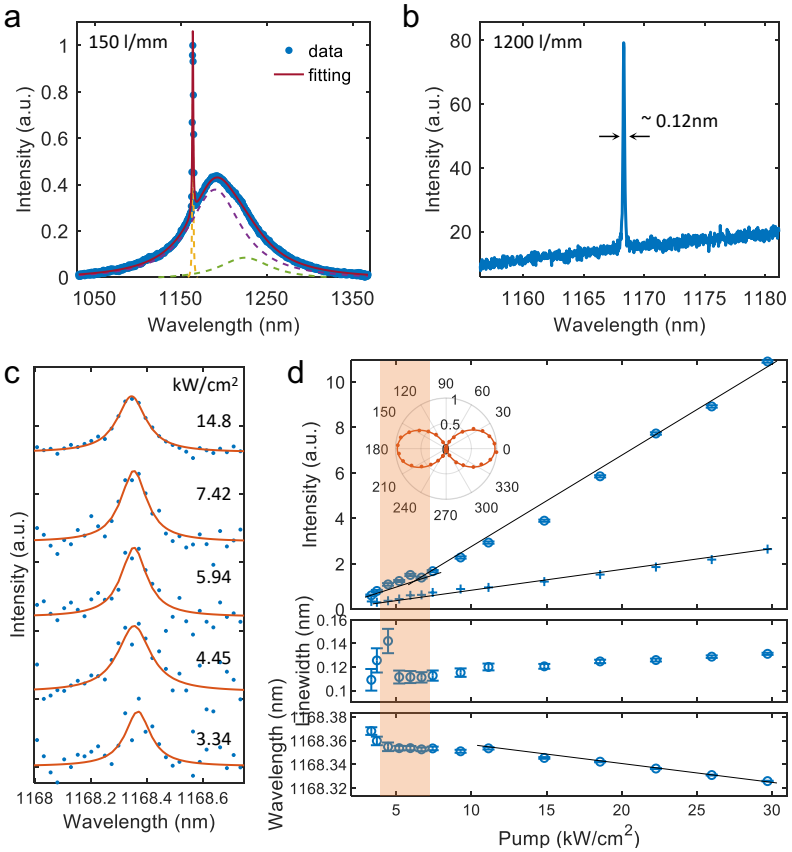

Figure 5.9. Output performance of Device 2. (a) PL spectra of Device 2 under a 150 lines/mm grating at 18.12 kW/cm^2. The dots are the measured data. The lines represent the Lorentz fittings. (b) PL spectra under a 1200 lines/mm grating. (c) PL spectra under different pump power excitation. The Lorentz fit (red curves) to the lasing-like mode agrees well with experimental data (dots). (d) Integrated intensity, linewidth, and wavelength of the output of Device 2 as a function of pump intensity. The experimental data are fitted by a Lorentzian function, and the error bars correspond to the 95% confidence interval of the Lorentzian fit. The threshold region is highlighted by the light red shaded area. The inset shows Linear polarization of the emitted mode characterized by polarization-resolved measurements, taken from Ref. [116].

Additionally, a linewidth narrowing is observed near a threshold of ∼5 kW/cm^2, suggesting a potential phase transition from thermal to coherent emission. Below the threshold, we observe an increase in linewidth and obtain a Q-factor of the unpumped HS-coupled cavity around 10^4, which is on the same order of magnitude as our simulation result for the bare silicon cavity (see Table 5.1). We explain the small effect on the Q-factor by the negligible absorption loss of IXs, two or three

orders of magnitude smaller than that of intralayer exciton. A common semiconductor gain medium is a direct bandgap material, which exhibits strong absorption before the material becomes transparent, significantly reducing the Q-factor of the cavity. Thus, the laser only undergoes linewidth decreasing with the pump level increasing. This linewidth broadening phenomenon has also been observed in indirect bandgap transition lasing [136], where the 50-nm-thick WS_2 serves as a low-absorption gain medium. The low absorption of IX combined with the high-Q cavity gives us the challenge of resolving the lasing transition by linewidth. On the other hand, the low-loss system would enable us to reach the threshold condition with a relatively small optical gain.

When pumping at higher levels (> 10 kW/cm^2), the laser-like mode is blueshifted and accompanied by linewidth broadening (the bottom panel of Fig. 5.9(d)), which can be explained by free-carrier absorption in the silicon cavity [137]. Our device barely suffers from pumping-induced heating as observed in previous works [11, 12], thanks to the supported cavity design and hBN encapsulation which enables efficient thermal energy dissipation [138].

We emphasize that the measured lasing-like emission is reproducible and can be observed via a lower-density grating. We perform the power-dependent PL measurements under a groove grating density of 150 (Fig. 5.10(a)) and 600 lines/mm (Fig. 5.10(b)). Both of them show a super-linear behaviour in the L-L curves around 5 kW/cm^2, similar to the measured threshold via the high-resolution gratings of 1200 lines/mm. Owing to the low spectral resolution of the 150 lines/mm grating, no distinct change in linewidth and energy shift is observed. The 600 lines/mm grating exhibits a broadening and reduction of the linewidth near the threshold, as well as a blue-shift of lasing-like mode at high pumping levels, exactly like the 1200 lines/mm grating.

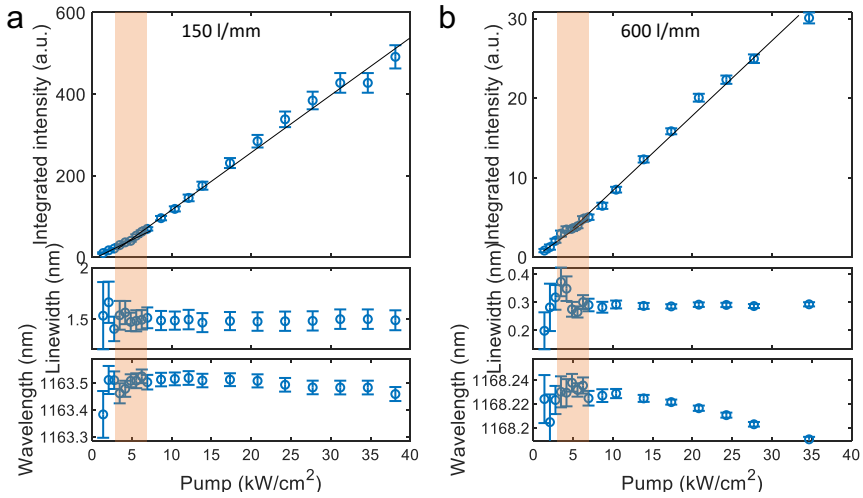

Figure 5.10. Reproducibility of power-dependent PL measurements performed under a grating density of (a) 150 and (b) 600 lines/mm.

Furthermore, the device exhibits excellent linear polarization with a degree of polarization [2] of ∼0.94 of the emission line (Fig. 5.9(d)), showing the efficient coupling between moiré IX and cavity mode. These observations indicate the occurrence of a lasing-like emission in Device 2 and the presence of efficient moiré excitonic gain within our low-loss system. And we believe that despite the linear L-L curve, Device 1 has a large probability of being a laser due to its exceptional performance. Further details regarding this will be discussed in the following section.

In this study, we describe the emission behaviour of our devices as lasing-like emission rather than lasing because the conclusive evidence from second-order coherence transitions [139] is absent. Performing such a measurement requires highly sensitive detectors. We are not able to detect the filtered signal from the lasing-like mode via the SPD (ID220-FR-MMF from IDQ).

[2]The degree of polarization is defined as $(I_{\max} - I_{\min})/(I_{\max} + I_{\min})$, where $I_{\max}$ ($I_{\min}$) is the maximum (minimum) output intensity.

5.3.3 Comparison: Coupling to different moiré IX states

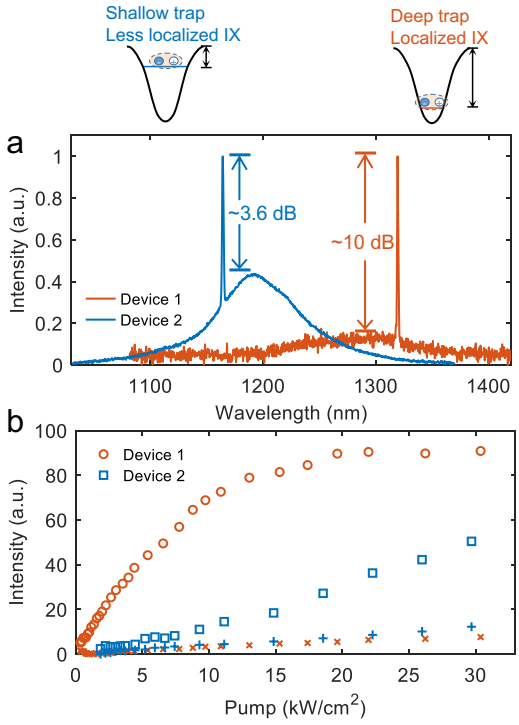

Figure 5.11. (a) Two types of lasing operation: Device 1 (with localized moiré IX) and Device 2 (with less localized moiré IX) at an excitation power intensity of ∼4.04 kW/cm^2 and ∼18.12 kW/cm^2 respectively. The black lines indicate the effective moiré potential depth. taken from Ref. [116]. (b) Output behaviour of two devices. The hollow circles/squares (plusses + and crosses x) represents the lasing-like emission (spontaneous emission). taken from Ref. [116].

For comparison, we put the data from the two devices together in Fig. 5.11.

Fig. 5.11(a) shows normalized PL spectra from Device 1 and Device 2 at an excitation power intensity of ∼4.04 kW/cm^2 and ∼18.12 kW/cm^2, respectively. Device 2 features a lasing-like emission on top of a strong spontaneous emission (SE) background, whereas Device 1 shows a significantly weaker background. Here, we propose the definition of the spontaneous-emission suppression ratio (SESR) instead of the commonly used single-mode suppression ratio (SMSR). Most of the reported TMD-based lasers operate at multi-mode, which can result in a small value of SMSR. To ensure a fair comparison, we only consider the strongest lasing mode and compare it with the most robust SE, as illustrated in the blue arrows in Fig. 5.11(a). To obtain

the SESR data from other works, we assume that the spectrum presented in a paper represents the optimal scenario. Therefore, we can determine the corresponding SESR by measuring the data from the main figure, and list it in Table 5.2.

Device 2 exhibits a SESR of ∼3.6 dB, aligning with the typical value (∼3-4 dB) for 2D material lasers. Ref. [11] explains that the strong SE background mainly originates from the TMD material far from the nanobeam cavity, which is not coupled to the cavity modes.

On the other hand, Device 1 demonstrates an impressive SESR of approximately 10 dB, similar to the SESR values achieved by vertical-cavity surface-emitting lasers (VCSEL) [82], where monolayer WS_2 embedded in distributed Bragg reflectors. We emphasize that the real SESR value could even be higher as the SE outside the nanobeam cavity is also collected [11]. We ascribe the significant difference between these two devices to a relatively larger optical gain of the low-energy moiré IX states, as a consequence of different thresholds. The connection between lasing threshold and optical gain can be described by this formula [12]:

$$\frac{2\pi n_{\text{eff}}}{\lambda}\frac{1}{Q} = \Gamma g_{\text{th}}, \tag{5.1}$$

where the left (right) term represents the loss (gain) of the system, Q is the cavity quality factor, n_{eff} is the effective refractive index for the cavity mode, λ is the cavity resonance wavelength, Γ is the optical confinement factor which characterizes the fraction of optical mode confined in the gain medium, and g_{th} is the threshold material gain. The relatively larger material gain at low pump levels will make it easier to compensate for the system loss and achieve low-threshold lasing.

The atomically thin layer restricts the motion of excitons to two dimensions, strongly increasing exciton binding energy. The presence of moiré potentials further confines the exciton within the plane dimensions, leading to discrete energy levels. Device 1 is coupled to the low-energy IX state, which is trapped in real space by deep moiré potential, whereas Device 2 is coupled to the high-energy moiré IX state which is less localized, as illustrated in Fig. 5.11(a). The strong confinement results in a high gain at low excitation power. It can also be evidenced by the output intensity of Device 1 with a larger slope efficiency than Device 2, as shown in Fig. 5.11(b). We note that our devices exhibit output saturation. We observe that Device 1 shows saturation at a much lower pumping level compared to Device 2, consistent with their confinement characteristics.

Device 3

In order to provide further evidence of the 'ultra-low-threshold' characteristics of Device 1, we demonstrate the case when the IX is coupled to a cavity mode with resonance wavelength at ∼1286 nm (Device 3), see Fig. 5.12(a), where we observe a lasing-like emission at a low threshold. The pump power-dependent measurement of Device 3 is carried out using the grating with 600 and 1200 lines/mm, and the results are presented in Fig. 5.12(c) and (d), respectively. Both results show a distinct kink

in the L-L curves and linewidth narrowing at a threshold as low as ∼0.25 kW/cm^2, suggesting a lasing-like emission from Device 3.

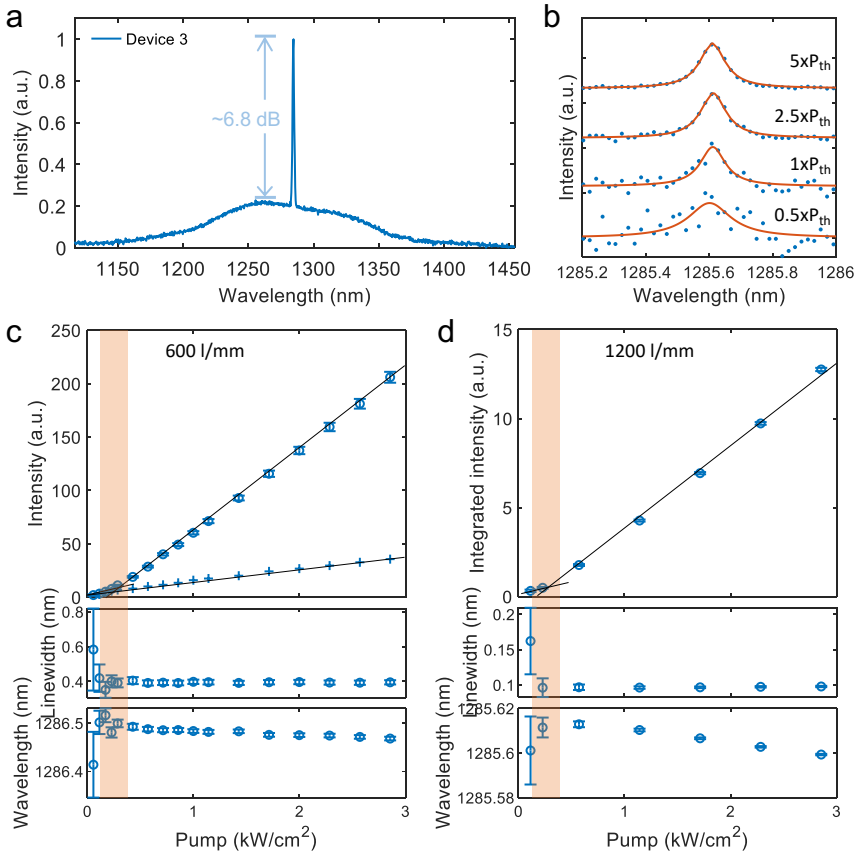

Figure 5.12. Low-threshold lasing-like emission from Device 3. (a) PL spectrum of Device 3 at an excitation power of ∼ 1.43 kW/cm^2. (b) PL spectra at various pump levels measured with a groove density of 1200 lines/mm. Experimental data (dots) are analyzed by the Lorentz fitting (red curves). Power-dependent PL measurements were performed using a grating with a density of 600 lines/mm (c) and 1200 lines/mm (d). The black lines are a guide to the eye. The threshold region is highlighted by the light red shaded area, showing a lasing threshold of ∼ 0.25 kW/cm^2. Such a low threshold further proves that Device 1 has an instrument-limited low threshold.

Similar to Device 1 and Device 2, Device 3 also reaches the spectral resolution limit of our setup and exhibits a narrow linewidth of ∼0.1 nm, showing a strong spectral coherence. And we also observe a reduction of linewidth in Device 3. In contrast to Device 2, we did not observe a linewidth increase in Device 3 before the

threshold. Fig. 5.12(b) displays the Lorentz fit to the lasing-like mode measured via 1200 lines/mm before and after the threshold. It clearly shows that the signal before the threshold is very weak, leading to increased uncertainty in both the linewidth and center wavelength. For a low pump level, the signal becomes excessively weak and gets overwhelmed by noise, so we are unable to extract the fitting data. Compared to Device 2 and Device 3, we believe that Device 1 is also lasing-like emission with a threshold that is so low that it cannot be distinguished in our measurement.

In addition, Device 3 exhibits a SESR value of 6.8 dB, falling within the range between Device 1 and Device 2. This observation further confirms our earlier proposition of a larger optical gain in the localized moiré IX states than the delocalized one.

5.4 Summary

In this chapter, we integrate moiré superlattices with single-mode silicon topological photonic crystal nanocavities and study the impact of moiré superlattices on laser performance. To the best of our knowledge, we, for the first time, explore the potential of room-temperature moiré IX for high-performance laser applications. We demonstrate a broad gain spectrum over 150 nm from moiré IXs. We find the deep localized moiré IX has a larger optical gain in comparison to its less-localized counterpart, resulting in a reduction in the threshold and an enhanced spontaneous-emission suppression ratio (SESR). Through the combination of a Q-factor cavity and deep-localized moiré IX states, we have successfully demonstrated lasing-like emission in an operation wavelength (1321 nm) extended to the O-band of optical fiber communication (1260-1360nm). Furthermore, our demonstration attains the highest spectral coherence among TMD-based lasers [140] (Table 5.2) and exhibits a high SESR of 10 dB and possibly a threshold of less than 0.25 kW/cm^2. We expect that the lasing threshold can be significantly reduced by increasing the Γ, for example, embedding the gain material into the cavity [82]. Furthermore, our findings encourage studying novel exciton physics in moiré superlattices at room temperature and open new avenues for using these artificial quantum materials in high-performance device applications.

Lasing-like emission

Once again, we emphasize that we are referring to 'lasing-like emission' instead of 'lasing'. This is due to the lack of conclusive evidence, i.e., the second-order autocorrelation function $g^{(2)}(0)$ transition process from 2 to 1. Unfortunately, the weak signal from the samples and inadequate detector sensitivity hinder us to conduct the photon correlation measurement.

Small linewidth reduction

Linewidth narrowing is a conventional signature of the onset of lasing. In general, the linewidth tends to decrease by half when lasing occurs [141].

In our work, we show a minor linewidth decrease around the threshold from 0.14 to 0.11 nm for Device 2 and from 0.15 to 0.1 nm for Device 3. Such subtle changes in linewidth are commonly observed in high-β TMD-nanolasers [12–14, 80, 142]. For example, Xiang Zhang's group reported an excitonic laser using monolayer WS_2 coupled to a microdisk [80] and observed a linewidth reduction from 0.28 to 0.24 nm.

Stephan Reitzenstein's group also observed a minor linewidth narrowing from 0.21 to 0.19 nm [143] in high-β lasers, and the onset of lasing is confirmed by excitation-dependent second-order autocorrelation measurements. They pointed out that power-dependent linewidth narrowing cannot be a criterion for lasing in high-β lasers, as it could be caused by quenching of absorption losses [143].

Advanced model

Many studies on TMD nanolasers use the laser rate equation model to fit the L-L curve. However, we did not employ rate equation fitting for mainly two reasons. Firstly, coherence and statistical properties cannot be captured using the rate equation modeling [143]. Secondly, the rate equations do not take into account the excitonic effect and non-radiative loss [82].

One may notice Device 2 shows an unfamiliar inverse S-shape in the L-L curve. This phenomenon has also been experimentally observed in WS_2-based VCSELs [82]. Stephan Reitzenstein's group has systematically studied high-β nanolasers and reported the emergence of an inverse S-shape at 90 K in an III-nitride QW nanobeam system [143]. When the temperature increased to 156 K, the L-L curve became linear. They ascribed this inversely S-shaped L-L curve likely to the presence of a zero-dimensional localized state, providing larger gain compared to 2D gain materials until it is saturated. Their microscopic model is not able to reproduce the inverse S-shape, even though it takes into account the light-matter coupling strength and non-radiative losses.

In all, a comprehensive description of the moiré IX lasing behaviour requires a sophisticated model that incorporates various factors such as the gain contribution from various moiré IX states, excitonic effect and non-radiative losses. Currently, the gain mechanisms in the moiré IX remain to be understood. Our research findings stimulate further investigations into the theory for moiré exciton lasing with experimental data support.

Table 5.2. Comparison of TMD-based lasers. The symbol '-' means that no corresponding data are reported. The value marked with '*' are calculated according to the data shown in the paper.

Ref.	Material	Cavity	Temperature	Wavelength (nm)	Linewidth (nm)	Q factor	Threshold (kW/cm^2)	SMSR (dB)
[79]	WSe_2	GaP L3 PhCC	80K 130K	739.7 @80K	0.3 @80K 0.5 @160K	2465* @80K	$\sim 1\times10^{-3}$ @130K	-
[144]	WSe_2	silica microspheres	RT	806.7	4.58	~200	0.72×10^{-3}	3.61*
[80]	WS_2	Si_3N_4 microdisk + HSQ	10K	612.2	0.24	2604	$\sim 5–8\times10^{3}$	4.26*
[82]	WS_2	SiO_2/TiO_2 DBR	RT	636.5	~0.72	~900	0.44×10^{-3}	10.40*
[145]	WS_2	Si_3N_4 PhC (BIC)	RT	637	0.25	2500	$89\text{-}144\times10^{-3}$	5.10*
[136]	WS_2	WS_2 disk	RT	~869	1.48	587*	1.25	2.29*
[142]	$MoSe_2$	SiO_2 microsphere	RT	~750-875	5-1.25	154-770	$215\text{-}107\times10^{-3}$	3.23*
[81]	MoS_2	SiO_2 microdisk + SiO_2 microsphere	RT	~600-800	0.26	1900-3300	~7.14*	3.54*
[146]	MoS_2	SiO_2 microsphere	77-400K	650-690	0.3-2.5	400-1900	$32\text{-}580\times10^{-3}$	5.19*
[11]	$MoTe_2$	Si nanobeam	RT	1132.25	0.202	5603	$\sim 6.6\times10^{-3}$ 2.10*	3.78*
[12]	$MoTe_2$	Si L3 PhCC	RT	1305	0.49	2660	~1.5	10.52*
[13]	$MoTe_2$	Si nanobeam	RT	1319	0.294	4486	~4.2	0.39*
[14]	MoS_2/ WSe_2	Si L3 PhCC	RT	1128	~2.15	524	~6.88*	4.02*
[15]	WSe_2/ $MoSe_2$	Si_3N_4 grating	5K	918.5	1.359	630	~0.409*	-
This work	MoS_2/ WSe_2	Si nanobeam	RT	1321.6	~0.08	>10000	<0.25	10.31

Conclusion and Outlook

In this thesis, we focus on exploring the existence of room-temperature moiré excitons through the fabrication of high-quality MoS_2/WSe_2 heterobilayers and investigate their potential as gain media in lasing when combined with high-Q microcavities.

The key highlights of this thesis are as follows:

Firstly, we have built a deterministic 2D material transfer system and successfully prepared high-quality heterobilayers. Relying on previous recipes in Nanolab, we have also developed a fabrication process for high-Q cavities.

Secondly, we have repaired an outdated spectrometer and built a multi-functional near-infrared optical testing platform, which provides a solid foundation for our investigation of room-temperature moiré excitons and their interactions with the cavities.

Thirdly, we report, for the first time, the evidence of room-temperature moiré excitons in MoS_2/WSe_2 heterobilayers and their impacts on light emission utilizing the optical setup we constructed. We find that the moiré potential gives rise to an ultra-wide emission tunability of IXs and extends IX lifetime at RT.

Fourthly, by integrating a moiré superlattice with a silicon topological nanocavity, we demonstrat low-threshold laser-like emission at the technologically important telecommunication O-band and the highest spectral coherence (< 0.1 nm) compared to all reported two-dimensional material-based lasers.

We believe that our findings, both from a fundamental and applied perspective, set the grounds for the study of quantum phenomena in 2D systems and their applications at elevated temperatures. It will be of high interest to the broad community covering optics, nanoscience, material, and physics, and therefore will open up new activities in this very topical area.

There are still numerous interesting topics that have not been explored or have been explored in any depth so far, waiting for further investigation. Among the many exciting possibilities, several relevant ones are highlighted below.

Direct evidence of moiré exciton

Currently, numerous articles have reported the observation of moiré excitons through optical spectroscopy [46, 48, 63, 64]. It provides indirect evidence of the confinement of excitons in real space through optical features such as spectrum splitting, and valley-polarized PL that align with theoretical calculations. Nanoscale

confinement has been investigated using angle-resolved photoemission spectroscopy (ARPES) [52, 68] and transmission electron microscopy low-loss electron energy-loss spectroscopy (STEM-EELS) [70]. However, these methods reconstruct the wavefunction distribution of the electronic component of the exciton rather than directly probing the exciton itself. Therefore, there is a need for future direct observations of excitons confined in periodic moiré patterns using high spatial resolution spectroscopy such as near-field techniques. This will eliminate the dominant exciton trapping mechanism arising from external sources such as extrinsic traps or defects and give opportunities to study moiré exciton physics for quantum technology.

Gain mechanism

In addition to van der Waals heterobilayers, various active 2D materials have been investigated for low-threshold lasing applications, including monolayer TMD and multilayer TMDs [136]. And more recently, it was demonstrated that combining TMD with cadmium selenide (CdSe) quantum dots is beneficial for low-threshold lasing [147].

There are different perspectives regarding the origin of optical gain in 2D materials. Some argue that the gain arises from the contribution of the stimulated emission of electron-hole plasma above the Mott transition [148], while others contend that the gain originates from excitons [80, 149]. Cunzheng Ning's group [150] reported the observation of optical gain from charged excitons (so-called trions) in gated $MoTe_2$ at low carrier density levels, orders of magnitudes below the Mott density. They mentioned that the trion gain could exist at any arbitrarily low carrier density level, which could lead to extremely low-threshold lasers down to the single charge level.

Despite the significant progress made thus far, there is limited understanding of the fundamental mechanism for achieving lasing in TMDs materials. For instance, a direct measurement of the optical gain in IX is crucial for further advancements in low-power consumption nanolasers. Because these lasers exhibit exceptional energy efficiency with a wide range of applications in today's data-driven world, such as low-power optical communications, optical interconnects, optoelectronic integration, quantum information processing, and sensing systems.

Lasing confirmation

Many studies have demonstrated TMD-based lasers by combining two-dimensional materials with various photonic cavities, primarily through the observation of super-linear L-L curves and linewidth narrowing around the lasing threshold. However, whether the system operates in a lasing regime or not remains a subject of controversy [151]. Reports show that similar phenomena in the L-L curve and linewidth can occur in LEDs and amplified spontaneous emission (ASE) [139], thereby making it an inconclusive criterion for lasing. In addition, first-order coherence cannot be used as a criterion for identifying lasers as it depends on the linewidth. To confirm lasing, it is necessary to measure the second-order photon auto-correlation function $g^2(\tau)$ which reflects photon statistics. For instance, when $g^2(0)$ reduces from 2 to 1 in a standard laser, the photon statistics undergoes a transition from a super-Poissonian to Poissonian distribution, i.e., a transition from thermal light to coherent light.

In Our TMD-based devices, the measurement of $g^2(\tau)$ is challenging due to the low threshold and weak emission of these 2D systems. We tried to measure $g^2(\tau)$ using a Hanbury Brown and Twiss setup, but the count rates were too low. Highly sensitive photon detectors like superconducting detectors could be helpful. Recently, the second-order photon auto-correlations above and below a threshold have been measured [136, 147], but the evolution of $g^2(\tau)$ around threshold in TMD nanolasers is still lacking.

Large-scale TMD fabrication

In this thesis, we use the mechanical exfoliation method to obtain monolayer TMDs. The optical quality of the exfoliated monolayer depends on the quality of the bulk crystal. The typical defect density of CVT-grown crystals is on the order of $\sim 10^{13}/\mathrm{cm}^2$, while flux-grown crystals exhibit a lower defect density by 1-2 orders of magnitude, around $\sim 10^{11}/\mathrm{cm}^2$ [83]. The quantum yield of the exfoliated monolayer can be further enhanced by employing chemical treatments to eliminate defect-mediated non-radiative recombination [128].

Despite the low cost and high optical quality of atomically thin layers achieved through the exfoliation method, it suffers from limited size, low yields, and time-consuming procedures. Furthermore, the implementation of stacked heterostructures exacerbates the challenges by further reducing the yield and available area, accompanied by various uncertainties arising from experimental procedures.

For future applications, it is imperative to seek more efficient growth methods for obtaining large-size, high-quality atomical-thin 2D materials. In this year (2023), MIT [152] has developed a method that enables the growth of defect-free monolayer WSe_2 on industrial silicon wafers. The grown monolayer has a defect density of $\sim 10^{13}/\mathrm{cm}^2$, approaching the quality level of mechanically exfoliated WSe_2 flakes. They have also demonstrated layer-by-layer growth of large-scale MoS_2/WSe_2 heterostructures. We are optimistic about the integration of these semiconducting 2D materials into industrial platforms and anticipate the extensive utilization of 2D materials in the near future.

Bibliography

[1] A. Rickman, "The commercialization of silicon photonics," *Nature Photonics*, vol. 8, no. 8, pp. 579–582, 2014.

[2] D. Liang and J. E. Bowers, "Recent progress in lasers on silicon," *Nature Photonics*, vol. 4, no. 8, pp. 511–517, 2010.

[3] K. Hirschman, L. Tsybeskov, S. Duttagupta, and P. Fauchet, "Silicon-based visible light-emitting devices integrated into microelectronic circuits," *Nature*, vol. 384, no. 6607, pp. 338–341, 1996.

[4] L. Pavesi, L. Dal Negro, C. Mazzoleni, G. Franzo, and d. F. Priolo, "Optical gain in silicon nanocrystals," *Nature*, vol. 408, no. 6811, pp. 440–444, 2000.

[5] S. Chen, W. Li, J. Wu, Q. Jiang, M. Tang, S. Shutts, S. N. Elliott, A. Sobiesierski, A. J. Seeds, I. Ross, *et al.*, "Electrically pumped continuous-wave III-V quantum dot lasers on silicon," *Nature Photonics*, vol. 10, no. 5, pp. 307–311, 2016.

[6] D. Liang, X. Huang, G. Kurczveil, M. Fiorentino, and R. Beausoleil, "Integrated finely tunable microring laser on silicon," *Nature Photonics*, vol. 10, no. 11, pp. 719–722, 2016.

[7] K. F. Mak and J. Shan, "Photonics and optoelectronics of 2D semiconductor transition metal dichalcogenides," *Nature Photonics*, vol. 10, no. 4, pp. 216–226, 2016.

[8] M.-Y. Li, S.-K. Su, H.-S. P. Wong, and L.-J. Li, "How 2D semiconductors could extend Moore's law," *Nature*, vol. 567, no. 7747, pp. 169–170, 2019.

[9] L. Zhao, Q. Shang, M. Li, Y. Liang, C. Li, and Q. Zhang, "Strong exciton-photon interaction and lasing of two-dimensional transition metal dichalcogenide semiconductors," *Nano Research*, vol. 14, no. 6, pp. 1937–1954, 2021.

[10] J. Pu and T. Takenobu, "Monolayer transition metal dichalcogenides as light sources," *Advanced Materials*, vol. 30, no. 33, p. 1707627, 2018.

[11] Y. Li, J. Zhang, D. Huang, H. Sun, F. Fan, J. Feng, Z. Wang, and C.-Z. Ning, "Room-temperature continuous-wave lasing from monolayer molybdenum ditelluride integrated with a silicon nanobeam cavity," *Nature Nanotechnology*, vol. 12, no. 10, pp. 987–992, 2017.

[12] H. Fang, J. Liu, H. Li, L. Zhou, L. Liu, J. Li, X. Wang, T. F. Krauss, and Y. Wang, "1305 nm few-layer $MoTe_2$-on-silicon laser-like emission," *Laser & Photonics Reviews*, vol. 12, no. 6, p. 1800015, 2018.

[13] H. Fang, J. Liu, Q. Lin, R. Su, Y. Wei, T. F. Krauss, J. Li, Y. Wang, and X. Wang, "Laser-like emission from a sandwiched $MoTe_2$ heterostructure on a silicon single-mode resonator," *Advanced Optical Materials*, vol. 7, no. 20, p. 1900538, 2019.

[14] Y. Liu, H. Fang, A. Rasmita, Y. Zhou, J. Li, T. Yu, Q. Xiong, N. Zheludev, J. Liu, and W. Gao, "Room temperature nanocavity laser with interlayer excitons in 2D heterostructures," *Science Advances*, vol. 5, no. 4, p. eaav4506, 2019.

[15] E. Y. Paik, L. Zhang, G. W. Burg, R. Gogna, E. Tutuc, and H. Deng, "Interlayer exciton laser of extended spatial coherence in atomically thin heterostructures," *Nature*, vol. 576, no. 7785, pp. 80–84, 2019.

[16] N. N. Ledentsov, M. Grundmann, F. Heinrichsdorff, D. Bimberg, V. Ustinov, A. Zhukov, M. Maximov, Z. I. Alferov, and J. Lott, "Quantum-dot heterostructure lasers," *IEEE Journal of Selected Topics in Quantum Electronics*, vol. 6, no. 3, pp. 439–451, 2000.

[17] X. Chia, A. Y. S. Eng, A. Ambrosi, S. M. Tan, and M. Pumera, "Electrochemistry of nanostructured layered transition-metal dichalcogenides," *Chemical reviews*, vol. 115, no. 21, pp. 11941–11966, 2015.

[18] Q. H. Wang, K. Kalantar-Zadeh, A. Kis, J. N. Coleman, and M. S. Strano, "Electronics and optoelectronics of two-dimensional transition metal dichalcogenides," *Nature Nanotechnology*, vol. 7, no. 11, pp. 699–712, 2012.

[19] A. Splendiani, L. Sun, Y. Zhang, T. Li, J. Kim, C.-Y. Chim, G. Galli, and F. Wang, "Emerging photoluminescence in monolayer MoS_2," *Nano Letters*, vol. 10, no. 4, pp. 1271–1275, 2010.

[20] K. F. Mak, C. Lee, J. Hone, J. Shan, and T. F. Heinz, "Atomically thin MoS_2: a new direct-gap semiconductor," *Physical Review Letters*, vol. 105, no. 13, p. 136805, 2010.

[21] G.-B. Liu, W.-Y. Shan, Y. Yao, W. Yao, and D. Xiao, "Three-band tight-binding model for monolayers of group-VIB transition metal dichalcogenides," *Physical Review B*, vol. 88, no. 8, p. 085433, 2013.

[22] W. Jin, P.-C. Yeh, N. Zaki, D. Zhang, J. T. Sadowski, A. Al-Mahboob, A. M. van Der Zande, D. A. Chenet, J. I. Dadap, I. P. Herman, *et al.*, "Direct measurement of the thickness-dependent electronic band structure of MoS_2 using angle-resolved photoemission spectroscopy," *Physical Review Letters*, vol. 111, no. 10, p. 106801, 2013.

[23] Y. Zhang, T.-R. Chang, B. Zhou, Y.-T. Cui, H. Yan, Z. Liu, F. Schmitt, J. Lee, R. Moore, Y. Chen, *et al.*, "Direct observation of the transition from indirect to direct bandgap in atomically thin epitaxial $MoSe_2$," *Nature Nanotechnology*, vol. 9, no. 2, pp. 111–115, 2014.

[24] A. Kormányos, G. Burkard, M. Gmitra, J. Fabian, V. Zólyomi, N. D. Drummond, and V. Fal'ko, "k · p theory for two-dimensional transition metal dichalcogenide semiconductors," *2D Materials*, vol. 2, no. 2, p. 022001, 2015.

[25] X. Xu, W. Yao, D. Xiao, and T. F. Heinz, "Spin and pseudospins in layered transition metal dichalcogenides," *Nature Physics*, vol. 10, no. 5, pp. 343–350, 2014.

[26] J. R. Schaibley, H. Yu, G. Clark, P. Rivera, J. S. Ross, K. L. Seyler, W. Yao, and X. Xu, "Valleytronics in 2D materials," *Nature Reviews Materials*, vol. 1, no. 11, pp. 1–15, 2016.

[27] G. Wang, A. Chernikov, M. M. Glazov, T. F. Heinz, X. Marie, T. Amand, and B. Urbaszek, "Colloquium: Excitons in atomically thin transition metal dichalcogenides," *Reviews of Modern Physics*, vol. 90, no. 2, p. 021001, 2018.

[28] I. Pelant and J. Valenta, *Luminescence spectroscopy of semiconductors*. OUP Oxford, 2012.

[29] A. Raja, A. Chaves, J. Yu, G. Arefe, H. M. Hill, A. F. Rigosi, T. C. Berkelbach, P. Nagler, C. Schüller, T. Korn, *et al.*, "Coulomb engineering of the bandgap and excitons in two-dimensional materials," *Nature Communications*, vol. 8, no. 1, p. 15251, 2017.

[30] R. Miller and D. Kleinman, "Excitons in GaAs quantum wells," *Journal of Luminescence*, vol. 30, no. 1-4, pp. 520–540, 1985.

[31] A. Chernikov, T. C. Berkelbach, H. M. Hill, A. Rigosi, Y. Li, B. Aslan, D. R. Reichman, M. S. Hybertsen, and T. F. Heinz, "Exciton binding energy and nonhydrogenic Rydberg series in monolayer WS_2," *Physical Review Letters*, vol. 113, no. 7, p. 076802, 2014.

[32] D. Kozawa, R. Kumar, A. Carvalho, K. Kumar Amara, W. Zhao, S. Wang, M. Toh, R. M. Ribeiro, A. H. Castro Neto, K. Matsuda, *et al.*, "Photocarrier relaxation pathway in two-dimensional semiconducting transition metal dichalcogenides," *Nature Communications*, vol. 5, no. 1, p. 4543, 2014.

[33] K. F. Mak, K. He, J. Shan, and T. F. Heinz, "Control of valley polarization in monolayer MoS_2 by optical helicity," *Nature Nanotechnology*, vol. 7, no. 8, pp. 494–498, 2012.

[34] H. Zeng, J. Dai, W. Yao, D. Xiao, and X. Cui, "Valley polarization in MoS_2 monolayers by optical pumping," *Nature Nanotechnology*, vol. 7, no. 8, pp. 490–493, 2012.

[35] M. Li, M. Z. Bellus, J. Dai, L. Ma, X. Li, H. Zhao, and X. C. Zeng, "A type-I van der Waals heterobilayer of $WSe_2/MoTe_2$," *Nanotechnology*, vol. 29, no. 33, p. 335203, 2018.

[36] T. Yamaoka, H. E. Lim, S. Koirala, X. Wang, K. Shinokita, M. Maruyama, S. Okada, Y. Miyauchi, and K. Matsuda, "Efficient photocarrier transfer and effective photoluminescence enhancement in type I monolayer $MoTe_2$ /WSe_2 heterostructure," *Advanced Functional Materials*, vol. 28, no. 35, p. 1801021, 2018.

[37] C. Zhang, C. Gong, Y. Nie, K.-A. Min, C. Liang, Y. J. Oh, H. Zhang, W. Wang, S. Hong, L. Colombo, *et al.*, "Systematic study of electronic structure and band alignment of monolayer transition metal dichalcogenides in van der Waals heterostructures," *2D Materials*, vol. 4, no. 1, p. 015026, 2016.

[38] Y. Wang, Z. Wang, W. Yao, G.-B. Liu, and H. Yu, "Interlayer coupling in commensurate and incommensurate bilayer structures of transition-metal dichalcogenides," *Physical Review B*, vol. 95, no. 11, p. 115429, 2017.

[39] P. Rivera, J. R. Schaibley, A. M. Jones, J. S. Ross, S. Wu, G. Aivazian, P. Klement, K. Seyler, G. Clark, N. J. Ghimire, *et al.*, "Observation of long-lived interlayer excitons in monolayer $MoSe_2$-WSe_2 heterostructures," *Nature Communications*, vol. 6, no. 1, pp. 1–6, 2015.

[40] P. Rivera, H. Yu, K. L. Seyler, N. P. Wilson, W. Yao, and X. Xu, "Interlayer valley excitons in heterobilayers of transition metal dichalcogenides," *Nature Nanotechnology*, vol. 13, no. 11, pp. 1004–1015, 2018.

[41] E. Barré, O. Karni, E. Liu, A. L. O'Beirne, X. Chen, H. B. Ribeiro, L. Yu, B. Kim, K. Watanabe, T. Taniguchi, *et al.*, "Optical absorption of interlayer excitons in transition-metal dichalcogenide heterostructures," *Science*, vol. 376, no. 6591, pp. 406–410, 2022.

[42] H.-P. Komsa and A. V. Krasheninnikov, "Electronic structures and optical properties of realistic transition metal dichalcogenide heterostructures from first principles," *Physical Review B*, vol. 88, no. 8, p. 085318, 2013.

[43] N. R. Wilson, P. V. Nguyen, K. Seyler, P. Rivera, A. J. Marsden, Z. P. Laker, G. C. Constantinescu, V. Kandyba, A. Barinov, N. D. Hine, *et al.*, "Determination of band offsets, hybridization, and exciton binding in 2D semiconductor heterostructures," *Science Advances*, vol. 3, no. 2, p. e1601832, 2017.

[44] E. Calman, M. Fogler, L. Butov, S. Hu, A. Mishchenko, and A. Geim, "Indirect excitons in van der Waals heterostructures at room temperature," *Nature Communications*, vol. 9, no. 1, p. 1895, 2018.

[45] Z. Wang, D. A. Rhodes, K. Watanabe, T. Taniguchi, J. C. Hone, J. Shan, and K. F. Mak, "Evidence of high-temperature exciton condensation in two-dimensional atomic double layers," *Nature*, vol. 574, no. 7776, pp. 76–80, 2019.

[46] K. Tran, G. Moody, F. Wu, X. Lu, J. Choi, K. Kim, A. Rai, D. A. Sanchez, J. Quan, A. Singh, *et al.*, "Evidence for moiré excitons in van der Waals heterostructures," *Nature*, vol. 567, no. 7746, pp. 71–75, 2019.

[47] O. Karni, E. Barré, S. C. Lau, R. Gillen, E. Y. Ma, B. Kim, K. Watanabe, T. Taniguchi, J. Maultzsch, K. Barmak, *et al.*, "Infrared interlayer exciton emission in MoS_2/WSe_2 heterostructures," *Physical Review Letters*, vol. 123, no. 24, p. 247402, 2019.

[48] E. M. Alexeev, D. A. Ruiz-Tijerina, M. Danovich, M. J. Hamer, D. J. Terry, P. K. Nayak, S. Ahn, S. Pak, J. Lee, J. I. Sohn, *et al.*, "Resonantly hybridized excitons in moiré superlattices in van der Waals heterostructures," *Nature*, vol. 567, no. 7746, pp. 81–86, 2019.

[49] L. Zhang, Z. Zhang, F. Wu, D. Wang, R. Gogna, S. Hou, K. Watanabe, T. Taniguchi, K. Kulkarni, T. Kuo, *et al.*, "Twist-angle dependence of moiré excitons in $WS_2/MoSe_2$ heterobilayers," *Nature Communications*, vol. 11, no. 1, p. 5888, 2020.

[50] L. A. Jauregui, A. Y. Joe, K. Pistunova, D. S. Wild, A. A. High, Y. Zhou, G. Scuri, K. De Greve, A. Sushko, C.-H. Yu, *et al.*, "Electrical control of interlayer exciton dynamics in atomically thin heterostructures," *Science*, vol. 366, no. 6467, pp. 870–875, 2019.

[51] L. Sigl, M. Troue, M. Katzer, M. Selig, F. Sigger, J. Kiemle, M. Brotons-Gisbert, K. Watanabe, T. Taniguchi, B. D. Gerardot, *et al.*, "Optical dipole orientation of interlayer excitons in $MoSe_2$- WSe_2 heterostacks," *Physical Review B*, vol. 105, no. 3, p. 035417, 2022.

[52] O. Karni, E. Barré, V. Pareek, J. D. Georgaras, M. K. Man, C. Sahoo, D. R. Bacon, X. Zhu, H. B. Ribeiro, A. L. O'Beirne, *et al.*, "Structure of the moiré exciton captured by imaging its electron and hole," *Nature*, vol. 603, no. 7900, pp. 247–252, 2022.

[53] C. Cho, J. Wong, A. Taqieddin, S. Biswas, N. R. Aluru, S. Nam, and H. A. Atwater, "Highly strain-tunable interlayer excitons in MoS_2/WSe_2 heterobilayers," *Nano Letters*, vol. 21, no. 9, pp. 3956–3964, 2021.

[54] P. K. Nayak, Y. Horbatenko, S. Ahn, G. Kim, J.-U. Lee, K. Y. Ma, A.-R. Jang, H. Lim, D. Kim, S. Ryu, *et al.*, "Probing evolution of twist-angle-dependent interlayer excitons in $MoSe_2/WSe_2$ van der Waals heterostructures," *ACS Nano*, vol. 11, no. 4, pp. 4041–4050, 2017.

[55] S. Bertolazzi, J. Brivio, and A. Kis, "Stretching and breaking of ultrathin MoS_2," *ACS Nano*, vol. 5, no. 12, pp. 9703–9709, 2011.

[56] J. N. Coleman, M. Lotya, A. O'Neill, S. D. Bergin, P. J. King, U. Khan, K. Young, A. Gaucher, S. De, R. J. Smith, *et al.*, "Two-dimensional nanosheets produced by liquid exfoliation of layered materials," *Science*, vol. 331, no. 6017, pp. 568–571, 2011.

[57] K. Zollner, P. E. F. Junior, and J. Fabian, "Strain-tunable orbital, spin-orbit, and optical properties of monolayer transition-metal dichalcogenides," *Physical Review B*, vol. 100, no. 19, p. 195126, 2019.

[58] C. Zhang, M.-Y. Li, J. Tersoff, Y. Han, Y. Su, L.-J. Li, D. A. Muller, and C.-K. Shih, "Strain distributions and their influence on electronic structures of WSe_2–MoS_2 laterally strained heterojunctions," *Nature Nanotechnology*, vol. 13, no. 2, pp. 152–158, 2018.

[59] H. Yu, Y. Wang, Q. Tong, X. Xu, and W. Yao, "Anomalous light cones and valley optical selection rules of interlayer excitons in twisted heterobilayers," *Physical Review Letters*, vol. 115, no. 18, p. 187002, 2015.

[60] J. Choi, M. Florian, A. Steinhoff, D. Erben, K. Tran, D. S. Kim, L. Sun, J. Quan, R. Claassen, S. Majumder, *et al.*, "Twist angle-dependent interlayer exciton lifetimes in van der Waals heterostructures," *Physical Review Letters*, vol. 126, no. 4, p. 047401, 2021.

[61] F. Wu, T. Lovorn, and A. MacDonald, "Theory of optical absorption by interlayer excitons in transition metal dichalcogenide heterobilayers," *Physical Review B*, vol. 97, no. 3, p. 035306, 2018.

[62] H. Yu, G.-B. Liu, J. Tang, X. Xu, and W. Yao, "Moiré excitons: From programmable quantum emitter arrays to spin-orbit–coupled artificial lattices," *Science Advances*, vol. 3, no. 11, p. e1701696, 2017.

[63] K. L. Seyler, P. Rivera, H. Yu, N. P. Wilson, E. L. Ray, D. G. Mandrus, J. Yan, W. Yao, and X. Xu, "Signatures of moiré-trapped valley excitons in $MoSe_2/WSe_2$ heterobilayers," *Nature*, vol. 567, no. 7746, pp. 66–70, 2019.

[64] F. Mahdikhanysarvejahany, D. N. Shanks, M. Klein, Q. Wang, M. R. Koehler, D. G. Mandrus, T. Taniguchi, K. Watanabe, O. L. Monti, B. J. LeRoy, *et al.*, "Localized interlayer excitons in $MoSe_2$–WSe_2 heterostructures without a moiré potential," *Nature Communications*, vol. 13, no. 1, p. 5354, 2022.

[65] H. Baek, M. Brotons-Gisbert, Z. X. Koong, A. Campbell, M. Rambach, K. Watanabe, T. Taniguchi, and B. D. Gerardot, "Highly energy-tunable quantum light from moiré-trapped excitons," *Science Advances*, vol. 6, no. 37, p. eaba8526, 2020.

[66] C. Jin, E. C. Regan, A. Yan, M. Iqbal Bakti Utama, D. Wang, S. Zhao, Y. Qin, S. Yang, Z. Zheng, S. Shi, *et al.*, "Observation of moiré excitons in WSe_2/WS_2 heterostructure superlattices," *Nature*, vol. 567, no. 7746, pp. 76–80, 2019.

[67] F. Wu, T. Lovorn, and A. H. MacDonald, "Topological exciton bands in moiré heterojunctions," *Physical Review Letters*, vol. 118, no. 14, p. 147401, 2017.

[68] D. Schmitt, J. P. Bange, W. Bennecke, A. AlMutairi, G. Meneghini, K. Watanabe, T. Taniguchi, D. Steil, D. R. Luke, R. T. Weitz, *et al.*, "Formation of moiré interlayer excitons in space and time," *Nature*, vol. 608, no. 7923, pp. 499–503, 2022.

[69] Z. Li, X. Lu, D. F. Cordovilla Leon, Z. Lyu, H. Xie, J. Hou, Y. Lu, X. Guo, A. Kaczmarek, T. Taniguchi, *et al.*, "Interlayer exciton transport in $MoSe_2/WSe_2$ heterostructures," *ACS Nano*, vol. 15, no. 1, pp. 1539–1547, 2021.

[70] S. Susarla, M. H. Naik, D. D. Blach, J. Zipfel, T. Taniguchi, K. Watanabe, L. Huang, R. Ramesh, F. H. da Jornada, S. G. Louie, *et al.*, "Hyperspectral imaging of exciton confinement within a moiré unit cell with a subnanometer electron probe," *Science*, vol. 378, no. 6625, pp. 1235–1239, 2022.

[71] C. Zhang, C.-P. Chuu, X. Ren, M.-Y. Li, L.-J. Li, C. Jin, M.-Y. Chou, and C.-K. Shih, "Interlayer couplings, moiré patterns, and 2D electronic superlattices in MoS_2/WSe_2 hetero-bilayers," *Science Advances*, vol. 3, no. 1, p. e1601459, 2017.

[72] X. Sun, Y. Zhu, H. Qin, B. Liu, Y. Tang, T. Lü, S. Rahman, T. Yildirim, and Y. Lu, "Enhanced interactions of interlayer excitons in free-standing heterobilayers," *Nature*, vol. 610, no. 7932, pp. 478–484, 2022.

[73] H. Yoo, R. Engelke, S. Carr, S. Fang, K. Zhang, P. Cazeaux, S. H. Sung, R. Hovden, A. W. Tsen, T. Taniguchi, *et al.*, "Atomic and electronic reconstruction at the van der Waals interface in twisted bilayer graphene," *Nature Materials*, vol. 18, no. 5, pp. 448–453, 2019.

[74] M. R. Rosenberger, H.-J. Chuang, M. Phillips, V. P. Oleshko, K. M. McCreary, S. V. Sivaram, C. S. Hellberg, and B. T. Jonker, "Twist angle-dependent atomic reconstruction and moiré patterns in transition metal dichalcogenide heterostructures," *ACS Nano*, vol. 14, no. 4, pp. 4550–4558, 2020.

[75] A. Weston, Y. Zou, V. Enaldiev, A. Summerfield, N. Clark, V. Zólyomi, A. Graham, C. Yelgel, S. Magorrian, M. Zhou, *et al.*, "Atomic reconstruction in twisted

bilayers of transition metal dichalcogenides," *Nature Nanotechnology*, vol. 15, no. 7, pp. 592–597, 2020.

[76] V. Enaldiev, V. Zolyomi, C. Yelgel, S. Magorrian, and V. Fal'Ko, "Stacking domains and dislocation networks in marginally twisted bilayers of transition metal dichalcogenides," *Physical Review Letters*, vol. 124, no. 20, p. 206101, 2020.

[77] M. H. Naik, E. C. Regan, Z. Zhang, Y.-H. Chan, Z. Li, D. Wang, Y. Yoon, C. S. Ong, W. Zhao, S. Zhao, *et al.*, "Intralayer charge-transfer moiré excitons in van der Waals superlattices," *Nature*, vol. 609, no. 7925, pp. 52–57, 2022.

[78] H. Li, S. Li, M. H. Naik, J. Xie, X. Li, J. Wang, E. Regan, D. Wang, W. Zhao, S. Zhao, *et al.*, "Imaging moiré flat bands in three-dimensional reconstructed WSe_2/WS_2 superlattices," *Nature Materials*, vol. 20, no. 7, pp. 945–950, 2021.

[79] S. Wu, S. Buckley, J. R. Schaibley, L. Feng, J. Yan, D. G. Mandrus, F. Hatami, W. Yao, J. Vučković, A. Majumdar, *et al.*, "Monolayer semiconductor nanocavity lasers with ultralow thresholds," *Nature*, vol. 520, no. 7545, pp. 69–72, 2015.

[80] Y. Ye, Z. J. Wong, X. Lu, X. Ni, H. Zhu, X. Chen, Y. Wang, and X. Zhang, "Monolayer excitonic laser," *Nature Photonics*, vol. 9, no. 11, pp. 733–737, 2015.

[81] O. Salehzadeh, M. Djavid, N. H. Tran, I. Shih, and Z. Mi, "Optically pumped two-dimensional MoS_2 lasers operating at room-temperature," *Nano Letters*, vol. 15, no. 8, pp. 5302–5306, 2015.

[82] J. Shang, C. Cong, Z. Wang, N. Peimyoo, L. Wu, C. Zou, Y. Chen, X. Y. Chin, J. Wang, C. Soci, *et al.*, "Room-temperature 2D semiconductor activated vertical-cavity surface-emitting lasers," *Nature Communications*, vol. 8, no. 543, p. 543, 2017.

[83] D. Edelberg, D. Rhodes, A. Kerelsky, B. Kim, J. Wang, A. Zangiabadi, C. Kim, A. Abhinandan, J. Ardelean, M. Scully, *et al.*, "Approaching the intrinsic limit in transition metal diselenides via point defect control," *Nano Letters*, vol. 19, no. 7, pp. 4371–4379, 2019.

[84] M. A. Meitl, Z.-T. Zhu, V. Kumar, K. J. Lee, X. Feng, Y. Y. Huang, I. Adesida, R. G. Nuzzo, and J. A. Rogers, "Transfer printing by kinetic control of adhesion to an elastomeric stamp," *Nature Materials*, vol. 5, no. 1, pp. 33–38, 2006.

[85] P. Tonndorf, R. Schmidt, P. Böttger, X. Zhang, J. Börner, A. Liebig, M. Albrecht, C. Kloc, O. Gordan, D. R. Zahn, *et al.*, "Photoluminescence emission and raman response of monolayer MoS_2, $MoSe_2$, and WSe_2," *Optics express*, vol. 21, no. 4, pp. 4908–4916, 2013.

[86] R. V. Gorbachev, I. Riaz, R. R. Nair, R. Jalil, L. Britnell, B. D. Belle, E. W. Hill, K. S. Novoselov, K. Watanabe, T. Taniguchi, *et al.*, "Hunting for monolayer boron nitride: optical and raman signatures," *Small*, vol. 7, no. 4, pp. 465–468, 2011.

[87] A. Castellanos-Gomez, M. Buscema, R. Molenaar, V. Singh, L. Janssen, H. S. Van Der Zant, and G. A. Steele, "Deterministic transfer of two-dimensional materials by all-dry viscoelastic stamping," *2D Materials*, vol. 1, no. 1, p. 011002, 2014.

[88] P. Zomer, M. Guimarães, J. Brant, N. Tombros, and B. Van Wees, "Fast pick up technique for high quality heterostructures of bilayer graphene and hexagonal boron nitride," *Applied Physics Letters*, vol. 105, no. 1, p. 013101, 2014.

[89] A. Raja, L. Waldecker, J. Zipfel, Y. Cho, S. Brem, J. D. Ziegler, M. Kulig, T. Taniguchi, K. Watanabe, E. Malic, *et al.*, "Dielectric disorder in two-dimensional materials," *Nature Nanotechnology*, vol. 14, no. 9, pp. 832–837, 2019.

[90] K. Kim, M. Yankowitz, B. Fallahazad, S. Kang, H. C. Movva, S. Huang, S. Larentis, C. M. Corbet, T. Taniguchi, K. Watanabe, *et al.*, "van der Waals heterostructures with high accuracy rotational alignment," *Nano Letters*, vol. 16, no. 3, pp. 1989–1995, 2016.

[91] Andor, "Grating adjustment." `https://andor.oxinst.cn/assets/uploads/andor-support-resources/FAQ035.pdf`.

[92] W. Zhao, Z. Ghorannevis, L. Chu, M. Toh, C. Kloc, P.-H. Tan, and G. Eda, "Evolution of electronic structure in atomically thin sheets of WS_2 and WSe_2," *ACS Nano*, vol. 7, no. 1, pp. 791–797, 2013.

[93] K. P. Dhakal, D. L. Duong, J. Lee, H. Nam, M. Kim, M. Kan, Y. H. Lee, and J. Kim, "Confocal absorption spectral imaging of MoS_2: optical transitions depending on the atomic thickness of intrinsic and chemically doped MoS_2," *Nanoscale*, vol. 6, no. 21, pp. 13028–13035, 2014.

[94] Y. Li, A. Chernikov, X. Zhang, A. Rigosi, H. M. Hill, A. M. Van Der Zande, D. A. Chenet, E.-M. Shih, J. Hone, and T. F. Heinz, "Measurement of the optical dielectric function of monolayer transition-metal dichalcogenides: MoS_2, $MoSe_2$, WS_2, and WSe_2," *Physical Review B*, vol. 90, no. 20, p. 205422, 2014.

[95] J. G. Roch, G. Froehlicher, N. Leisgang, P. Makk, K. Watanabe, T. Taniguchi, and R. J. Warburton, "Spin-polarized electrons in monolayer MoS_2," *Nature Nanotechnology*, vol. 14, no. 5, pp. 432–436, 2019.

[96] X. Li, Y. Shi, S. Li, W. Shi, W. Han, C. Zhou, X. Zhao, and B. Liang, "Layer-number dependent reflection spectra of MoS_2 flakes on SiO_2/Si substrate," *Optical Materials Express*, vol. 8, no. 10, pp. 3082–3091, 2018.

[97] J. S. Ross, S. Wu, H. Yu, N. J. Ghimire, A. M. Jones, G. Aivazian, J. Yan, D. G. Mandrus, D. Xiao, W. Yao, *et al.*, "Electrical control of neutral and charged excitons in a monolayer semiconductor," *Nature Communications*, vol. 4, no. 1, p. 1474, 2013.

[98] C. Ruppert, B. Aslan, and T. F. Heinz, "Optical properties and band gap of single-and few-layer $MoTe_2$ crystals," *Nano Letters*, vol. 14, no. 11, pp. 6231–6236, 2014.

[99] W.-T. Hsu, Z.-A. Zhao, L.-J. Li, C.-H. Chen, M.-H. Chiu, P.-S. Chang, Y.-C. Chou, and W.-H. Chang, "Second harmonic generation from artificially stacked transition metal dichalcogenide twisted bilayers," *ACS Nano*, vol. 8, no. 3, pp. 2951–2958, 2014.

[100] S. Psilodimitrakopoulos, L. Mouchliadis, I. Paradisanos, A. Lemonis, G. Kioseoglou, and E. Stratakis, "Ultrahigh-resolution nonlinear optical imaging of the armchair orientation in 2D transition metal dichalcogenides," *Light: Science & Applications*, vol. 7, no. 5, pp. 18005–18005, 2018.

[101] S. Psilodimitrakopoulos, A. Orekhov, L. Mouchliadis, D. Jannis, G. Maragkakis, G. Kourmoulakis, N. Gauquelin, G. Kioseoglou, J. Verbeeck, and E. Stratakis, "Optical versus electron diffraction imaging of twist-angle in 2D transition metal dichalcogenide bilayers," *npj 2D Materials and Applications*, vol. 5, no. 1, p. 77, 2021.

[102] D. Clark, V. Senthilkumar, C. Le, D. Weerawarne, B. Shim, J. Jang, J. Shim, J. Cho, Y. Sim, M.-J. Seong, *et al.*, "Strong optical nonlinearity of CVD-grown MoS_2 monolayer as probed by wavelength-dependent second-harmonic generation," *Physical Review B*, vol. 90, no. 12, p. 121409, 2014.

[103] N. Kumar, S. Najmaei, Q. Cui, F. Ceballos, P. M. Ajayan, J. Lou, and H. Zhao, "Second harmonic microscopy of monolayer MoS_2," *Physical Review B*, vol. 87, no. 16, p. 161403, 2013.

[104] Z. Wang, *Optical properties of 2D transition metal dichalcogenides enhanced by plasmonic nanostructures*. PhD thesis, National University of Singapore and Imperial College London, 2017.

[105] G. M. Maragkakis, S. Psilodimitrakopoulos, L. Mouchliadis, I. Paradisanos, A. Lemonis, G. Kioseoglou, E. Stratakis, *et al.*, "Imaging the crystal orientation of 2D transition metal dichalcogenides using polarization-resolved second-harmonic generation," *Opto-Electronic Advances*, vol. 2, no. 11, pp. 190026–1, 2019.

[106] J. Wang, J. Ardelean, Y. Bai, A. Steinhoff, M. Florian, F. Jahnke, X. Xu, M. Kira, J. Hone, and X.-Y. Zhu, "Optical generation of high carrier densities in 2D semiconductor heterobilayers," *Science Advances*, vol. 5, no. 9, p. eaax0145, 2019.

[107] A. R. Khan, B. Liu, T. Lü, L. Zhang, A. Sharma, Y. Zhu, W. Ma, and Y. Lu, "Direct measurement of folding angle and strain vector in atomically thin WS_2 using second-harmonic generation," *ACS Nano*, vol. 14, no. 11, pp. 15806–15815, 2020.

[108] J. Liang, J. Zhang, Z. Li, H. Hong, J. Wang, Z. Zhang, X. Zhou, R. Qiao, J. Xu, P. Gao, *et al.*, "Monitoring local strain vector in atomic-layered $MoSe_2$ by second-harmonic generation," *Nano Letters*, vol. 17, no. 12, pp. 7539–7543, 2017.

[109] I. Paradisanos, A. M. S. Raven, T. Amand, C. Robert, P. Renucci, K. Watanabe, T. Taniguchi, I. C. Gerber, X. Marie, and B. Urbaszek, "Second harmonic generation control in twisted bilayers of transition metal dichalcogenides," *Physical Review B*, vol. 105, no. 11, p. 115420, 2022.

[110] Y. Song, R. Tian, J. Yang, R. Yin, J. Zhao, and X. Gan, "Second harmonic generation in atomically thin $MoTe_2$," *Advanced Optical Materials*, vol. 6, no. 17, p. 1701334, 2018.

[111] B. Miller, A. Steinhoff, B. Pano, J. Klein, F. Jahnke, A. Holleitner, and U. Wurstbauer, "Long-lived direct and indirect interlayer excitons in van der Waals heterostructures," *Nano Letters*, vol. 17, no. 9, pp. 5229–5237, 2017.

[112] PicoQuant, "Time-correlated single photon counting." `https://www.picoquant.com/images/uploads/page/files/7253/technote_tcspc.pdf`.

[113] S. instruments, "Timetagger user manual." `https://www.swabianinstruments.com/static/downloads/TimeTagger_User_Manual.pdf`.

[114] D. Huang, J. Choi, C.-K. Shih, and X. Li, "Excitons in semiconductor moiré superlattices," *Nature Nanotechnology*, vol. 17, no. 3, pp. 227–238, 2022.

[115] E. C. Regan, D. Wang, E. Y. Paik, Y. Zeng, L. Zhang, J. Zhu, A. H. MacDonald, H. Deng, and F. Wang, "Emerging exciton physics in transition metal dichalcogenide heterobilayers," *Nature Reviews Materials*, vol. 7, pp. 778–795, 2022.

[116] Q. Lin, H. Fang, Y. Liu, Y. Zhang, M. Fischer, J. Li, J. Hagel, S. Brem, E. Malic, N. Stenger, *et al.*, "A room-temperature moir\'e interlayer exciton laser," *arXiv preprint arXiv:2302.01266*, 2023.

[117] H. Fang, C. Battaglia, C. Carraro, S. Nemsak, B. Ozdol, J. S. Kang, H. A. Bechtel, S. B. Desai, F. Kronast, A. A. Unal, *et al.*, "Strong interlayer coupling in van der waals heterostructures built from single-layer chalcogenides," *Proceedings of the National Academy of Sciences*, vol. 111, no. 17, pp. 6198–6202, 2014.

[118] D. Unuchek, A. Ciarrocchi, A. Avsar, K. Watanabe, T. Taniguchi, and A. Kis, "Room-temperature electrical control of exciton flux in a van der Waals heterostructure," *Nature*, vol. 560, no. 7718, pp. 340–344, 2018.

[119] J. Kunstmann, F. Mooshammer, P. Nagler, A. Chaves, F. Stein, N. Paradiso, G. Plechinger, C. Strunk, C. Schüller, G. Seifert, *et al.*, "Momentum-space indirect interlayer excitons in transition-metal dichalcogenide van der Waals heterostructures," *Nature Physics*, vol. 14, no. 8, pp. 801–805, 2018.

[120] A. Rodriguez, M. Kalbáč, and O. Frank, "Strong localization effects in the photoluminescence of transition metal dichalcogenide heterobilayers," *2D Materials*, vol. 8, no. 2, p. 025028, 2021.

[121] F. Carrascoso, D.-Y. Lin, R. Frisenda, and A. Castellanos-Gomez, "Biaxial strain tuning of interlayer excitons in bilayer MoS_2," *Journal of Physics: Materials*, vol. 3, no. 1, p. 015003, 2019.

[122] Y. Tang, J. Gu, S. Liu, K. Watanabe, T. Taniguchi, J. Hone, K. F. Mak, and J. Shan, "Tuning layer-hybridized moiré excitons by the quantum-confined stark effect," *Nature Nanotechnology*, vol. 16, no. 1, pp. 52–57, 2021.

[123] K. Liu, L. Zhang, T. Cao, C. Jin, D. Qiu, Q. Zhou, A. Zettl, P. Yang, S. G. Louie, and F. Wang, "Evolution of interlayer coupling in twisted molybdenum disulfide bilayers," *Nature Communications*, vol. 5, no. 1, p. 4966, 2014.

[124] Y. Niu, S. Gonzalez-Abad, R. Frisenda, P. Marauhn, M. Drüppel, P. Gant, R. Schmidt, N. S. Taghavi, D. Barcons, A. J. Molina-Mendoza, *et al.*, "Thickness-dependent differential reflectance spectra of monolayer and few-layer MoS_2, $MoSe_2$, WS_2 and WSe_2," *Nanomaterials*, vol. 8, no. 9, p. 725, 2018.

[125] L. Sirigu, D. Oberli, L. Degiorgi, A. Rudra, and E. Kapon, "Excitonic lasing in semiconductor quantum wires," *Physical Review B*, vol. 61, no. 16, p. R10575, 2000.

[126] J. Choi, W.-T. Hsu, L.-S. Lu, L. Sun, H.-Y. Cheng, M.-H. Lee, J. Quan, K. Tran, C.-Y. Wang, M. Staab, *et al.*, "Moiré potential impedes interlayer exciton diffusion in van der Waals heterostructures," *Science Advances*, vol. 6, no. 39, p. eaba8866, 2020.

[127] G. Moody, J. Schaibley, and X. Xu, "Exciton dynamics in monolayer transition metal dichalcogenides," *JOSA B*, vol. 33, no. 7, pp. C39–C49, 2016.

[128] M. Amani, D.-H. Lien, D. Kiriya, J. Xiao, A. Azcatl, J. Noh, S. R. Madhvapathy, R. Addou, S. Kc, M. Dubey, *et al.*, "Near-unity photoluminescence quantum yield in MoS_2," *Science*, vol. 350, no. 6264, pp. 1065–1068, 2015.

[129] Y. Lei, Q. Lin, S. Xiao, J. Li, and H. Fang, "Optically active telecom defects in $MoTe_2$ fewlayers at room temperature," *Nanomaterials*, vol. 13, no. 9, p. 1501, 2023.

[130] Y. Ota, R. Katsumi, K. Watanabe, S. Iwamoto, and Y. Arakawa, "Topological photonic crystal nanocavity laser," *Communications Physics*, vol. 1, no. 86, p. 86, 2018.

[131] V. I. Klimov, S. A. Ivanov, J. Nanda, M. Achermann, I. Bezel, J. A. McGuire, and A. Piryatinski, "Single-exciton optical gain in semiconductor nanocrystals," *Nature*, vol. 447, no. 7143, pp. 441–446, 2007.

[132] W. Li, X. Lu, S. Dubey, L. Devenica, and A. Srivastava, "Dipolar interactions between localized interlayer excitons in van der Waals heterostructures," *Nature Materials*, vol. 19, no. 6, pp. 624–629, 2020.

[133] M. A. Bandres, S. Wittek, G. Harari, M. Parto, J. Ren, M. Segev, D. N. Christodoulides, and M. Khajavikhan, "Topological insulator laser: Experiments," *Science*, vol. 359, no. 6381, p. eaar4005, 2018.

[134] F. Cadiz, E. Courtade, C. Robert, G. Wang, Y. Shen, H. Cai, T. Taniguchi, K. Watanabe, H. Carrere, D. Lagarde, *et al.*, "Excitonic linewidth approaching the homogeneous limit in MoS_2-based van der Waals heterostructures," *Physical Review X*, vol. 7, no. 2, p. 021026, 2017.

[135] H. Deng, G. Weihs, C. Santori, J. Bloch, and Y. Yamamoto, "Condensation of semiconductor microcavity exciton polaritons," *Science*, vol. 298, no. 5591, pp. 199–202, 2002.

[136] J. Sung, D. Shin, H. Cho, S. W. Lee, S. Park, Y. D. Kim, J. S. Moon, J.-H. Kim, and S.-H. Gong, "Room-temperature continuous-wave indirect-bandgap transition lasing in an ultra-thin WS_2 disk," *Nature Photonics*, vol. 16, no. 11, pp. 792–797, 2022.

[137] P. Zhao, Z. Feng, F. Qi, A. Qi, Y. Wang, and W. Zheng, "Blue shift of laser mode in photonic crystal microcavity," in *Semiconductor Lasers and Applications VI*, vol. 9267, pp. 99–104, SPIE, 2014.

[138] Q. Cai, D. Scullion, W. Gan, A. Falin, S. Zhang, K. Watanabe, T. Taniguchi, Y. Chen, E. J. Santos, and L. H. Li, "High thermal conductivity of high-quality monolayer boron nitride and its thermal expansion," *Science Advances*, vol. 5, no. 6, p. eaav0129, 2019.

[139] S. Kreinberg, W. W. Chow, J. Wolters, C. Schneider, C. Gies, F. Jahnke, S. Höfling, M. Kamp, and S. Reitzenstein, "Emission from quantum-dot high-β microcavities: transition from spontaneous emission to lasing and the effects of superradiant emitter coupling," *Light: Science & Applications*, vol. 6, no. e17030, p. e17030, 2017.

[140] W. Wen, L. Wu, and T. Yu, "Excitonic lasers in atomically thin 2D semiconductors," *ACS Materials Letters*, vol. 2, no. 10, pp. 1328–1342, 2020.

[141] H. Gerhardt, H. Welling, and A. Güttner, "Measurements of the laser linewidth due to quantum phase and quantum amplitude noise above and below threshold. I," *Zeitschrift für Physik*, vol. 253, no. 2, pp. 113–126, 1972.

[142] X. Fu, X. Fu, Y. Chen, L. Qin, H. Peng, R. Shi, F. Li, Q. Zhou, Y. Wang, Y. Zhou, *et al.*, "Optically pumped monolayer $MoSe_2$ excitonic lasers from whispering gallery mode microcavities," *The Journal of Physical Chemistry Letters*, vol. 11, no. 2, pp. 541–547, 2019.

[143] S. T. Jagsch, N. V. Triviño, F. Lohof, G. Callsen, S. Kalinowski, I. M. Rousseau, R. Barzel, J.-F. Carlin, F. Jahnke, R. Butté, *et al.*, "A quantum optical study of thresholdless lasing features in high-β nitride nanobeam cavities," *Nature Communications*, vol. 9, no. 1, p. 564, 2018.

[144] J.-X. Yu, S. Xing, G.-Y. Dai, S.-Y. Ling-Hu, and F.-X. Gu, "Direct-bandgap bilayer WSe_2/microsphere monolithic cavity for low-threshold lasing," *Advanced Materials*, vol. 34, no. 3, p. 2106502, 2022.

[145] X. Ge, M. Minkov, S. Fan, X. Li, and W. Zhou, "Laterally confined photonic crystal surface emitting laser incorporating monolayer tungsten disulfide," *npj 2D Materials and Applications*, vol. 3, no. 16, p. 16, 2019.

[146] L. Zhao, Q. Shang, Y. Gao, J. Shi, Z. Liu, J. Chen, Y. Mi, P. Yang, Z. Zhang, W. Du, *et al.*, "High-temperature continuous-wave pumped lasing from large-area monolayer semiconductors grown by chemical vapor deposition," *ACS Nano*, vol. 12, no. 9, pp. 9390–9396, 2018.

[147] H.-T. Lin, C.-Y. Chang, C.-L. Yu, A. B. Lee, S.-Y. Gu, L.-S. Lu, Y.-W. Zhang, S.-Y. Lin, W.-H. Chang, S.-W. Chang, *et al.*, "Boost lasing performances of 2D semiconductor in a hybrid tungsten diselenide monolayer/cadmium selenide quantum dots microcavity laser," *Advanced Optical Materials*, vol. 10, no. 20, p. 2200799, 2022.

[148] A. Chernikov, C. Ruppert, H. M. Hill, A. F. Rigosi, and T. F. Heinz, "Population inversion and giant bandgap renormalization in atomically thin WS_2 layers," *Nature Photonics*, vol. 9, no. 7, pp. 466–470, 2015.

[149] A. Steinhoff, M. Florian, M. Rösner, G. Schönhoff, T. O. Wehling, and F. Jahnke, "Exciton fission in monolayer transition metal dichalcogenide semiconductors," *Nature Communications*, vol. 8, no. 1, p. 1166, 2017.

[150] Z. Wang, H. Sun, Q. Zhang, J. Feng, J. Zhang, Y. Li, and C.-Z. Ning, "Excitonic complexes and optical gain in two-dimensional molybdenum ditelluride well below the Mott transition," *Light: Science & Applications*, vol. 9, no. 1, p. 39, 2020.

[151] L. Reeves, Y. Wang, and T. F. Krauss, "2D material microcavity light emitters: to lase or not to lase?," *Advanced Optical Materials*, vol. 6, no. 19, p. 1800272, 2018.

[152] K. S. Kim, D. Lee, C. S. Chang, S. Seo, Y. Hu, S. Cha, H. Kim, J. Shin, J.-H. Lee, S. Lee, *et al.*, "Non-epitaxial single-crystal 2D material growth by geometric confinement," *Nature*, pp. 1–7, 2023.

{2.7182818284}ϑφερτυθιοπσδφγηξκλ